Mémoire

Auteur : Verkercke, Sébastien
Promoteur(s) : 8567; Wautelet, Gilles
Faculté : Faculté des Sciences
Diplôme : Master en sciences spatiales, à finalité approfondie
Année académique : 2021-2022
URI/URL : http://hdl.handle.net/2268.2/14760

Analysis of the Impact of Solar Energetic Particles Events on the Martian Neutral Upper Atmosphere using Mars Express Radio Occultation Data

by Sébastien Verkercke

Master Thesis Promoter: Ozgur Karatekin

Master Thesis Co-supervisor : Gilles Wautelet

Evaluation committee:
Véronique Dehant
Michaël De Becker

Academic Year 2021/2022
Faculty of Sciences
Master in Space Sciences, Research focus

Master Thesis presented in order to obtain a Master Degree in Space Sciences at the University of Liège

ROYAL OBSERVATORY
OF BELGIUM

Acknowledgements

Even if this master thesis is an individual work, it would not have been possible to make it without the precious help of the following persons that deserve acknowledgements for their support. First and foremost, I would like to thank Ozgur Karatekin for his supervision of this thesis. His valuable advices and the discussions he provided me as well as the time he allocated for this research made this thesis possible. He really showed the true quality of a great supervisor and mentor and I am hoping that we will continue to collaborate on future research projects in a way or another. I also want to thank Grégoire Henry for his precious help with the programming part of this thesis and for his availability for the numerous discussions we had on the whole project, as well as Ananya Krishnan for her explanations on radio occultation measurements and for all her answers to my (too) numerous questions. I also have to thank Cem Berk Senel for his support with the numerical climate models of Mars, as well as Véronique Dehant for her help in the finding of the subject of this thesis and the discussions we had throughout the year. Finally, I want to thank my parents and my fiancée for their full support during this master at the Université de Liège.

Contents

Introduction **1**

1 Generalities of Mars **4**
1.1 The Planet Mars . . . 4
1.1.1 Mars Orbital Parameters . . . 4
1.1.2 Mars Interior and Surface . . . 5
1.2 The Martian Atmosphere . . . 6
1.3 The Martian Ionosphere . . . 8
1.3.1 The Ionospheric Structure Formation . . . 8
1.3.2 The Dayside of the Martian Ionosphere . . . 10
1.3.3 The Nightside of the Martian Ionosphere . . . 10
1.3.4 The Martian Ionospheric Composition . . . 10
1.3.5 Sporadic Ionospheric Structure Induced by SEP Electron . . . 11

2 Radar Sounding and Radio Occultations **12**
2.1 Radar Sounding . . . 12
2.1.1 Data Acquisition . . . 12
2.1.2 Ionospheric Effects on Radio Wave Propagation . . . 13
2.2 Radio Occultation . . . 14
2.2.1 Measurement Method and Signals Characteristics . . . 15
2.2.2 Observed Quantities and Frequency Residuals . . . 16
2.2.3 Principles: From Frequency Residuals to Ionospheric/Atmospheric Refractivity 20
2.2.4 Deriving Density, Pressure and Temperature Profiles . . . 29
2.2.5 Uncertainties on the Ionospheric and Atmospheric Profiles . . . 33
2.3 Numerical Method and Stability . . . 35
2.3.1 Numerical Integration of the Abel Transform . . . 36
2.3.2 Baseline Fits and Manual-fits . . . 37
2.3.3 Stability of the Baseline Parameters . . . 40
2.3.4 Comparison of Vertical Profiles with an External Study . . . 43

3 Data Selections and Results **48**
3.1 Data Selection Using Radar Blackouts of MARSIS and SHARAD . . . 48
3.2 Case Study 1 - CME Impact on Mars during June 2011 . . . 50
3.2.1 Chronology and Properties of the Event through Various Measurements . . . 50
3.2.2 Radio Occultation Ionospheric Profiles during June 2011 CME Impact . . . 54
3.2.3 Radio Occultation Atmospheric Profiles during June 2011 CME Impact . . . 56
3.3 Case Study 2 - CME Impact on Mars during February/March 2015 . . . 62
3.3.1 Chronology and Properties of the Event through Various Measurements . . . 62
3.3.2 Radio Occultation Ionospheric Profiles during 2015 CME Impact . . . 63
3.3.3 Radio Occultation Atmospheric Profiles during 2015 CME Impact . . . 65

4 Conclusion and Perspectives **69**

References **72**

List of Figures

1 Vertical Temperature Profiles . . . 7
2 Martian Ionosphere Formation . . . 9
3 MARSIS Blackout . . . 14
4 Mars Radio Occultation Sequence . . . 15
5 Frequency residuals at X-band from an occultation . . . 20
6 Occultation Geometry . . . 22
7 Bending of the ray due to refraction . . . 24
8 Ray path geometry in polar coordinates . . . 26
9 Refractivity vertical profile . . . 28
10 Typical Martian ionospheric and atmospheric density profiles . . . 30
11 Typical Martian atmospheric pressure and temperature profiles . . . 32
12 Fitted baseline corrected electron density profile . . . 37
13 Manually fitted baseline corrected electron density profile . . . 39
14 Comparison of baseline corrected vertical profiles regarding a_0 . . . 41
15 Comparison of baseline corrected vertical profiles regarding a_1 . . . 42
16 Differences of vertical profiles using different baseline correction regarding a_0 . . . 42
17 Differences of vertical profiles using different baseline correction regarding a_1 . . . 43
18 Comparison of refractivity vertical profiles from different studies . . . 44
19 Comparison of neutral number density vertical profiles form different studies . . . 45
20 Comparison of vertical temperature profiles form different studies . . . 47
21 Lists of orbits with blackouts occurrence for MARSIS and SHARAD . . . 49
22 Helioweather results on June 2011 CME . . . 50
23 Radargrams obtained by MARSIS during the 2011 CME impact . . . 51
24 ASPERA-3/MEX measurements during the CME impact . . . 53
25 Vertical electron density profiles compared with ASPERA-3/MEX measurements . . . 55
26 Vertical atmospheric refractivity profiles of 2011 . . . 56
27 Vertical atmospheric scale height profiles of 2011 . . . 57
28 Vertical temperature profiles compared to GCMs outputs . . . 60
29 Vertical temperature profiles retrieved from Table 3 data . . . 61
30 MAVEN measurements during the CME impact of February/March 2015 . . . 63
31 Vertical electron density profiles compared with MAVEN measurements . . . 64
32 Vertical atmospheric refractivity profiles of 2015 . . . 65
33 Vertical atmospheric scale height profiles of 2015 . . . 66
34 Vertical temperature profiles retrieved from Table 4 data . . . 67

List of Tables

1 Mars and Earth Orbital Parameters . . . 5
2 Data Files used in Manual Baseline Fit Stability Analysis . . . 40
3 Data Files used in June 2011 CME impact analysis . . . 54
4 Data Files used in February/March 2015 CME impact analysis . . . 64

Abstract

It is only recently that the periods during which the radars MARSIS and SHARAD are incapacitated, have been correlated to coronal mass ejections (CME) and solar energetic particles (SEP) events. MAVEN measurements of enhancements of the SEP electrons flux happen to be consistent with these radar blackouts. This phenomenon was attributed to an extra-ionization of the neutral atmosphere of Mars by the increased flux of SEP electrons, inducing an increase of the electron density which attenuates the radar signal. However, the effect of this phenomenon on the physical properties of the atmosphere was never observed as the instruments generally used, experienced blackouts. This study proposes the use of radio occultations to monitor the physical properties of the neutral Martian atmosphere during CME and SEP events as the radio signals used in this technique are not attenuated by the extra-ionization. The two case studies of this work suggest that CME/SEP events are correlated to a decrease of the upper atmosphere refractivity due to an increase of the electron density induced by an extra-ionization caused by the SEP electrons. An atmospheric disturbance is also observed during CME/SEP events further suggesting an extra-ionization of this same region. Our results are coherent with the MAVEN and MEX measurements of the SEP electrons as well as with MARSIS and SHARAD blackouts. This study presents the first global analysis of such modifications of the physical properties of the neutral atmosphere of Mars.

Key words: Mars, Radio occultation, Mars Express, Atmosphere, Ionosphere, Remote sensing

Résumé

Ce n'est que récemment que les périodes durant lesquelles les incapacités des radars MARSIS et SHARAD ont été corrélées avec les événements d'éjections de masses coronales (EMC) et de particules énergiques solaires (PES). Les mesures de MAVEN des augmentations du flux d'électrons de PES sont consitantes avec les "blackouts" des radars. Ce phénomène a été attribué à une ionisation supplémentaire de l'atmosphère neutre de Mars par les flux accrus d'électrons de PES, causant une augmentation de la densité d'électrons, ce qui attenue le signal radar. Cependant, l'effet de ce phénomène sur les propriétes physiques de l'atmosphère n'a jamais été observé car les instruments utilisés habituellement expérimentaient des "blackouts". Cette étude propose l'utilisation d'occultations radio afin de mesurer les propriétés physiques de l'atmosphère neutre martienne lors des événements EMC et PES car les signaux radio utilisés par cette méthode ne sont pas atténués par l'ionisation supplémentaire. Les deux études de cas de cette recherche suggèrent que les événements ECM/PES sont corrélés avec une diminution de la réfractivité dans la haute atmosphère de Mars causée par une augmentation de la densité d'électrons, elle-même induite par une ionisation supplémentaire due aux électrons PES. Une perturbation atmosphérique est aussi observée durant les événements EMC/PES suggérant d'autant plus une ionisation supplémentaire de cette région. Nos résultats sont cohérents avec les mesures des électrons PES de MAVEN et MEX ainsi qu'avec les "blackouts" de MARSIS et SHARAD. Ceci présente la première analyse globale de tels effets sur les propriétés physiques de l'atmosphère neutre de Mars.

Mots clefs: Mars, Occultation radio, Mars Express, Atmosphère, Ionosphère, Télédétection

Introduction

Mars has always intrigued humanity, from the ancient Greeks describing it as a "wandering" star in the night sky until today's extensive explorations and observations of the red planet [1][2][3]. However, even while being a neighbouring planet of the Earth and under continuous studies, Mars has still not revealed all its secrets. In fact, the planet started to gain intensive interest as from 1960, with the first missions launched to explore Mars and its first successful flyby in 1965 by Mariner IV [3]. The presence of ice water and the evidences that the planet was once rich in liquid water, combined with volcanic activity rose the question of the possible presence of life once up on a time on the surface of Mars. Mars' atmosphere also falls into the same category of planetary atmospheres than the Earth's one, which are fast rotating and mainly dominated by radiative and convective processes [3][4]. Although it is not necessary to study other planetary atmospheres to understand the atmosphere of the Earth, it is mainly accepted that they represent an opportunity to test theories and our general understanding of these processes and their interactions. The physic is the same but observed in different environments with diverse forcing functions and boundary conditions. Since Mariner IV mission, more than a dozen spacecrafts have been launched to explore and study the different aspects of Mars expecting to get answers to the numerous questions that surround it. In particular, Mars' atmosphere, its current structure and its past evolution are still hot topics which could explain some phenomena like the water dissipation from its liquid form through escape process or the difference between its ionospheric structure and the Earth's one and the impacts it has on communications' signals.

In order to study Mars' atmosphere and to measure relevant parameters describing it, a number of remote sensing techniques were created, each with different interests and specificities. In particular, for Mariner IV, even if it was not its main objective, the use of radio occultations to derive atmospheric and ionospheric profiles of Mars was first investigated by Kliore & al. 1965 [5][6]. The changes in the phase, frequency and amplitude of the radio signal of Mariner IV caused by the passage of the signal through the Martian atmosphere could be directly connected to the parameters describing it. Indeed, changes observed directly before and after the planetary occultation of the spacecraft are still used to derive the refractivity and density of the atmosphere, its scale height, and the electron density profile of the Martian ionosphere [5][6][7]. This technique allows a total probing of the atmosphere and ionosphere from the top to the surface as the radio signal is not blocked neither by the plasma of the ionosphere nor by the dust and gases density of the neutral atmosphere close to the surface [6]. It is now widely used by the recent spacecrafts such as Mars Express (MEX) with the Mars Express Orbiter Radio Science (MaRS) or Mars Atmosphere and Volatile Evolution (MAVEN) with the MAVEN Radio Occultation Science Experiment (ROSE), respectively launched in 2003 and 2013.

As from the second wave of Mars exploration that started with the Vikings space missions, it has been clear that one of the major needs to progress in the study of Mars is the acquisition of extended and more detailed observations of the atmosphere [2][3]. This includes the extensive observations of present atmospheric temperature, column dust, water contents and their vertical profiles. This stresses the need for a continuous development of efficient ways of treating the data retrieved from the radio occultations as it is crucial to link the changes observed in the signal to the physical characteristics of the Martian atmosphere and ionosphere. These techniques are necessary

to understand precisely the structure of the atmosphere and of the ionosphere of Mars as these can influence the telecommunications between rovers on Mars' surface and the spacecrafts. Radio occultation can also be used for the probing of the Earth's atmosphere.

In September 2017, the Mars Advanced Radar for Subsurface and Ionosphere Sounding (MARSIS) on-board MEX, suffered from a complete blackout during 10 days while observing Mars' nightside. Similar blackouts were experienced by the Shallow Radar (SHARAD) instrument on board the Mars Reconnaissance Orbiter (MRO) spacecraft[7][8]. It appears that these blackout events were caused by the formation of a global absorption layer, including the deep nightside region [7]. It is known that solar energetic particles (SEPs) or the interplanetary coronal mass ejections (CMEs) can lead to some radar disruptions [7][8]. These are supposed to enhance the electron density of the lower ionosphere below 90 km (or the top of the neutral atmosphere; cf. Section I), where even a small amount of extra-ionization significantly increases the signal attenuation [7]. Since then, studies of the blackout events of both MARSIS and SHARAD were conducted during a full solar cycle [8] and the analysis suggest that solar electrons with energies of tens of keV could be the cause for these absorption layers [7][8]. Even if evidences from the MAVEN observations show that these SEPs and CMEs are correlated to these radar blackouts, no sounding of the ionospheric and atmospheric properties were made during these events.

The aim of this master thesis is to evaluate the impact of the CME and SEP events on the neutral atmosphere of Mars, especially on its density, pressure and temperature anomalies during these radar blackout periods. These effects were never analysed, as previous studies only focused on the ionosphere of Mars and only theorized a plausible effect on the neutral atmosphere. In this optic, the Royal Observatory of Belgium (ROB) elaborated a program able to treat the raw data acquired by MEX and MAVEN through radio occultations and to derive simultaneously atmospheric and ionospheric profiles from these data. This allows a global analysis of the structure which represents a novelty in this research as this method was never used during such events. Radio occultations are not affected by any kind of cut-off due to the local plasma, allowing to probe the atmosphere from the top to the bottom during the period of high solar activity[5][6]. This will further help to understand Mars' atmospheric and ionospheric structures as well as their physical properties. The turbopause, the boundary between Mars' atmosphere and ionosphere, below which turbulent motions and molecular diffusion are dominant, is also affected by the coronal mass ejection and is still not well understood even if many observations are available [6][7][8]. This is due to the numerous influences that directly modify the properties of this region, such as dust storms, solar activity or seasonal variability [4]. Using the radio occultation data available during and around CME and SEP events and the program developed by the ROB, the effects of increased solar activity on Mars' neutral atmosphere and on the turbopause are investigated in this work.

In this optic, this work is organized as followed; the Section I is summarizing the current knowledge of Mars, its atmosphere and its ionosphere acquired through diverse missions and techniques without getting into the details of the latter. The Section II is briefly introducing the technical description of the spacecrafts involved and the properties of their radio signal emissions and receptions. This is followed by a presentation of the radio occultation technique used to acquire data on the ionosphere and the atmosphere. This remote sensing technique and the relations between the signal and the physical properties are detailed in this part. The uncertainties on these quantities

are also derived. In this same section, the numerical method used for the treatment of the data acquired by radio occultation is explained. This is followed by an analysis of the stability of the results produced by this method as parameters are introduced for the baseline fitting of the derived profiles. Comparisons with already published results are also performed to ensure the validity of our data treatment. The Section III is dedicated to the data selections used in this study. The main results of this thesis are then presented, followed by the analysis of the different atmospheric profiles and their identified characteristics. A few case-studies of radio occultations measurements performed during or around SEP events are presented, along the chronology of the SEP events and the physical properties of the atmosphere that were derived. Correlations are made between the observed characteristics of the outputs of the radio occultations measurements and the observations made simultaneously by other instruments linking SEP events to changes in the physical properties of the upper Martian atmosphere. Section IV presents the conclusions of this thesis with an analysis of the results. Some perspectives and improvements for further studies on this subject are also proposed.

1 Generalities of Mars

This section summarizes the current understanding of Mars, its atmosphere and its ionosphere. A brief description of Mars and the aspects of interest for this study are presented here. This first section is setting the context of the environment of this study by describing the basic notions and definitions as well as the different Martian structures that are analysed through out this work. It is also introducing some of the phenomena that are further investigated. This section firstly presents Mars' orbital parameters and the Martian interior and surface with some explanations of the physical properties that contribute to this study. The structure and composition of the atmosphere of Mars are then described, followed by a reflection on its evolution. Thereafter, a similar description is made for the ionosphere with a presentation of the influence of the solar activity on the ionospheric structure. That introduces the different environments that will be analysed through this work and defines the structures and elements that are influencing the atmosphere and the ionosphere which are studied here.

1.1 The Planet Mars

Mars is the fourth terrestrial planet of our Solar system and the second smallest one in this same system. With an average radius 3389.5 km, Mars is only about half the size of the Earth [2]. This planet was formed some 4.5 Gyr ago but its actual appearance is not the one Mars always had [2]. During its evolution, Mars' interior, surface and atmosphere have suffered from tremendous changes that altered the planet aspect and its physical properties on a global scale, notably through the loss of its intrinsic magnetic field and the escape of a large part of its atmosphere and water content [3][4]. The Earthlike orbital parameters of Mars, such as its spin rate and its axial tilt make the planet somehow comparable to the Earth, notably regarding the radiative and convective processes of its atmosphere. However, as explained hereafter, some huge differences exist between the Earth and Mars, setting a whole new different environment to study.

1.1.1 Mars Orbital Parameters

Some of Mars' orbital parameters are similar to the Earth's ones. Both planets have a similar rotation frequency of 7.088 x 10^{-5} s^{-1} and 7.292 x 10^{-5} s^{-1} respectively for Mars and the Earth, making a sidereal day of each planet fairly similar in terms of hours. The obliquity of Mars is also very close to the one of the Earth, with a tilt of 25.19° compared to 23.44° for the Earth[2][4][6]. These are two important features for the comparison of the atmospheres of Mars and the Earth since they dictate respectively the repartition of the heat and the seasonal variability in the atmospheres, as explained later. The orbital semi-major axis, the aphelion and perihelion of Mars are of course greater than the ones of the Earth since it is further from the Sun. Finally, since Mars is approximately only half the size of the Earth with a mass that is close to 0.1 the Earth's mass, the Martian gravity is smaller than on the Earth with a value that approximates the third of the Earth's gravity[4]. This lower value of gravity influences directly the laws governing the atmospheric circulation and structure as it influences the hydrostatic equilibrium.

Solely based on these parameters, one can already tell that models describing the Earth's atmosphere could also be used to describe Mars' atmosphere on a global scale. However, it is necessary to remain very careful with the boundary conditions as they can vary a lot between the two planets.

Metric	Mars	Earth	Ratio
Radius (equatorial) (km)	3396	6378	0.53
Area (10^6 km^2)	144.8	510.1	0.28[a]
Solar day (Mars sol, Earth day, h)	24.66	24.00	1.027
Sidereal day (h)	24.62	23.93	1.029
Rotation frequency, Ω (sidereal, 10^{-5} s^{-1})	7.088	7.292	0.972
Year[c] (Mars sols)	668.6,	355.6,	1.88
Year[c] (Earth days)	687.0	365.25	
Orbital semi-major axis[b] (AU)	1.524	1.000	1.52
Orbit eccentricity[b]	0.0935	0.0167	5.60
Perihelion[b] (AU)	1.38	0.98	1.41
Aphelion[b] (AU)	1.67	1.02	1.64
Obliquity (tilt of rotation axis)[b] (deg)	25.19	23.44	1.075
Gravity (surface, m s^{-2})	3.71	9.80	0.38

Table 1: Table giving the main orbital parameters of Mars and of the Earth as well as their ratios [4].

The Table 1 regroups the major orbital parameters of Mars and of the Earth as well as their ratios. This gives a clearer idea of which parameters are Earthlike and which are not.

1.1.2 Mars Interior and Surface

Mars interior has been probed with the use of a lander sensing the propagation of the shear (S) and pressure (P) waves through its interior using seismometers. Since their propagations depend on the density and on the physical properties of the medium, one can infer the internal structure of the planet from these measurements [8][9]. The only mission to study exclusively the Martian interior was the Interior Exploration using Seismic Investigations, Geodesy and Heat Transport (InSight) mission, which was launched in 2016[10]. The propagation of the S and P waves measured by these different missions revealed that Mars' interior is composed of a large, and certainly liquid, iron core (between 1500 and 2100 km) surrounded by a 1240 to 1850 km thick mantle, itself topped by a 10 to 50 km deep crust[11]. The composition of the core is supposedly iron, nickel, and sulphur whereas the crust is made of iron, magnesium, aluminium, calcium and potassium. Even if not directly studied in this work, Mars' surface and subsurface play the role of a gaseous reservoir in the carbon dioxide cycle of the planet's atmosphere. As mentioned later, CO_2 is the main component of this atmosphere meaning that the surface is closely interacting with the Martian atmosphere

and cannot be neglected [2][3].

Nowadays, Mars does not exhibit any intrinsic magnetic field, meaning that its liquid core does not act as a dynamo anymore. However, Mars is known to have what seems to be a single tectonic plate implying that the renewed crust would only formed along the only spreading center of this plate, which is nearly parallel to the equator. Mars' crust is thus composed by "bands" of crust of similar geological age that extend on approximately the same latitude [3][9][12]. Each band of crust is globally imprinted with the same magnetic properties meaning that a global intrinsic magnetic field must have existed at some point on Mars. The magnetic properties of each band are approximately the same as the one of the magnetic field of Mars at the time of the formation of the band of crust. The magnetic properties vary from band to band, allowing to retrace partly the history of Mars' magnetic field [12]. This remaining crustal magnetic field influences the local structure of the ionosphere.

Mars' surface also exhibits a rich topography with extreme characteristics such as Olympus Mons, the highest peak in the solar system, or Valles Marineris, a canyon as large as the United States. It was intensively studied by the Mars Orbital Laser Altimeter (MOLA) instrument onboard of the Mars Global Surveyor spacecraft, since its launch in 1996 [13].'A precise understanding of Mars' topography is important as it also plays a role on the vertical atmospheric and ionospheric profiles which are measured through different techniques, notably through radio occultation.

1.2 The Martian Atmosphere

Mars atmosphere is much tenuous than on the Earth as its density is only about 1% of the Earth's one, meaning that its pressure and temperature are also much lower[4]. Its composition is also very different from the Earth's atmosphere as it is mainly composed of CO_2 (95.32%) and a small amount of N_2 and Ar. This could be acquired through remote sensors, in-situ laboratories and rovers measurements[2][4]. This shows that even if Mars' spin rate and axial tilt are Earthlike and thus that the Martian atmosphere falls into the same category as the Earth's one, some huge differences exist between the two. For example, the temperature range of the Martian atmosphere near surface is broader than on the Earth as no ocean is regulating it (from 140K to 310K with an average temperature of 215K compared with an average surface temperature of 288K on the Earth)[14].

Even with such large differences, Mars still exhibits similarities with the Earth. At its poles, Mars has icy polar caps composed mostly of carbon dioxide and some water ice. These polar caps change size according to the seasons, influencing the global circulation of its atmosphere. Indeed, the change in insulation created by the tilt of Mars influences directly the content of CO_2 in its atmosphere. In the wintertime, low insulation results in lower temperature which favours the formation of dry carbon dioxide and thus an expansion of the polar cap. However, simultaneously on the other hemisphere, the higher insulation results in the decrease of the dry ice content leading to an increase of the CO_2 content in the atmosphere[2]. This insulation difference generates the global circulation of Mars atmosphere forming Hadley-like cells over the hemispheres [4]. The vertical temperature profile of the Martian atmosphere is also somewhat comparable to the one derived on the Earth. Indeed, the profiles retrieved during the Viking Landers entry are now used as "standards" for the vertical temperature profiles and they exhibit similarities with the temperature profile on the Earth[2][4] (cf. Figure 1). Mars lower atmosphere extends from Mars' surface to $\sim$ 40 km of

altitude and is comparable to the troposphere of the Earth. It is mainly driven by radiative and convective processes and varies with a diurnal cycle. Over this layer and until 100 km altitude, there exists a middle atmosphere which is more or less isothermal [4][15][16]. The lower and middle atmospheres will be further referred as the neutral atmosphere of Mars. Similarly to the Earth, the Martian mesopause is located at approximately 100 km altitude, even if the atmospheres are really physically different. Over the Martian mesopause, the temperature rises due to the absorption of ultraviolet radiations by neutral atoms ionizing the region and forming the ionosphere [2][4].

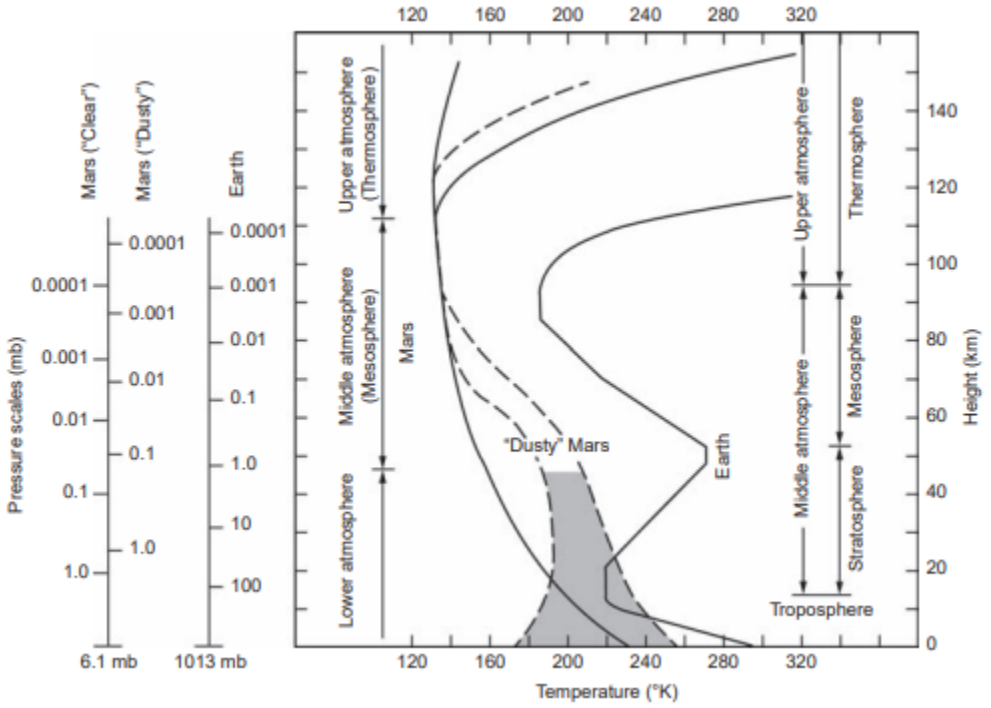

Figure 1: The vertical temperature profile measured when the Viking Landers entered the Martian atmosphere is shown (solid curve on the left) with the standard nomenclature for terrestrial meteorology. This has to be compared with the Earth's vertical temperature profile on the right. Temperatures derived from the Viking Lander 1 entry serve here as a "standard reference atmosphere" for Mars, with similar nomenclature. Dashed curves with shading reflect the effects on temperature of aerosols during major dust events [4].

However, Mars has not always been this dry and cold environment as its surface and atmosphere were once containing higher content of water respectively in liquid and vapour forms. On the surface, the alteration of the volcanic rocks by the liquid water is a piece of evidence that once, water was flowing on Mars and shaped its surface and its composition [3][4]. The composition of the Martian atmosphere and its physical properties were thus very different. The remaining components are representative of the outgassing induced by Mars volcanism. If Mars once had a thicker CO_2 atmosphere able to sustain a hydrologic cycle maintaining liquid water at its surface in the same way as the Earth's atmosphere, it is supposed that this water has now either escape to space or that it is

trapped in subsurface reservoirs [4][14]. The escape processes of the volatiles from Mars atmosphere are not yet well defined but are usually attributed to both the loss of its intrinsic magnetic field and to the global dust storm on the Martian surface [3][4]. In both cases, the ionosphere of Mars seems to have played a role through different escape processes such as sputtering or ion pick-up [2][4].

Mars' surface is often subject to large dust storms as strong circulations exist in its atmosphere. Global dust storm is a truly global event that extends from pole to pole. However, this kind of events are only observed only rarely and not in systematic ways [3]. The dust activity increases at certain moments, especially in Southern Spring and Summer, the so-called "dust storm season" [4]. The local and global dust storms are supposed to be partially responsible of the escape of the volatiles from the Martian atmosphere[14]. Additionally, this dust directly influences the physical properties of the atmosphere such as its optical thickness or even its temperature, as the dust suspended in the Martian atmosphere strongly affects the radiative transfer by the absorption of radiations (cf. Figure 1)[4][14][15][16].

Like on the Earth, the Martian atmosphere is also influenced by the solar activity[2][3][4][14]. Even if the most obvious influence happens in the ionospheric structure of the planet, higher solar activity is supposed to influence the neutral atmosphere as well. The study of this influence on the physical parameters of the neutral atmosphere constitutes the main topic of this work and is further detailed in Section 3.

1.3 The Martian Ionosphere

As it will be explained, the ionosphere plays a special role in radio waves propagation. However, the Martian ionosphere differs from the Earth's one in numerous ways [17][18][19]. Due to the greater distance from the Sun to Mars than to the Earth, the weaker solar radiation flux generates a lower plasma density in the Martian ionosphere. The fact that Mars does not have an intrinsic magnetic field also greatly influences its ionospheric structure. Additionally, the crustal magnetic anomalies also influence this structure locally. This stresses the need for extensive studies of Mars' atmosphere and ionosphere as they impact directly the safety of on-going and future missions on Mars.

1.3.1 The Ionospheric Structure Formation

The Martian ionosphere is an ionized medium that is formed by the photo-ionization of the upper atmosphere by the extreme ultraviolet (EUV) radiation of the Sun. It is thus a thermal weakly ionized plasma of planetary origin [20]. Since this formation process is due to the Sun's radiation, the ionospheric structure is different on the dayside than on the nightside. As there is only a weak crustal magnetic field or no intrinsic magnetic field on Mars, the solar wind can directly interact with its ionosphere on the dayside[2][17]. This interaction creates an ionospheric current which forms an extensive draped induced magnetosphere and generally stands off the solar wind. The solar wind is shocked and diverted around the ionopause. In this region, there is a balance between the incident pressure of the solar wind and the thermal pressure of the planetary plasma [2]. On the dayside, the interplanetary magnetic field "piles up" in front of the ionopause, forming a layer called the magnetic barrier. The region between the bowshock and the magnetic barrier is called the magnetosheath and is composed of turbulent solar plasma decelerated by its magnetic interactions with the obstacle. On the nightside, the magnetic field lines extend in a draped way

forming the ionotail which extends on thousands of kilometers[2][17]. The dayside/nightside ionospheric structure is maintained by the short lifetime of the ions compared to the duration of a sideral day on Mars[2]. The ionospheric structure described here above and the steps leading to its formation are illustrated in the Figure 2.

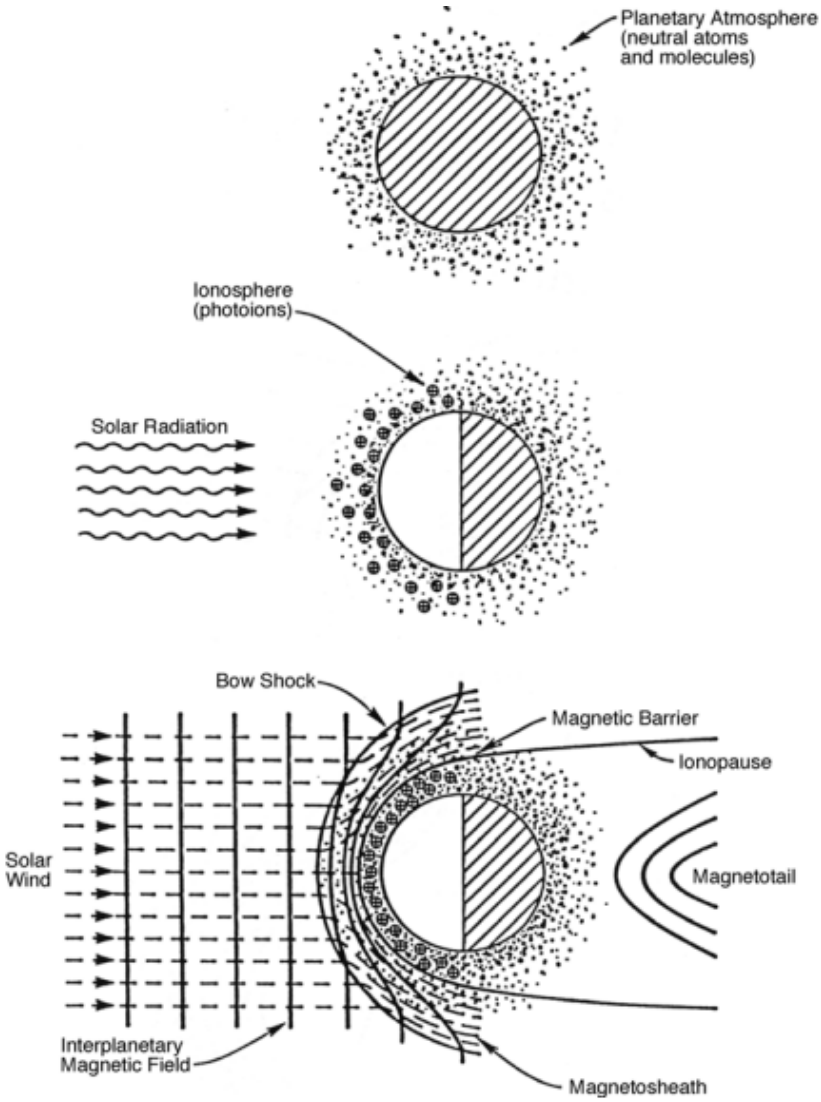

Figure 2: Illustration of the Steps that Lead to the Formation of the Mars Ionosphere in the Solar Wind and Interplanetary Magnetic Field [2]

The ionosphere of Mars is topping the neutral atmosphere and is ranging from approximately 100 km to about 500 km where the ionopause is located. This range is approximative as the base of the ionosphere is influenced by the dust storms, the solar activity, the solar zenith angle (SZA) and the local crustal magnetic field. Moreover, the ionopause is also changing of altitude,

notably due to the solar activity or the SZA [6][18][19]. These variations combined with the difficulty of analysing remotely this layer are directly reflected by the lack of scientific consensus on the boundaries of this layer [18][19]. The actual altitude of the lower boundary is ranging between 80 and 130 km, whereas the ionopause is supposed to be between 350km and 700km [4][6][17][18][19][20].

1.3.2 The Dayside of the Martian Ionosphere

The dayside of the Martian ionosphere is composed of two main layers of planetary plasma: the M2 layer that corresponds to the maximum ionization area of the ionosphere which is produced by the solar EUV photons, and the M1 layer that corresponds to the layer below the maximum of ionization and is mainly produced by the soft X-ray photons[21]. The M2 layer represents the plasma density peak and is located at about 130 km altitude but this altitude, as well as the density peak value, are dependant of the SZA since they result from photochemical processes[20][21]. The M1 layer is a region of lower electron density than the M2 layer but still represents a local maximum of ionization. It is located at approximately an altitude of 105 km, under the M2 layer since soft X-ray photons have a smaller wavelength and therefore penetrate deeper in the atmosphere. Its density is generally half of the M2 layer. As for the M2 layer, its location also depends on the SZA but its is more variable as the solar soft X-ray emissions are also variable and depend strongly on the solar activity[2][20]. As observed by the spacecraft Mariner 9 in 1971, dust storms can also greatly affect the positions of these layers[2].

1.3.3 The Nightside of the Martian Ionosphere

With more restrictive conditions for its observations, the nightside of Mars is less extensively studied than the dayside. Indeed, the maximum data coverage is from 90° to 125° SZA[2]. Additionally, since there is no radiation from the Sun ionizing the atmosphere, the electron density on the nightside has an average of 5.0 x 10^9 m^{-3} which is two orders of magnitude lower than the average value on the dayside. These particularly low values are difficult to be detected through remote sensing techniques[2][20]. However, from what is known, the nightside ionosphere is highly structured and dynamic, and low levels of plasma density may extend out a long distance in a comet-like structure[20].

The origin of the nightside ionospheric plasma is not quite clear but two different sources are possible. One of them is the flow of plasma from the dayside to the nightside of the ionosphere. This transport is thus highly dependent of the solar wind pressure. The other source is the local ion production by impact of energetic electrons[2]. It is indeed observed that on the nightside, the largest peak densities are found in the surrounding of the vertical crustal magnetic fields, which form cusps that allow superthermal electrons to precipitate into the atmosphere. In the contrary, smaller peak densities are found near horizontal crustal magnetic fields, which prevent superthermal electrons from precipitating into the atmosphere[20]. However, due to the lack of observations of the ionospheric nightside of Mars, it is not clear which source is dominant.

1.3.4 The Martian Ionospheric Composition

The upper Martian atmosphere composition differs with altitude. Below a threshold located at approximately 250-300 km, the CO_2 is the dominant component whereas above this threshold, O_2

becomes the most abundant gas. Since the ions are produced by photoionization of the atmosphere components, the ions populating the ionosphere are the singly-ionized versions of the dominant atmospheric neutrals at the particular altitude[20]. This means that CO_2^+ is the most produced ion at lower altitudes whereas O_2^+ is the most produced ion at higher altitudes[2][20][22]. However, the CO_2^+ is shortlived and undergoes a rapid charge transfer reaction with neutral atomic oxygen to form O^+ and O_2^+, making the latter ion the most abundant below 300 km altitude. Above this altitude, O^+ and O_2^+ have similar abundance. O_2^+ is lost by dissociative recombination with an electron whereas O^+ is lost by charge exchanges with neutral molecules which are also further lost through dissociative recombination with an electron[2][20].

1.3.5 Sporadic Ionospheric Structure Induced by SEP Electron

As proven by multiple studies, the SEPs and the CMEs have a clear influence on the structure of the Martian ionosphere[7][8]. Indeed, observations over a complete solar cycle show that high-energy electrons from the Sun can enter the Martian atmosphere, causing enhanced ionization at altitudes between 60 and 90 km[8]. However, the effects of this extra-ionization on the neutral atmosphere parameters, such as the temperature, the density and the pressure have not yet been studied. One would expect an increase of the electron density at these altitudes as the ionization is enhanced. Another expected effect is a higher temperature measured due to the deposition of energy by the SEPs in this layer which would be linked to this increased ionization.

2 Radar Sounding and Radio Occultations

Remote sensing techniques are necessary to study the ionosphere and the atmosphere of Mars. Actually, no continuous in-situ measurement method exists to analyse the upper atmosphere nor for the lower ionosphere[8]. Radar sounding and radio occultation are two different remote sensing methods that are currently used by the spacecrafts orbiting Mars to observe nearly continuously the properties of the Martian ionospheric and atmospheric structures. This section describes both of these techniques, notably how Mars' environment influences the signals used by these remote sensing methods and how the changes in these signals can be linked to physical properties of the media. However, the radio occultation method is detailed here, whereas the radar sounding is only introduced. The reason is that the former represents our main tool for this study while the latter is only used for the selection of the studied periods. The instruments used for the data acquisition are also briefly described.

2.1 Radar Sounding

Radar sounders, such as MARSIS on board of MEX or SHARAD on board of MRO, are instruments that are using low-frequency radar waves (few MHz) that are designed to sound the subsurface and the ionosphere of Mars[21]. The layer that is probed by the radar depends on the frequency of the signal used by the instruments. These different frequencies characterize the different experiments conducted by the instruments.

2.1.1 Data Acquisition

The ionospheric plasma is characterized by a frequency due to the oscillation of the free electrons around the ions. Indeed, as electrons are lighter than ions, they can be considered as particles moving around "static" ions. The Coulomb force acts as a restoring force each time the electrons tend to get away from the ions, creating an oscillation with a particular frequency that depends on the electron density[23].

When the radar sounder is set to probe the ionosphere, it sends a vertical radio wave of the frequency f_w through the topside of the ionospheric plasma. As the wave propagates deeper through the ionosphere, the electron density increases. The wave continues to propagate as long as its frequency is greater than the plasma frequency of the surrounding plasma. When it reaches the layer with $f_w = f_p$ (f_p is the plasma frequency), the wave is reflected back to the sounder, which measures the time delay between the signal emission and the reception of its echo[21]. By knowing the exact altitude of the spacecraft with respect to the planet and the speed of the radar wave, one can infer the altitude at which the wave is reflected as well as the electron density characterized by this particular plasma frequency. This cycle is repeated to cover the whole spectrum between the local plasma frequency at the altitude of the spacecraft and the maximum plasma frequency of the topside by using a range of wave frequencies[7][21]. In the case of MARSIS set in active ionospheric sounding mode, the radar pulses emitted have frequencies between 0.1 and 5.5 MHz, to locate the maximum electron density of the Martian ionosphere at an altitude of $\sim$ 150 km.

If the frequency is further increased, the radio signal passes through the ionosphere and is reflected by the surface[7][8]. This shows a first limitation of the radar sounders for the probing of the

ionosphere as they can only probe the topside of the ionosphere to the maximum of the electron density, which is corresponding to the M2 layer[7][8][21]. The radar sounders can also use higher frequencies up to 30 MHz (depending on the instrument), allowing the radar pulses to go through the ionosphere and to probe the surface and the subsurface of the planet. In any case, a second constrain of the radar sounders is the high signal to noise ratio of the technique, limiting the data collection when the spacecraft is near its periapsis[21].

2.1.2 Ionospheric Effects on Radio Wave Propagation

The radar signal is not only reflected by the ionosphere due to the plasma but can be altered in four other ways[7][8]. While crossing the Martian ionosphere, it can experience (1) an increase in the time delay compared to the time expected when travelling at the speed of light in vacuum, (2) a distortion of the signal phase due to the frequency dependence of the refractive index (radar signals close to the critical frequency of the ionosphere), (3) an attenuation of the signal amplitude which is induced by the collisions of thermal electrons with the neutrals and (4) Faraday rotation effects over strong crustal magnetic field regions[7][24].

In the case of Mars' surface and subsurface observations by MARSIS and SHARAD, the frequencies used by these instruments are much larger than the expected ionospheric critical frequency of the "normal" ionosphere. Additionally, the crustal magnetic field is considered to be in general relatively weak in the regions observed by the radars[7]. This means that the main source of signal modification by the Martian ionosphere/atmosphere is the attenuation caused by the electrons. As shown by previous studies, the attenuation of the signal (A) is directly proportional to the electron density (Ne) and to the frequency of electron-neutral collisions (υ), all depending on the altitude (h)[7][8].

$$A(h) \propto Ne(h) \frac{\upsilon(h)}{(2\pi f_w)^2 + \upsilon^2(h)} \tag{2.1}$$

One can expect to have a large attenuation at altitudes where the collision frequency between neutral and electrons is large, thus where the neutral density and the electron density are both non-negligible. However, on one hand, the neutral density increases exponentially with decreasing altitude and is close to zero around 100 km of altitude, just under the ionosphere. On the other hand, the electron density is non-negligible in the M1 and M2 ionospheric layers. This means that under normal conditions when considering a usual ionospheric structure as described in Section I, the attenuation of the radar signal is low as there is nearly no overlap between the neutral and ionized regions and the radar instruments can operate without any issue[7][8][21].

During high solar activity periods, it was demonstrated that the increased SEP electron fluxes can enhance an additional ionization layer below the ionosphere at approximately 90 km. As proven by Witasse et al. 2001, the absorption caused by even a relatively low-density electron layer in the neutral atmosphere would result in more attenuation than in the main ionospheric layer M2, where the electron density reaches its maximum[7][8][24][25]. Furthermore, other studies of the Martian atmosphere have shown that additional ionization at altitudes below the two main electron peaks in the Martian ionosphere could result in the total absorption of the radar signal resulting in a blackout event[8]. In the case of Mars, the peak attenuation is reached when the signal frequency equals

the electron-neutral (CO_2 for the Martian atmosphere) collision frequency of the local plasma[7]. An example of the signal received by MARSIS under usual conditions and during a blackout event is shown in Figure 3.

It is worth to note that from the equation (2.1), the attenuation is also inversely proportional to the square of the radar signal frequency, meaning that low-frequency signals are more attenuated by Mars' ionosphere/atmosphere than high-frequency signals. This was observed by Lester et al. 2022 as MARSIS underwent more blackouts than SHARAD between 2006 and 2017 because MARSIS operates at frequencies five time smaller than SHARAD[8].

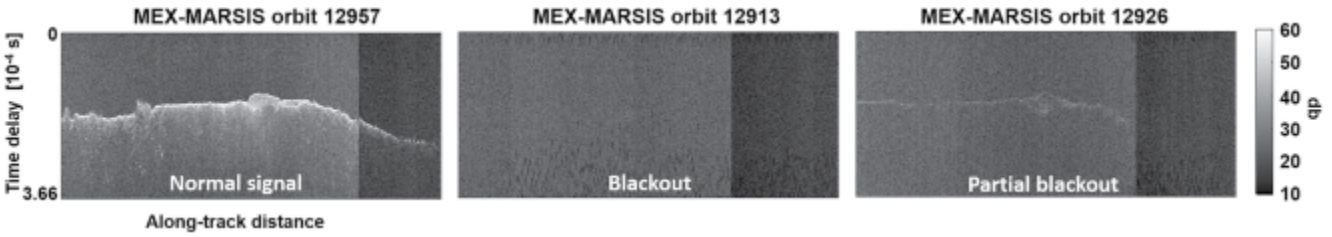

Figure 3: Examples of the radar signals received by MARSIS. The radar's received signal strength is plotted as a function of time delay and of the along-track distance. The left-hand panel is an example of a normal returned signal, the central panel is an example of the radar signal during a total blackout, and the right hand panel during a partial blackout[8].

2.2 Radio Occultation

Radio occultation is a remote measurement method using radio signals between a spacecraft and a ground station on the Earth. It is a bistatic radar configuration as the radar emitter is spatially separated from the radar receiver, distinguishing it from a monostatic radar.

As seen from the Earth, when the spacecraft's trajectory passes behind the limb of the planet, the spacecraft's radio signal sent to the ground station passes through the planet's ionosphere, then through its atmosphere until it is blocked by the planet's surface. This phase is called an ingress. The sequence is reversed as the spacecraft emerges from behind the planet. The radio signal passes first through the atmosphere, then through the ionosphere until it reaches the ionopause. This phase is called an egress. These two phases are represented by the diagram shown in Figure 4. In both cases, the passage of the signal through these media is called an occultation[5][18][19][26][27]. The changes of amplitude, frequency and phase of the radio signal caused by the passage through these media can provide information about their physical properties. These changes are caused by the attenuation of the signal combined with the change of the refractive index as the signal crosses different media[5][26].

The first radio occultation of Mars' atmosphere and ionosphere was carried by the Mariner IV spacecraft in 1965[4][5]. In this study, the radio occultation data that are used come from the Mars Express Radio Science Experiment (MaRS).

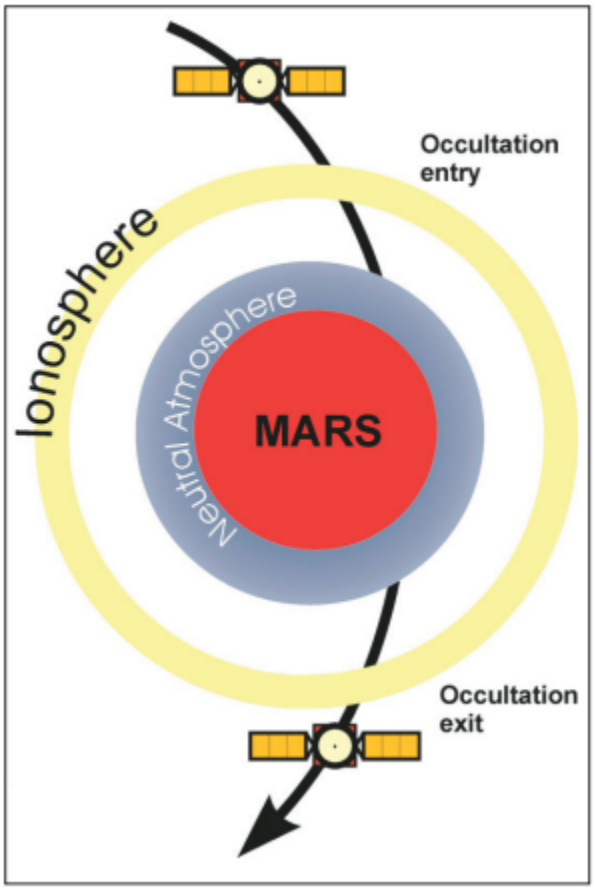

Figure 4: Diagram of the operational sequence of the two-way link used for sounding the atmosphere/ionosphere as seen from the Earth. The sequence is here shown as projected on the sky plane. During the ingress, the spacecraft enters the occultation and the signal passes the atmosphere from the top to the surface before being blocked by the planet. This process is reverse during the egress, as the spacecraft exits the occultation from the planet and the two-way radio link re-establishes [18].

2.2.1 Measurement Method and Signals Characteristics

There exist different type of radio occultations as different signals can be used during the occultation. In the case of MaRS, the high gain antenna (HGA) is equipped with transponders that allow to read a signal and to re-transmit it while applying a multiplying factor to the carrier frequency[18][19]. The ground station (the Deep Space Network in this case) sends an uplink radio signal to the spacecraft either in S-band (2.1 GHz) or in X-band (7.1 GHz). As MaRS uses two radio link modes, it is transponding the received radio signal in two coherent downlink signals. When a S-band uplink carrier frequency is received by MaRS, it is transponded downlink at S-band and X-band upon multiplication by the constant transponder ratios $k_{SS} = 240/221$ and $k_{SX} = 880/221$, respectively, in order to guarantee a ratio of the two downlinks of $880/240 = 11/3$. If the received uplink carrier frequency is in X-band, it is multiplied by $k_{XX} = 880/749$ and $k_{XS} = 240/749$ to arrive at X-band

and S-band downlink frequencies, respectively, with again the ratio of both frequencies is 880/240 = 11/3[18][19]. In this study, the uplink frequency is solely in X-band at f_{up} = 7.1 GHz. In this case, the downlink frequencies of the S-band and the X-band are respectively $f_{S,down}$ = 2.3 GHz and $f_{X,down}$ = 8.4 GHz. The construction of these radio signals frequencies is summarized by:

$$f_{S,down} = k_{XS} \cdot f_{up,received} \tag{2.2}$$

$$f_{X,down} = k_{XX} \cdot f_{up,received} \tag{2.3}$$

However, the uplink frequency received by the spacecraft $f_{up,received}$ is not equal to the one sent by the ground station. It is the result of the sum of the transmitted frequency f_{up}, the Doppler shift resulting from the relative motions of the Earth based transmitter and the spacecraft $\frac{v}{c} f_{up}$, and a net phase advance imposed by the turbulent solar wind plasma along the ray path Δf_{SW} [19].

$$f_{up,received} = \left(1 - \frac{v}{c}\right) f_{up} + \Delta f_{SW} \tag{2.4}$$

Additionally, if this signal is received during an occultation, one has to take account of the bending of the ray path due to the crossing of the ionosphere and/or the atmosphere. Since the transponder ratios k_{XS} and k_{XX} are constant, the ratio of the downlink signal frequencies is also constant and is equal to[18][19]:

$$\frac{f_{X,down}}{f_{S,down}} = \frac{k_{XX}}{k_{XS}} = k = \frac{11}{3} \tag{2.5}$$

It is important to note that the downlink signal is also modified by the same Doppler shift contributions, plasma perturbations and by the atmosphere and ionosphere bending in the same way as the uplink signal [19].

2.2.2 Observed Quantities and Frequency Residuals

Regardless of the mode used by the instrument, the quantities monitored by the ground station are the received carrier frequencies, the signal strength (received total power) and the polarisation of the radio signals[18]. These are the "raw" data and are referred as the Level-1 data. The frequency received by the antenna is reconstructed and calibrated for the propagation delay in transiting the Earth's troposphere and ionosphere. The frequency of the radio carrier is shifted according to the relative radial velocity between the spacecraft HGA and the ground station (classical Doppler shift). However, in the case of radio occultation, one would rather be interested by the relative phase shift that is experienced by the radio wave while it propagates through an ionised medium such as the ionosphere [18][19]. This second shift is much smaller than the classical unperturbed Doppler shift (fractions of Hertz compared with 28 kHz). In order to extract this small frequency shift from the total signal modification, a predicted "sky-frequency", which does not consider contribution from the propagation through the Mars atmosphere/ionosphere, is calculated and subtracted from the received downlink frequency to obtain frequency residuals[19][27].

The predicted frequency is computed by a complex force model that considers the gravitational forces of the planets themselves and of all the other objects considered as a third body that are

applied on the spacecraft. The model also accounts for non-gravitational forces, such as the solar radiation pressure, acting on the spacecraft based on the reconstructed spacecraft's orbit [19][27]. Other effects caused by the motion of Mars in its orbit, the motion and the rotation of the Earth, solid Earth tides, plate tectonics, the relativistic Doppler effect and the finite light time between transmission and reception of radio signals are also included in the calculations [19]. The quantity of interest of these calculations is the relative velocity Δv_r of the spacecraft with respect to the Earth along the line of sight. The Doppler shift induced by this relative velocity depends on the signal frequency f_0 (7.1 GHz for the uplink in X-band and 2.3 GHz or 8.4 GHz for the downlink respectively in S-band or in X-band) and is defined as [18][19]:

$$\Delta f = -\frac{\Delta v_r}{c} f_0 \tag{2.6}$$

where c is the speed of light. Using the relation between the uplink and the downlink frequency (2.3) with the definition of the predicted frequency of (2.4) while neglecting the solar wind contribution, the predicted frequency is then given by [19]:

$$\begin{aligned} f_{pred} &= f_{down} - \frac{\Delta v_{r,down}}{c} f_{down} \\ &= k f_{up} - k f_{up} \frac{\Delta v_{r,up}}{c} - k \left(f_{up} - f_{up} \frac{\Delta v_{r,up}}{c} \right) \frac{\Delta v_{r,down}}{c} \\ &= k f_{up} \left(1 - \frac{\Delta v_{r,up}}{c} - \frac{\Delta v_{r,down}}{c} \right) + k f_{up} \frac{\Delta v_{r,down}}{c} \frac{\Delta v_{r,up}}{c} \\ &\simeq k f_{up} \left(1 - \frac{\Delta v_{r,up}}{c} - \frac{\Delta v_{r,down}}{c} \right) \end{aligned} \tag{2.7}$$

with k being the ratio of the transponder constants $\frac{k_{XX}}{k_{XS}}$. The last equality comes from the approximation that second order terms of the relative velocity are negligible.
The relative velocity for the uplink and the downlink signal can be considered to be approximately equal so one would get:

$$f_{pred} = k f_{up} \left(1 - 2 \frac{\Delta v_r}{c} \right) \tag{2.8}$$

The frequency residuals f_r are equal to the difference between the received frequency and the predicted one. These are computed for each frequency as:

$$f_r = f_{received} - f_{pred} \tag{2.9}$$

These residuals contain all the frequency shifts that were not considered for the predicted frequency. These shifts arise from (1) orbit errors from gravitational and non-gravitational forces not considered in the prediction, (2) the bending of the ray path in the ionosphere and neutral atmosphere, (3) contributions from the planetary gravity field and (4) the gravitational attraction of Phobos on the spacecraft during flybys [19]. The orbit errors can be easily removed by a baseline fit on the first few minutes of raw data. The Earth's atmosphere and ionosphere are also contributing to shifts in the received frequency of the radio signal. The Earth's atmosphere contribution is corrected by models using some meteorological measurements such as the temperature, the pressure,

the humidity, ... collected at the ground station antenna site. As for the Earth's ionosphere contribution, it is corrected through the use of GPS observations, allowing to model the ionosphere[28].

For the ionosphere of Mars, a X-band signal received at the ground station has a net Doppler shift (which is in fact the frequency residuals)[19][29]:

$$df_{i,XX} = df_{i,Xup} \cdot k_{XX} + df_{i,Xdown} \tag{2.10}$$

where df is the Doppler shift with XX denoting that both uplink (up) and downlink (down) signals are in X-band and the 'i' index is denoting that the radio signal propagates through the ionosphere. Since the Doppler shift depends on the signal frequency, one has[29]:

$$\begin{aligned} df_{i,Xup} &\propto \frac{1}{f_{i,Xup}} \\ df_{i,Xdown} &\propto \frac{1}{f_{i,Xdown}} \end{aligned} \tag{2.11}$$

By dividing the first equation by the second in (2.11) and using the relation (2.3), one can express the Doppler shift ratio as:

$$\frac{df_{i,Xup}}{df_{i,Xdown}} = \frac{f_{i,Xdown}}{f_{i,Xup}} = k_{XX} \tag{2.12}$$

which can be rewritten as:

$$df_{i,Xup} = df_{i,Xdown} k_{XX} \tag{2.13}$$

By combining equations (2.10) and (2.13), one can express the net Doppler shift as a function of the k_{XX} ratio and the Doppler shift experienced by the downlink signal $df_{i,down}$ as:

$$df_{i,XX} = df_{i,Xdown}(1 + k_{XX}^2) \tag{2.14}$$

or:

$$df_{i,Xdown} = df_{i,XX} \frac{1}{(1 + k_{XX}^2)} \tag{2.15}$$

This means that from the data recorded at the ground antenna, one can determine the frequency residuals $df_{i,XX}$. This quantity divided by a constant is the one-way Doppler shift caused by the ionosphere in a X-band measurement at the downlink frequency. As it will be shown later in this section, this latter quantity is the foundation of the construction of the ionospheric profiles[29].

The same relations apply for a S-band downlink radio signal going through the ionosphere. The net Doppler shift can as well be expressed as a function of the downlink Doppler shift and the k_{XS} transponder ratio as[29]:

$$df_{i,XS} = df_{i,Sdown}(1 + k_{XS}^2) \tag{2.16}$$

or:

$$df_{i,Sdown} = df_{i,XS}\frac{1}{(1+k_{XS}^2)} \tag{2.17}$$

As there are two frequencies used for the radio link between the spacecraft and the ground station, one can compute the differential Doppler δf , for which Doppler shifts from motion or residual motion have been eliminated. Using (2.5), one gets that[19][29]:

$$\delta f = df_{i,XS} - \frac{3}{11}df_{i,XX} \tag{2.18}$$

The uplink contributions can be cancelled out when using the relation (2.10) and the equivalent relation for the S-band signal, giving:

$$\delta f = df_{i,Sdown} - \frac{3}{11}df_{i,Xdown} \tag{2.19}$$

By using the relation (2.5) to express the downlink frequency shift in X-band as the downlink frequency shift in S-band, one gets:

$$\delta f = df_{i,Sdown}(1 - \frac{9}{121}) \tag{2.20}$$

The main advantage of the differential Doppler is that it removes all non-dispersive noise sources, such as errors in the trajectory reconstruction or spacecraft's motions caused by fuel sloshing[29]. The differential Doppler is essentially equivalent to a one-way S-band downlink[19].

When considering the neutral atmosphere, the relations change as the refractivity does not depend on the frequency. One thus get for the X-band (and similarly for the S-band) that the net Doppler shift is expressed as:

$$df_n = df_{n,up} \cdot k_{XX} + dfn, down \tag{2.21}$$

Since in the neutral atmosphere, the relation (2.12) is reversed as $\frac{df_{i,Xup}}{df_{i,Xdown}} = \frac{1}{k_{XX}}$ one gets:

$$df_n = 2dfn, down \tag{2.22}$$

In this case, similarly to the ionospheric case, the frequency residuals are measured by the ground station. This quantity divided by two gives the one-way Doppler shift caused by the atmosphere at the downlink frequency[19][29]. This latter quantity is the foundation of the construction of the neutral atmospheric profiles[29].

The radio subsystem of the spacecraft is configured as X-band uplink and coherent dual-frequency downlink. About twenty minutes before the geometrical occultation of the spacecraft by the planet's atmosphere, the ground station starts to record the downlinks at X-band and S-band[19]. The actual sounding of the ionosphere and the neutral atmosphere by the radio signals occurs only during the last few minutes of the recording[19]. The Figure 5 shows the frequency residuals of a X-band signal measured by a ground station.

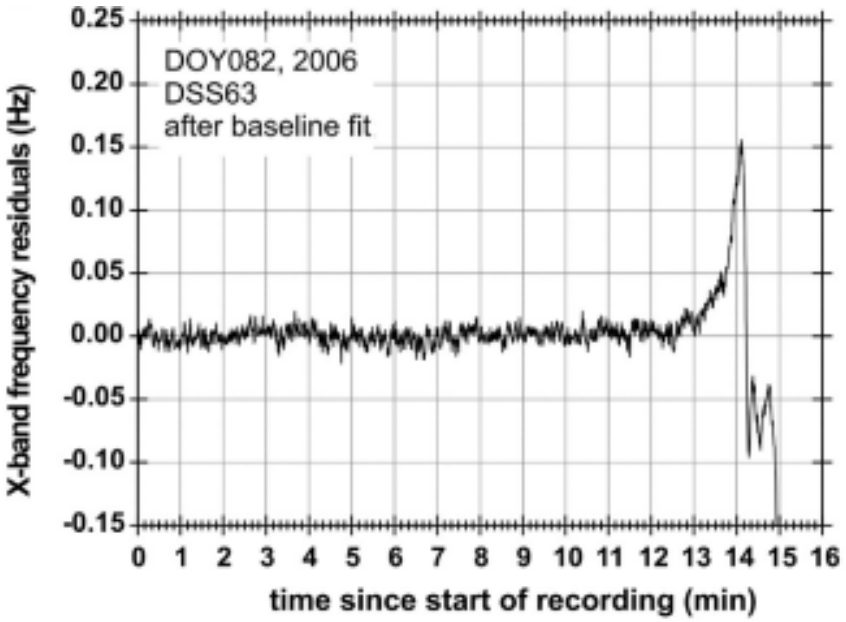

Figure 5: Frequency residuals at X-band from the occultation entry on DOY 082, 2006. The first baseline correction is applied by using the first ten minutes of the recording. These are subtracted from the "raw" residuals to correct any bias arising from contributions not considered in the prediction or from orbit errors. At 12.5 minutes, the first peak shows the beginning of the sensible ionosphere. The two peaks at 14 minutes and 14.2 minutes represent respectively the detection of the M2 and M1 layers. The frequency residuals drop to typically -10 Hz in the neutral atmosphere before getting blocked by the planetary surface[19].

2.2.3 Principles: From Frequency Residuals to Ionospheric/Atmospheric Refractivity

The way the Martian atmosphere and ionosphere are probed, through their effects on the radio carrier waves travelling between the spacecraft and the Earth during periods of occultation. These periods are when the spacecraft passes behind the Martian atmosphere or ionosphere in the sky-plane as seen from the Earth [19][30]. The occultation "season" can last a few weeks to a few months and depends on the orientation of the orbital plane of the spacecraft with respect to the Earth-Mars system. When passing through the atmosphere or ionosphere, the frequency of the radio signal is experiencing shifts which can be linked to the geometry of the ray path[18][19][30]. In Figure 5, the initial positive frequency shift is caused by the passage through the ionosphere. It causes a radially outward bending of the radio ray path as the frequency shift reaches values of up to one Hertz at X-band, depending on the electron density within the main ionospheric layer. Thereafter, as the radio signal propagates through the neutral atmosphere, the ray path bends radially inward and the frequency shift becomes negative and may reach -10 Hz as the signal gets close to the planet's surface[19]. This phenomenon is caused by the different refractive indexes of the two media. The ionospheric electrons decreases the refractive index below the vacuum value of 1, whereas the presence of neutrals increases the refractive index above the vacuum value of 1[5][20][30].

The frequency residuals can be used to determine the bending angle of the ray path caused

by the different refractivities of the atmosphere and the ionosphere. Additionally, to compute the bending angle profiles, one needs to know the state vector of the Earth and of the spacecraft accurately as these are the foundation of the occultation geometry. Figure 6 shows a diagram representing the classical geometry of an occultation. This geometry is characterized by a triangle ABC where the Earth is at A, Mars is at B and the spacecraft is at C. The refracted ray is following a bended ray path between C and A, corresponding to the downlink signal [19][20]. Since the refractive atmosphere and ionosphere are spherically symmetric, one can consider this bended ray path to lie in the plane define by the points A, B and C. The ray asymptotes correspond to the two half straight lines starting respectively from C and A that follow the ray path signal before and after the bending of the signal path. These asymptotes are characterized by a single impact parameter a since the atmosphere/ionosphere are spherically symmetric [30]. The latter parameter corresponds to the shortest distance between each asymptote and the center of Mars, located at B[19][30]. The angle α formed by the two asymptotes corresponds to the bending angle of the signal. The direct line of sight between the ground station at A and the spacecraft at C is the ray path of a signal that would not be affected by the atmosphere nor by the ionosphere of Mars. If the signal travels along the latter path, the frequency residuals are null[19].

The aim of the operation is to compute the bending angle of the ray. This bending angle can be expressed as the sum of the two angles formed by the line of sight and the asymptotes, β_r and δ_r such as:

$$\alpha = \beta_r + \delta_r \tag{2.23}$$

where β_r and δ_r are respectively the angle between the line of sight and the ray asymptote passing by the spacecraft and the angle between the line of sight and the ray asymptote passing by the ground station (Figure 6). Using classical physics, the frequency residuals due to the bending of the ray path can be expressed as[19]:

$$\begin{aligned}\Delta f =& \frac{f_0}{c}\left[v_{r,Earth} sin\left(\delta_e + \delta_r\right) + v_{z,Earth} cos\left(\delta_e + \delta_r\right) - v_{r,s/c} sin\left(\beta_e + \beta_r\right) - v_{z,s/c} cos\left(\beta_e + \beta_r\right)\right] \\ & - \frac{f_0}{c}\left[v_{r,Earth} sin\left(\delta_e\right) + v_{z,Earth} cos\left(\delta_e\right) - v_{r,s/c} sin\left(\beta_e\right) - v_{z,s/c} cos\left(\beta_e\right)\right]\end{aligned} \tag{2.24}$$

where f_0 is the carrier frequency in X or S-band and c is the speed of light. Using the system of coordinates introduced in the Figure 6, the velocity components of the Earth and of the spacecraft are respectively $v_{r,Earth}$, $v_{z,Earth}$ and $v_{r,s/c}$,$v_{z,s/c}$. The different angles from (2.24) are referred in the Figure 6. The first bracket corresponds to the frequency shift of the signal taking the true bended ray path and the second bracket to the frequency shift of the signal along the line-of-sight between the ground station and the spacecraft.

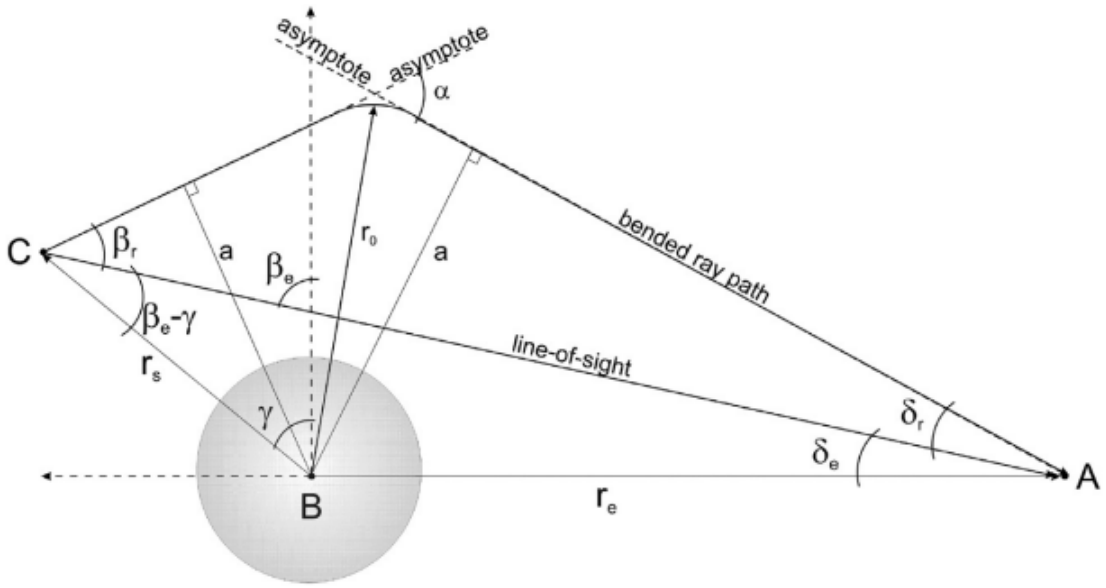

Figure 6: This diagram represents the exaggerated bending of the ray path due to the refractivity of the atmosphere. The points A, B and C represent respectively the Earth, Mars and the spacecraft in a two-dimension coordinate system centred on Mars. The z-axis is chosen to be along the line joining Mars to the Earth (in the A to B direction) and the r-axis is perpendicular to it, in the occultation plane. A radio signal would travel either along the line of sight or along the bended ray path respectively depending on whether the planet has an atmosphere or not. In the case of Mars, there is one. An extra frequency shift occurs relative to the frequency shift along the line of sight, which corresponds to the second bracket of equation (2.24). The bending angle α is computed from the extra frequency shift and the occultation geometry. The impact parameter a is the point of closest approach of the asymptotes to the center of Mars, not to be confused with the r_0 corresponding to the closest approach of the bended ray path to the planet's center. r_0 is also called the bending radius. The geometry angles need to be computed from the known ephemerides of Mars and the Earth and from the spacecraft orbit file for each time step of the observation, stressing the need to have a great accuracy on these latter values if one wants high precision atmospheric profiles when using radio occultation[19].

Using the known ephemerides of the Earth, of Mars and of the spacecraft, one can compute the velocity components and the angles introduced in Figure 6. The impact parameter a is defined as:

$$\begin{aligned} a &= r_e sin(\delta_e + \delta_r) \\ &= r_s sin(\beta_r + \beta_e - \gamma) \end{aligned} \tag{2.25}$$

where r_e is the distance between the center of the Earth and the center of Mars, r_s is the distance between the center of Mars and the spacecraft and γ the angle between the r-axis and the line joining the spacecraft and Mars. The angles β_e and δ_e, respectively the angle between the line of sight and the r-axis and the angle between the line of sight and the AB segment, are known

from the ephemerides of the three bodies[19][30]. Since the distances r_e and r_s are also known from the ephemerides, the only unknown angles remaining are β_r and δ_r. By using the equations (2.24) and (2.25) simultaneously, one can determine these angles. As first shown by Fjeldbo in 1964, one can perform the computation of these angles by replacing β_r and δ_r by $\beta_r + \Delta\beta_r$ and $\delta_r + \Delta\delta_r$ and then by linearising these equations for $\Delta\beta_r$ and $\Delta\delta_r$ such that[5][30][31]:

$$b_{11}\Delta\beta_r + b_{12}\Delta\delta_r = k_1 \tag{2.26}$$

$$b_{21}\Delta\beta_r + b_{22}\Delta\delta_r = k_2 \tag{2.27}$$

where the parameters b_{11}, b_{12}, b_{21}, b_{22}, k_1 and k_2 are various rearrangements of the previous angles, velocities, distances as well as the frequency residuals expressed in the equations (2.24) and (2.25)[30]. These angles thus depend directly on the frequency shift caused by the bending of the ray path[19].

The equations (2.26) and (2.27) can be used to compute β_r and δ_r as a function of time. The approach proposed originally by Fjeldbo consists at first to use rays passing outside of the atmosphere, where these two angles are equal to zero as there is no bending. One can then proceed with rays of lower altitude which start to penetrate the top of the atmosphere as the spacecraft moves behind Mars' atmosphere. For each ray, it is possible to make an estimation of the angles β_r and δ_r based on the previous rays and then to compute the two corrections $\Delta\beta_r$ and $\Delta\delta_r$ using the equations (2.26) and (2.27). The newly computed values of β_r and δ_r can then be reinserted in the set of linearised equations to determine the next set of the corrections. This iterative process can be proceeded as many time as needed until the desired precision is reached, and this for each ray[30]. When these angles are finally computed for each ray, the bending angle can be easily computed using (2.23) leading to the computation of the vertical profile of the bending angle in the ionosphere/atmosphere of the planet.

Once the bending angle is known, the next important step is the computation of the refractivity of the medium through which the signal travelled. One can use the ray inversion technique, also described by Fjeldbo. This method consists of assuming that the function of the bending angle $\alpha(a)$ depends on the impact parameter a and consists of K points determined by the Doppler data points measured[30]. One can thus consider that the Martian atmosphere is composed of K spherical layers, each one with constant refractivity and constant thickness. A ray signal passes tangentially through the middle of each of these layers. For clarity, Figure 7 only illustrates the m^{th} ray passing through this kind of atmosphere and being tangential to the m^{th} layer. Let r_m and n_m be respectively the radius and the refractive index of the m^{th} layer. As presented on the Figure 7, since the ray is tangentially passing through the middle of the layer, the bending radius of the m^{th} ray $r_{0,m}$ is directly related to the radii of the m^{th} and $m+1^{th}$ layers through the relation[30][31]:

$$r_{0,m} = \frac{1}{2}\left(r_m + r_{m+1}\right) \tag{2.28}$$

To represent the ray path, one needs to know the angles of incidence (i) and the refractive angles (j) at each boundary between each layer. For example, the angle of incidence of the m^{th} ray entering the n^{th} layer is denoted $i_{m,n}$ and the angle of refraction of this same ray crossing this same layer is denoted $j_{m,n}$.

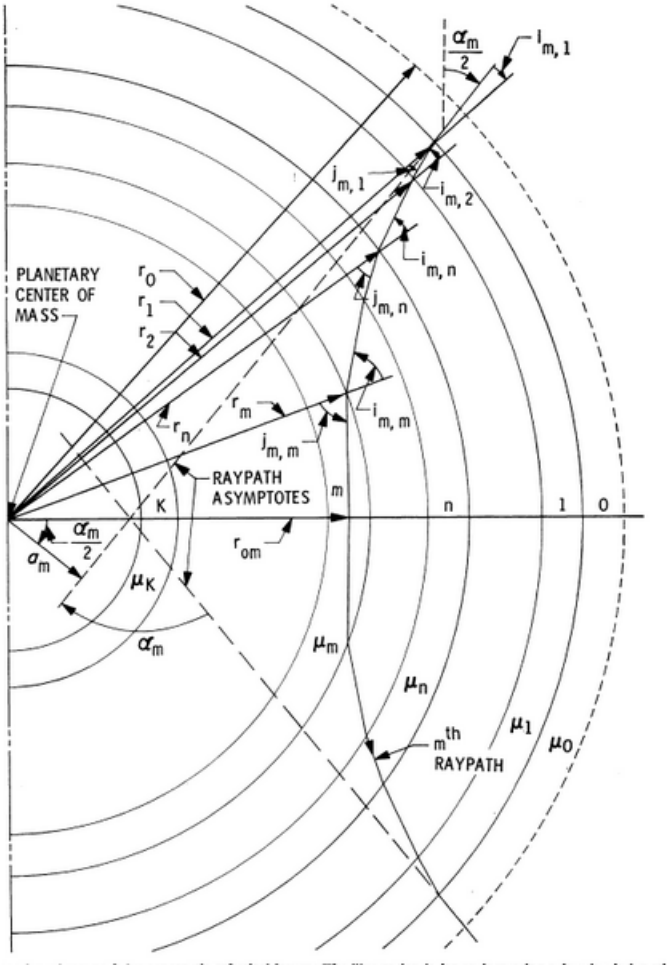

Figure 7: Representation of the refraction of a ray path crossing m of the K concentric layers of atmosphere. The refractive index increases with height in this figure. Note that even if the bending of the ray is not in the same way that in the Figure 6, the process of evaluation of the angles and thus of the refractivity, remains correct. As a reminder, the bending orientation depends on the nature of the medium, either the atmosphere or the ionosphere[30].

One can then apply the laws of sines and Snell's law for the m^{th} ray crossing the first boundary to obtain the following relations:

$$a_m = r_1 sin(i_{m,1}) \tag{2.29}$$

$$sin(i_{m,1}) = n_1 sin(j_{m,1}) \tag{2.30}$$

$$\psi_{m,1} = \frac{1}{2}\alpha_m + i_{m,1} - j_{m,1} \tag{2.31}$$

where a_m is the impact parameter of the m^{th} ray, α_m is the bending angle of this same ray and $\psi_{m,1}$ is the angle at which the m^{th} ray must be bent before it is traced from the first layer to

the point of closest approach of the ray[30][31]. It is here assumed that the refractive index is one outside of the atmosphere. These relations can be generalised for the n^{th} boundary such that:

$$r_n sin(i_{m,n}) = r_{n-1} sin(j_{m,n-1}) \tag{2.32}$$

$$n_{n-1} sin(i_{m,n}) = n_n sin(j_{m,n}) \tag{2.33}$$

$$\psi_{m,n} = \psi_{m,n-1} + i_{m,n} - j_{m,n} \tag{2.34}$$

At the m^{th} boundary, $\psi_{m,m} = 0$ by definition as the ray is reaching the point of closest approach. This means that at the m^{th} layer, the relation (2.34) becomes:

$$0 = \psi_{m,m-1} + i_{m,m} - j_{m,m} \tag{2.35}$$

These relations can be used to link the bending angle profile to the refractive index and to the radius of each layer. The zeroth layer is defined as the first layer above the atmosphere of the planet. The refractive index of this layer is thus equal to 1 and there is no bending angle so $\alpha_0 = 0$. The radius of this layer can then be expressed as :

$$r_0 = \frac{1}{2}(a_0 + a_{-1}) \tag{2.36}$$

with a_0 and a_{-1} the impact parameters of the last two rays that miss the top atmospheric layer. In this case, they also correspond to the closest distances separating each ray to the center of the planet[30]. Using the relation (2.28), one can determine the radius of the first layer as:

$$r_1 = 2a_0 - r_0 \tag{2.37}$$

One can study the first ray crossing the first layer, characterized both by the index 1 and set $\psi_{1,0} = \alpha_1/2$ in the equations (2.32) - (2.34). This allows to express the refractive index of the first layer as:

$$n_1 = a_1 \left[r_1 sin\left(\alpha_1/2 + sin^{-1}\left(\frac{a_1}{r_1} \right) \right) \right]^{-1} \tag{2.38}$$

Knowing that $j_{1,1} = \alpha_1/2$, the distance of closest approach of this first ray can be computed by using the general relation:

$$r_{0,m} = r_m sin(j_{m,m}) \tag{2.39}$$

Using this relation and the quantities computed for the first layer, it is possible to find the radius of the second layer by using the relation (2.28). These computations can be applied iteratively for each ray and thus for each layer, allowing to derive the vertical profile of the refractive index for the whole atmosphere[30]. The general expressions resulting from this iterative process express the refractive index of the m^{th} layer n_m and its radius r_m using the quantities of the m^{th} and of the $m-1^{th}$ layer such that:

$$r_m = 2r_{0,m} - r_{m-1} \tag{2.40}$$

$$n_m = n_{m-1} \frac{r_{m-1} sin(j_{m,m-1})}{r_{m-1} sin\left[\psi_{m,m-1} + sin^{-1}\left((r_m/r_{m-1}) sin(j_{m,m-1})\right)\right]} \tag{2.41}$$

It is worth noting that this method uses the simplification that the refractive index is constant inside each layer. A more accurate approach would be the use of a refractive index that is allowed to change along both the horizontal and the vertical axis.

However, even if the method described above and by the Figure 7 allows to trace the ray path and to compute the refractive index of each layer, all the parameters at stake such as the angle of refraction, the angle of incidence or even the radius of the first layer are not always exactly known. Additionally, this gives a discrete profile which is not realistic. It is thus important to have a relation directly linking the bending angle to the refractive index while using the previous relations. The Figure 8 represents the geometry of the ray path and the parameters that are used when representing the ray path with the polar coordinates (r, ϕ)[30][31].

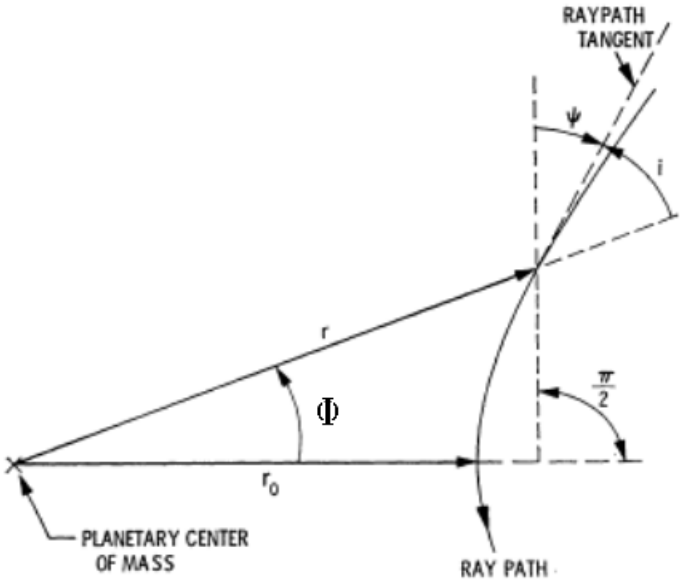

Figure 8: Representation of the ray path geometry in polar coordinates[30].

In the reference system of the Figure 8, the angle if incidence i is expressed as:

$$tan(i) = r \frac{d\phi}{dr} \tag{2.42}$$

By multiplying the equations (2.29), (2.30) and (2.32) together, it is possible to obtain a relation for the first layer. One can do the same for all the corresponding relations for all the other boundaries between the first and the n^{th} layer in order to obtain a new relation for the angle of incidence i such that:

$$a_n = n_{n-1} r_n sin(i_{m,n}) \tag{2.43}$$

If one considers an infinite number of layers, the above relation can be applied to an atmosphere with a refractive index n that is a continuous function of the radius r so that:

$$a = nrsin(i) \tag{2.44}$$

The relation (2.44) is known as the Bouger's rule[19][30]. This relation implies that at the point of closest approach, one has that:

$$a = n(r_0) r_0 \tag{2.45}$$

The Figure 8 shows that $i + \phi + \psi = \pi/2$ and that the differential of these angles are related as:

$$d\psi = -di - d\phi \tag{2.46}$$

By differentiating the equation (2.44), one can find another expression of di such that:

$$di = -\frac{a(n + (dn/dr)r)dr}{nr\left[(nr)^2 - a^2\right]^{1/2}} \tag{2.47}$$

Using the equations (2.42) and (2.44) allow to express ϕ without i and its differential can then be expressed as:

$$d\phi = \frac{adr}{r\left[(nr)^2 - a^2\right]^{1/2}} \tag{2.48}$$

By combining the three previous equations, $d\psi$ can be redefined as:

$$d\psi = \frac{a}{\left[(nr)^2 - a^2\right]^{1/2}} \frac{dn}{dr} \frac{dr}{n} \tag{2.49}$$

It is then possible to integrate $d\psi$ along the ray path. This integration expresses the angular deflection of the ray, which is the bending angle, as:

$$\alpha(a) = 2a \int_{r=r_0}^{r=\infty} \frac{dn}{ndr} \frac{dr}{\left[(nr)^2 - a^2\right]^{1/2}} \tag{2.51}$$

This last relation is in fact an Abel transform and allows to link the bending angle to the refractive index[19][30]. However, it would be preferable to have a relation that expresses the refractive index as a function of the bending angle rather than the expression (2.51). In order to find such an expression, one can reverse the relation (2.51) by introducing a dummy variable $x = nr$. The

integration now yields:

$$\alpha(a) = 2a \int_{x=a}^{x=\infty} \frac{dn}{ndx} \frac{dx}{[x^2 - a^2]^{1/2}} \tag{2.52}$$

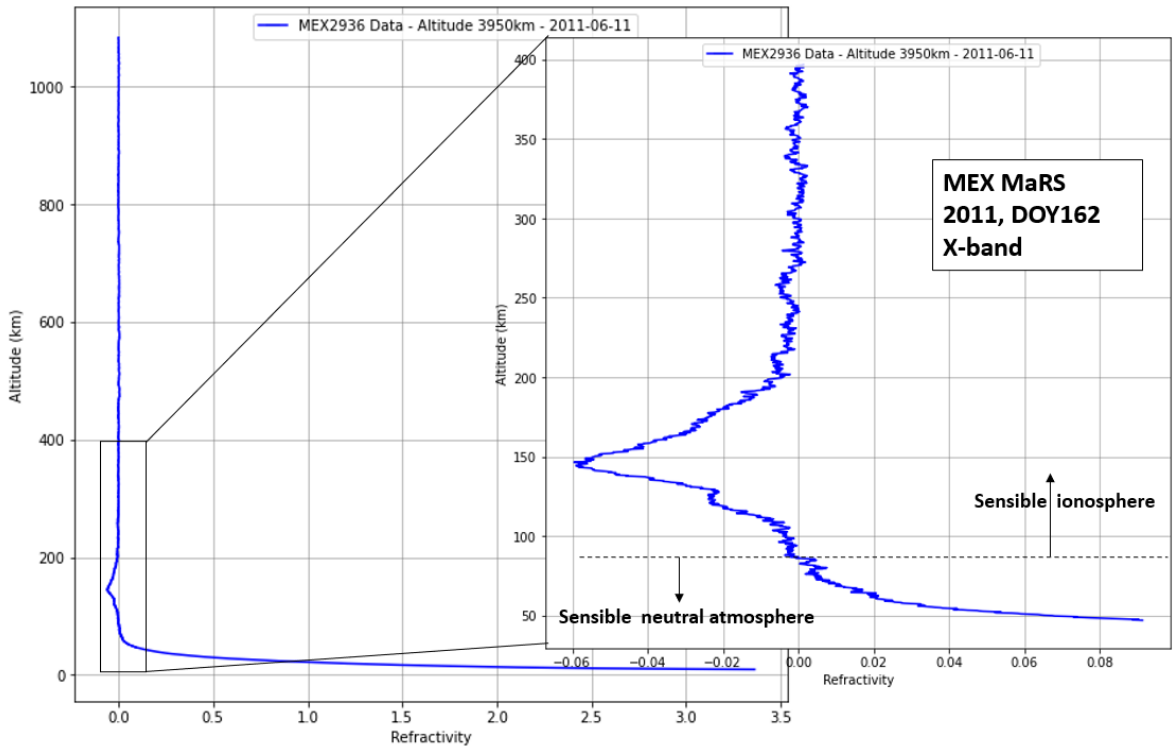

Figure 9: Example of a refractivity profile retrieved through an occultation measurement performed by MaRS instrument on board of MEX on the 11th of June 2011. This occultation is performed over the whole atmosphere/ionosphere, starting from the surface up to an altitude of 1083 km and thus above the ionopause. A baseline fit was performed on the profile to set the top of the density profile at zero, as it is fair to suppose that the electron density is zero at high altitude over the ionosphere. The ionosphere is characterized by a negative refractivity above 86 km, as the electrons induce a refractive index of the media that is smaller than 1. Under 86 km, the refractivity changes sign and becomes positive. This is a characteristic of the neutral atmosphere which has a refractive index above 1. At 86 km, the two media induce opposite refractivities generating a total refractivity equal to zero. The propagation of the radio wave is dominated by the ionosphere and the neutral atmosphere respectively above and below that altitude.

With the same notations as used previously, one can consider the impact parameter a_1 of the ray passing through the first layer with a distance of closest approach $r_{0,1}$. By multiplying both sides of (2.52) by $(a^2 - a_1^2)$ and by integrating them with respect to a from a_1 to infinity, one gets:

$$ln(n(r_{0,1})) = \frac{1}{\pi}\int_{a=a_1}^{a=\infty} \frac{\alpha(a)}{(a^2 - a_1^2)^{1/2}} da \tag{2.53}$$

This relation can be generalised for any layer such that:

$$ln(n(r_{0,j})) = \frac{1}{\pi}\int_{a=a_j}^{a=\infty} \frac{\alpha(a)}{(a^2 - a_j^2)^{1/2}} da \tag{2.54}$$

where $n(r_{0,j})$ is the refractive index at the point of closest approach to Mars with a distance $r_{0,j}$, along the ray path with impact parameter a_j [19][30][31][32]. Taking the exponential of the equation (2.54) gives:

$$n(r_{0,j}) = exp\left[\frac{1}{\pi}\int_{a=a_j}^{a=\infty} ln\left(\frac{a}{a_1} + \left[\left(\frac{a}{a_1}\right)^2 + 1\right]^{1/2}\right)\frac{d\alpha}{da} da\right] \tag{2.55}$$

The refractivity μ is related to the refractive index as $\mu = n(r) - 1$ and can be easily computed since the refractive index is known for the whole atmosphere. This means that after using all the above relations, it is possible to compute the refractivity as well as the associated asymptotic impact parameter a, the bending angle α and the ray distance of closest approach r_0 and this, for each time step of the occultation[19]. This allows to retrieve the vertical atmospheric and ionospheric profiles of the refractivity, as presented in the Figure 9. At a certain altitude r, the total refractivity can also be expressed as the sum of the neutral and of the electronic refractivities, respectivly denoted μ_n and μ_e [26]:

$$\mu(r) = \mu_n(r) + \mu_e(r) \tag{2.56}$$

In the Figure 9, it is clear that at a certain altitude corresponding to the transition region between the ionosphere and the neutral atmosphere (86 km in this case), the refractivities induced by both media cancel out. This can also be expressed as $\mu_n(r_b) = -\mu_e(r_b)$ where r_b is the altitude of the atmosphere/ionosphere boundary.

2.2.4 Deriving Density, Pressure and Temperature Profiles

The refractivity can be used to derive the density of both the ionosphere and of the neutral atmosphere. For the ionosphere, the refractivity is dependant of the electron density whereas the refractivity of the neutral atmosphere depends on the neutral density[19]. For the ionosphere, the refractivity is proportional to the electron density as [26]:

$$\begin{aligned} \mu_e &= -\frac{N_e(r)e^2}{8\pi^2 m_e \epsilon_0 f^2} \\ &= -\frac{40.31 \cdot 10^6 m^3 s^{-2}}{f^2} N_e(r) \end{aligned} \tag{2.57}$$

where N_e is the electron density, e is the elementary charge, m_e is the mass of an electron, ϵ_0 is the permittivity of the free-space and f is the frequency of the radio signal.

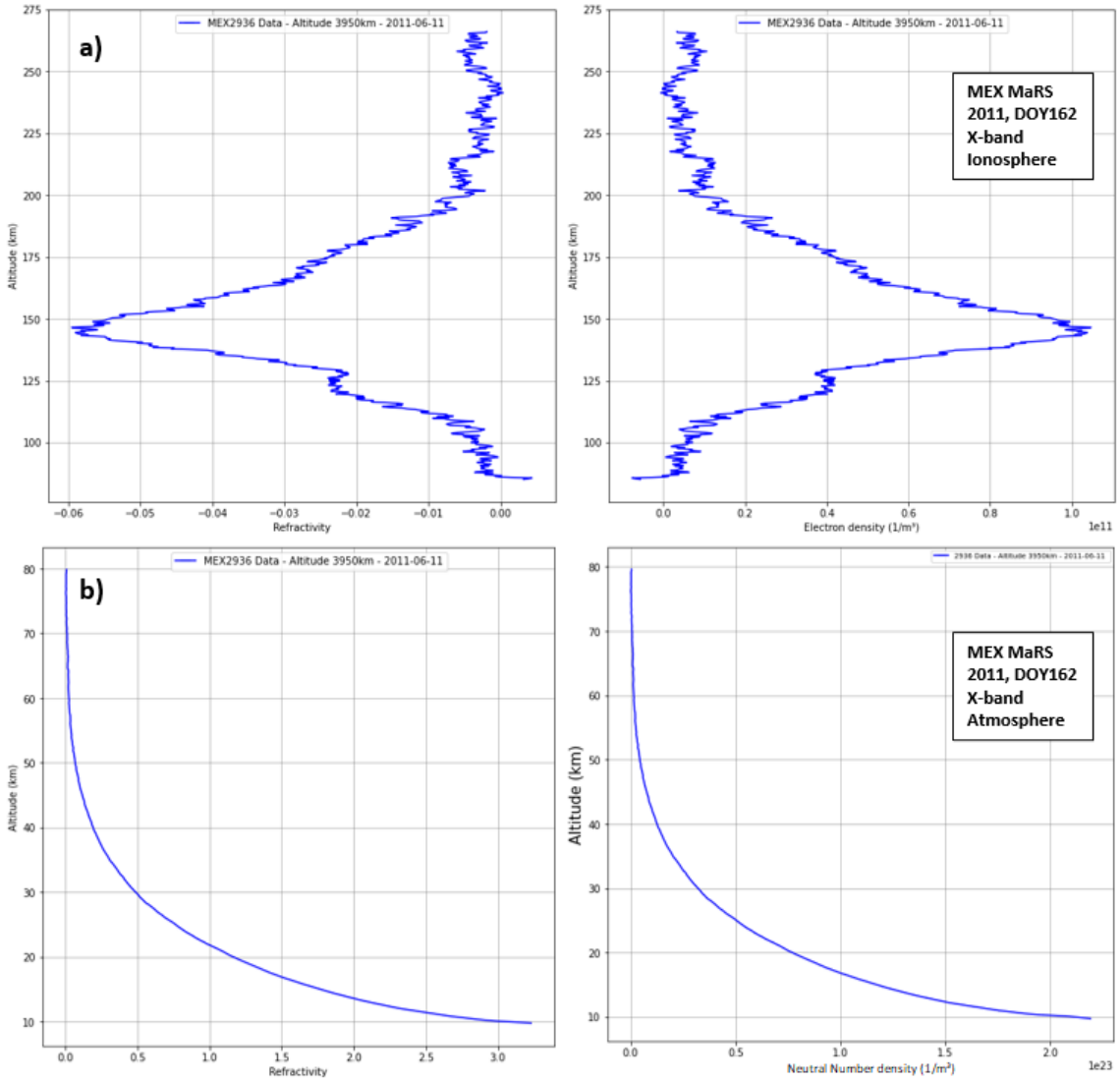

Figure 10: Comparison between a) an ionospheric refractivity (left) and an electron density (right) profiles retrieved through an occultation measurement performed by MaRS instrument on board of MEX on the 11th of June 2011. b) Same comparison but for the neutral atmosphere. Both density profiles are very similar to their respective refractivity profiles due to the proportionality between the two quantities. The ionospheric refractivity profile is a "mirror image" of the density profile because of the minus sign in (2.57).

Similarly for the atmosphere, the refractivity can be related to the neutral number density by

the equation:

$$\mu_n = C_1 k N_n = \kappa N_n \tag{2.58}$$

where N_n is the neutral number density, C_1 is a constant depending on the atmospheric composition, k is the Boltzmann constant and $\kappa = C_1 k$ is a single constant representing the refractive volume of the atmosphere[19]. This refractive volume is only depending on the constituent of the atmosphere but not on the dust or the aerosols as these are unnoticed by the high frequency radio signal. For a well-mixed atmosphere composed of 95.3% of CO_2, 2.7% of N_2 and 1.6% of Ar as the Martian atmosphere, the value of $C_1 = 1.306 \cdot 10^{-6} Km^2/N$ and the value of $\kappa = 1.804 \cdot 10^{-29} m^3$ [6][19][26]. The neutral number density computation is thus very dependant on its composition and an accurate knowledge of this composition is crucial in order to derive correct neutral number density profiles[19][26]. It is worth noting that the refractivity depends on the frequency of the signal when passing through the ionosphere but this is not the case in the atmosphere.

By knowing the total refractivity profile and by using the relations (2.56), (2.57) and (2.58), one can retrieve the total density profile. By looking at the last three relations, it is clear that, since in the ionosphere the electron density is greater than the neutral density by several orders of magnitude, the refractivity is mainly caused by the electrons and thus μ_n is negligible compared to μ_e. However, in the neutral atmosphere, the neutral density is much greater than the electron density, meaning that μ_e is negligible compared to μ_n. Figure 10.a and b show respectively ionospheric and atmospheric vertical profiles of the refractivity (left) and of the respective densities (right). It is clear that the refractivity profiles are very similar to the density profiles as they are directly proportional through the relations (2.57) and (2.58)[26].

The refractivity measurement can also be used to derive the pressure and the thermal structure of the atmosphere. Assuming an atmosphere at hydrostatic equilibrium, one can demonstrate that:

$$dp = N(z)\bar{m}(z)g(z) \tag{2.59}$$

where dp is the pressure differential, $N(z)$ is the neutral number density at altitude z, $\bar{m}$ is the mean molecular mass and $g(z)$ is the gravitational acceleration at altitude z [33]. As a simplification, one can assume that the mean molecular mass is constant over the whole atmosphere with $\bar{m} \simeq 7.221 \cdot 10^{-26} kg$ since the atmosphere is well-mixed [6][33][34]. When solving for $p(z)$, the pressure at altitude z, this equation yields:

$$p(z) = p_0 + \bar{m} \int_z^{z_0} N(z')g(z')dz' \tag{2.60}$$

where p_0 is the pressure at the boundary. By using the relation between the pressure, the density and the temperature given by the ideal gas law:

$$p(z) = N(z)kT(z) \tag{2.61}$$

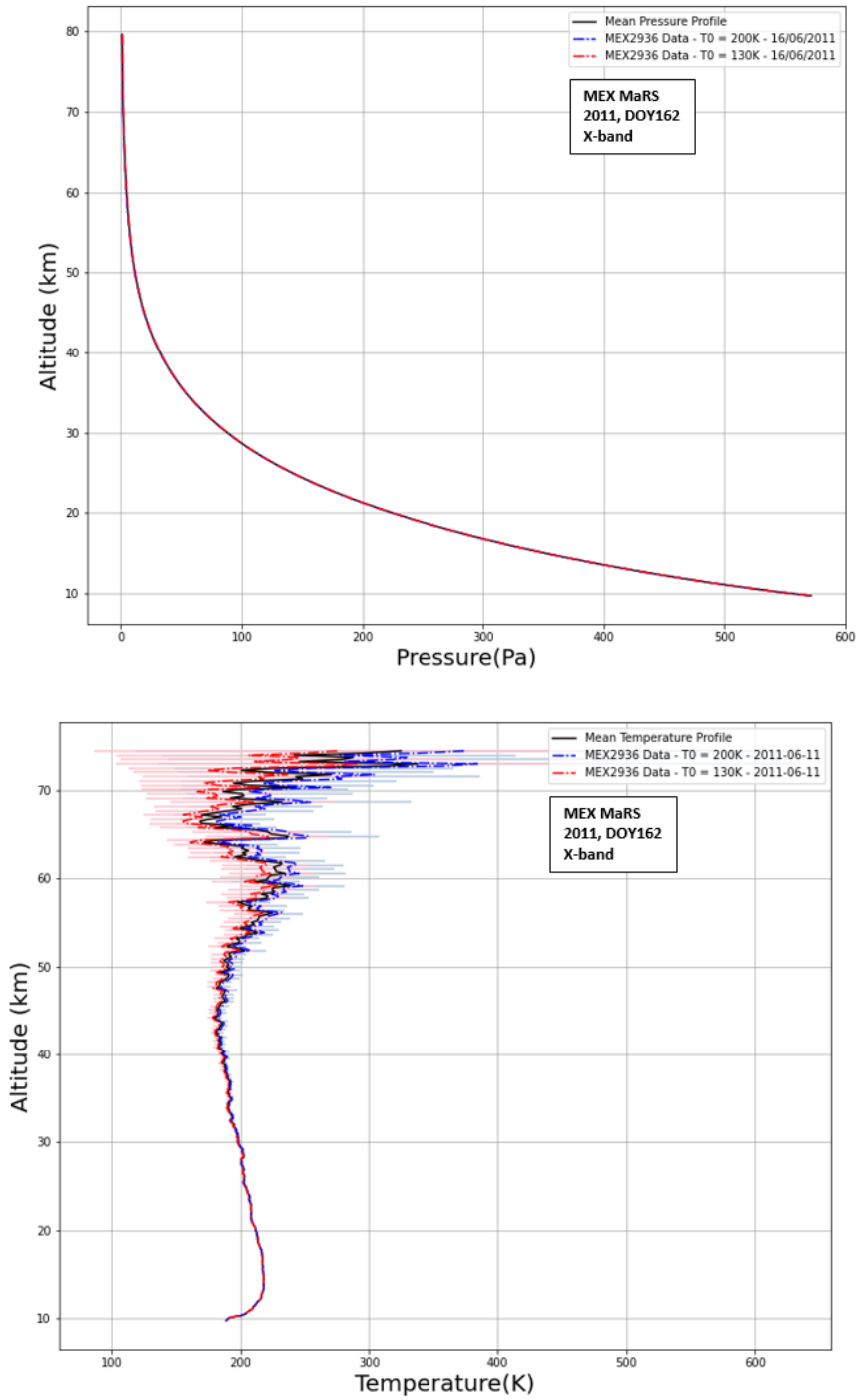

Figure 11: Typical pressure (top) and temperature (bottom) profiles of the Martian atmosphere acquired with MEX radio occultation measurement. These profiles were computed using the above method. The red profiles correspond to the profiles initiated with a boundary temperature of T_0 =130 K at 80 km altitude and the blue profiles correspond to the ones initiated with a boundary temperature of T_0 =200 K. The error bars are plotted in respectively light red and light blue and are computed as explained in the subsection 2.2.5. The black profiles correspond to the respective mean profiles of the blue and red ones.

one can rewrite the relation (2.60) as:

$$p(z) = N_0 k T_0 + \bar{m} \int_z^{z_0} N(z') g(z') dz' \tag{2.62}$$

or

$$T(z) = \frac{T_0 N_0}{N(z)} + \bar{m} \frac{1}{k N(z)} \int_z^{z_0} N(z') g(z') dz' \tag{2.63}$$

where N_0, $N(z)$ and T_0, $T(z)$ are respectively the densities and the temperatures at the boundary and at altitude z [6][19][26][33]. This means that with a prior knowledge of the constituent of the atmosphere and the density profile, it is possible to compute both the pressure and the temperature profiles of the atmosphere. It is important to notice that it is also necessary to have an initial boundary condition to initiate the profiles computations [6][34]. The Figure 11 shows typical pressure and temperature profiles retrieved through this method with a refractivity profile from a MEX measurement.

2.2.5 Uncertainties on the Ionospheric and Atmospheric Profiles

As for any measurement, some uncertainties exist for the quantity that is measured through radio occultation, being the frequency residuals. These are influenced by the thermal noise and by the phase noise. Some thermal noises ($\sigma_{thermal}$) are produced at all stages of the experiment, including by each transmitter and receiver. The phase noise (σ_{phase}) depends on multiple factors such as the instabilities of all reference oscillators used in the experiment and the variations in the refractive index in the terrestrial atmosphere, the terrestrial ionosphere and the plasma in the interplanetary medium [35]. The uncertainty on the frequency residuals $\sigma_{\Delta f}$ depends on latter quantities as:

$$\sigma_{\Delta f} = \sqrt{\sigma_{thermal}^2 + \sigma_{phase}^2 f^2} \tag{2.64}$$

where f is the frequency of the signal. As explained by Withers (2010), for the small bending angles, the frequency residuals can be approximated as [35]:

$$\frac{\Delta f}{f} \simeq \frac{V \alpha}{c} \tag{2.64}$$

where V is the relative speed between the spacecraft and the ground station, α is the bending angle and c is the speed of light.

One can assume that in a neutral atmosphere or in the top of an ionosphere, the refractivity, which is proportional to the electron density or to the neutral number density, decreases exponentially with increasing altitude[35]. Similarly to the hydrostatic equilibrium, this can thus be expressed as:

$$\mu(r) = \mu_0 exp\left(\frac{-(r - r_0)}{H}\right) \tag{2.65}$$

where μ_0 is the refractivity at r_0 with a scale height H. Since the refractivity can be expressed as a function of the refractivity index as $\mu = (n(r) - 1)$, one can show that:

$$\frac{dln(n)}{dr} = \frac{-\mu_0}{H} exp\left(\frac{-(r-r_0)}{H}\right) \tag{2.66}$$

Using this, the equation (2.51) can be re-expressed as:

$$\alpha(a) = \frac{2a\mu_0}{H} \int_{r=r_0}^{r=\infty} exp\left(\frac{-(r-r_0)}{H}\right) \frac{dr}{\left[(nr)^2 - a^2\right]^{1/2}} \tag{2.67}$$

In neutral atmospheres with pressures less than hundreds of bars and in ionospheres, the refractivity is such that $|\mu| << 1$ meaning that the ray path is not bent a lot[35]. Under such conditions, one can approximate that the closest distance to the ray r_0 is nearly the impact parameter a, corresponding to the same ray, and that nr is approximately r, so that:

$$\alpha(a) = \frac{2a\mu_0}{H} \int_{r=a}^{r=\infty} exp\left(\frac{-(r-a)}{H}\right) \frac{dr}{(r^2 - a^2)^{1/2}} \tag{2.68}$$

The solution of this the above equation can be expressed as[35]:

$$\alpha(a) = \frac{2a\mu_0}{H} exp\left(\frac{a}{H}\right) K_0\left(\frac{a}{H}\right) \tag{2.69}$$

where $K_0\left(\frac{a}{H}\right)$ is the Bessel function of the second kind of order 0. The impact parameter a is of the order of the planet's radius, which is greater than the atmosphere's scale height H. One gets $a/H >> 1$. In this limit, the Bessel function becomes:

$$K_0\left(\frac{a}{H}\right) \rightarrow \sqrt{\frac{\pi H}{2a}} exp\left(\frac{-a}{H}\right) \tag{2.70}$$

and the relation (2.69) becomes:

$$\alpha(a) = \mu(r)\sqrt{\frac{2\pi a}{H}} \tag{2.71}$$

This last relation shows that if the refractivity increases with a decreasing altitude, then the bending angle increases as well with decreasing altitude[35]. By combining the approximation made in (2.64) with the relation (2.71), one can get another expression for the approximation of the frequency residuals as:

$$\Delta f(a) \simeq \frac{f\mu(r)V}{c}\sqrt{\frac{2\pi a}{H}} \tag{2.72}$$

Since the vertical extend of the Martian atmosphere and ionosphere are much smaller than the radius of Mars, one can approximate that $R_{Mars} \simeq a$ and use this in the relation (2.72). By doing so and by reverting the relation, the uncertainty on the refractivity σ_μ can be expressed as[18][35]:

$$\sigma_\mu \simeq \frac{c\sigma_{\Delta f}}{Vf}\sqrt{\frac{H}{2\pi R_{Mars}}} \tag{2.73}$$

This approximation it perfectly acceptable as the uncertainty on the refractivity is small, so it can be approximated to a small bending angle, which respects the condition of the relation (2.64)[34][35]. When combining the relations (2.57) and (2.73), one can approximate the uncertainty on the electron density as[35]:

$$\sigma_{N_e} \simeq \frac{4\pi\sigma_{\Delta f} f c m_e \epsilon_0}{Ve^2}\sqrt{\frac{2\pi H_{iono}}{R}} \tag{2.74}$$

where H_{iono} is the scale height of the Martian ionospheric plasma. In the same way, by combining the equations (2.58) and (2.73), one can express an approximation for the uncertainty on the neutral number density as[35]:

$$\sigma_{N_n} \simeq \frac{c\sigma_{\Delta f}}{Vf\kappa}\sqrt{\frac{H_n}{2\pi R}} \tag{2.75}$$

where H_n is the scale height of the neutral atmosphere. However, these relations cannot be used to derive the whole vertical profiles of the electron density or of the neutral density, as the approximation of small bending angles is not satisfied for the whole radio occultation measurement. The uncertainties are only weakly dependent on the altitude, allowing to consider that these would approximate to small bending angles and thus to use the relation (2.64)[34][35].

By using the uncertainty on the neutral number density, one can then compute the uncertainty on the pressure with the equation (2.62). With the latter and the relation (2.75), one can also compute the uncertainty on the temperature by using the ideal gas law written at (2.61). These relations also depend on the gravitational field and on the altitude which also introduce uncertainties. The uncertainty on the altitude depends on the precision of the ray path geometry, which is usually assumed to be less than 100 meters since the reconstruction of MEX orbit is accurate[19]. The uncertainty on the gravitational field can be directly derived from the expression $g = (GM_{Mars})/r^2$, where G is the gravitational constant, M_{Mars} is the mass of Mars and r the distance to the center of the planet, while using the uncertainty on the r. The uncertainty on the temperature and on the pressure both increase with increasing altitude (cf. Figure 11). The uncertainty on the temperature is low at the surface with values $< 1\%$ of the temperature but grows rapidly to a few tenths of Kelvin over 40 km of altitude until the boundary with the ionosphere (cf. Figure 11, bottom).

2.3 Numerical Method and Stability

This subsection first describes the different methods used to compute numerically the Abel transform in the relation (2.54) as it is one of the main computation needed to retrieve the different quantities of interest, such as the densities, the pressure or the temperature. This is followed by an explanation of the concept of baseline corrections that are used on the electron density profiles and how some parameters are introduced to manually fit these profiles. An analysis of the stability of the baseline corrections' parameters and of the uncertainties they add to the processed data is

conducted. Finally, a comparison between our processed data and the same data processed externally is made to confirm that our method for the treatment of the radio occultation data is valid. The external results used here are already published and validated by the scientific community.

2.3.1 Numerical Integration of the Abel Transform

The use of a numerical method for the data reduction implies to use discrete steps to compute the bending angle α_i and the impact parameter a_i. The data samples are annotated with an index i that ranges from 1 to N. These are arranged in order of increasing impact parameters, thus of increasing altitude. The Abel transform can be evaluated by connecting adjacent samples with straight lines. For successive samples with impact parameters such as $a_i < a < a_{i+1}$, one can express the bending angle as [32]:

$$\alpha = C_i a + D_i \tag{2.76}$$

where C_i and D_i are constants expressed as:

$$C_i = \frac{\alpha_{i+1} - \alpha_i}{a_{i+1} - a_i} \tag{2.77}$$

$$D_i = \frac{\alpha_i a_{i+1} - \alpha_{i+1} a_i}{a_{i+1} - a_i} \tag{2.78}$$

By replacing α by its expression given by the relation (2.76) in (2.54), one gets a new expression for the refractive index as:

$$ln(n_j) \simeq \frac{1}{\pi} \sum_{i=j}^{N-1} \int_{a_i}^{a_{i+1}} \frac{C_i a + D_i}{(a^2 - a_j^2)^{1/2}} da \tag{2.79}$$

One can consider the functions depending on the impact parameter $F_j(a)$ and $G_j(a)$:

$$F_j(a) = \int \frac{da}{(a^2 - a_j^2)^{1/2}} \tag{2.80}$$

$$G_j(a) = \int \frac{a}{(a^2 - a_j^2)^{1/2}} da \tag{2.81}$$

These functions can be evaluated analytically as[32]:

$$F_j(a) = ln \left(\frac{a}{a_j} + \left[\left(\frac{a}{a_j} \right)^2 - 1 \right]^{1/2} \right) \tag{2.82}$$

$$G_j(a) = \sqrt{a^2 - a_j^2} \tag{2.83}$$

which can be verified through differentiation. By combining the relation (2.79), (2.82) and (2.83), one gets that:

$$\ln(n_j) \simeq \frac{1}{\pi} \sum_{i=j}^{N-1} \{C_i \left[G_j(a_i + 1) - G_j(a_i)\right] + D_i \left[F_j(a_{i+1}) - F_j(a_i)\right]\} \tag{2.84}$$

This last expression allows to express the refractive index of the j^{th} layer of the probed atmosphere. Considering a data sample of N measurements is equivalent to approximate the atmosphere as stratified. The accuracy of the profile of the atmosphere increases as the number of data samples N increases. However, since this is the basis of our numerical approach, the time needed to treat one radio occultation measurement also increases with N.

2.3.2 Baseline Fits and Manual-fits

As already expressed in the Section 2.2.2, a baseline fit is performed on the radio occultation measurements. However, systematic errors on the electron and neutral densities are a common phenomenon with this measurement technique.

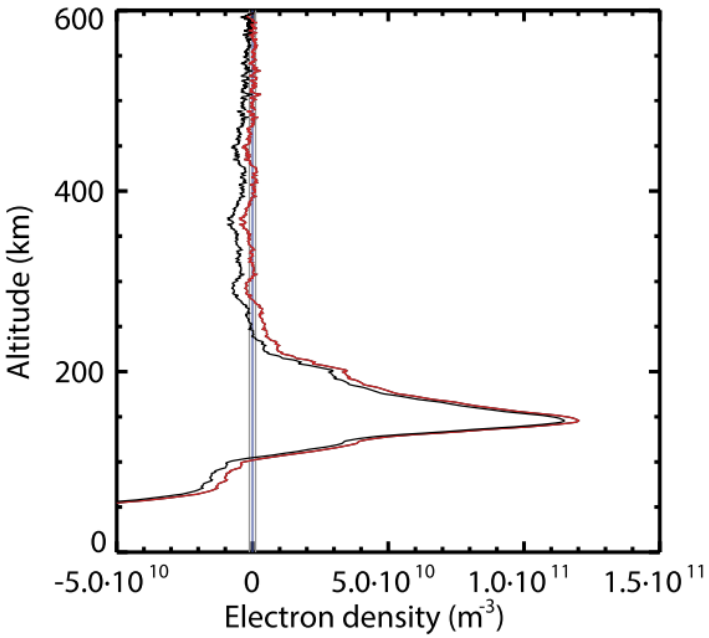

Figure 12: Comparison between two versions of an electron density profile derived from the same radio occultation. The black line is a version of the profile without any correction. The red line is a version of the profile with a fitted baseline correction. The straight blue line represents the zero value of the electron density and the two grey ones are the usual noises coming from the thermal and phase noises explained above[20].

Under ideal conditions, a ray path passing through a medium with negligible refractivity, the frequency residuals measured for that ray path should be zero[19][20]. In reality and as introduced in the previous subsection, some experimental errors are systematically introduced due to the thermal noise of the equipments or due to the phase noise caused by the interplanetary plasma. These noises are randomly distributed and cause the frequency residuals measured to fluctuate a little around zero. These type of errors are no obstacle to the elaboration of accurate frequency residuals profiles[18][19].

Other factors, such as errors in the trajectory reconstructions or oscillator drift in the radio equipment can also introduce drift in the measured frequency residuals[20]. This type of errors are not corrected automatically by the fitted baseline correction and can lead to unreliable profiles if these biases are not removed.

The Figure 12 shows two versions of an electron density profile retrieved from the same radio occultation. The black line is a version of the profile where no baseline correction was performed whereas the red line is a version where only a fitted baseline correction was used. One clearly sees that the black profile does not exhibit an electron density equal to zero at high altitudes nor at the transition region between the ionosphere and the neutral atmosphere, which are two characteristics of an accurate electron density profile (cf. Section 2.2.3 and 2.2.4)[20][26]. As at high altitudes, the electron density depends on the residual frequency value, this means that the residual frequency is also not zero. The red profile exhibits an electron density, and thus a residual frequency, equals to zero at high altitudes as a fitted baseline correction was applied. However, the transition region between the ionosphere and the neutral atmosphere is not exhibiting this characteristic, meaning that the profile is not reliable[20][36].

In order to correct such offsets in the measurement, one can proceed with the following approach. A low-order polynomial function of time is chosen and fitted to a selected high-altitude portion of the original frequency residuals. This function is then subtracted to the complete frequency residuals measurements to obtain a complete time series of the corrected frequency residuals. After this step, the high altitudes frequency residuals are now centred on zero, and so are the respective values of the electron density[20]. Until this point, the approach is the same fitted baseline correction as represented in red in the Figure 12.

However, this first correction is based on the data that are not yet influenced by ionospheric effects and so refers to the ionopause. The number of data acquired above the ionopause depends on the trajectory during the radio occultation and the ionopause position itself is always moving, as it is depending on the solar activity[20]. This makes it difficult to create a systematic correction, stressing the need to introduce an extra manual correction. A rapid look at the observed frequency residuals allows to choose the right order of the polynomial function introduced, which is linear in most of the case[20][36]. As shown by the red line of the Figure 12, even with the right choice of the polynomial function, the electron density can still be different from zero at the transition region, even if it should be. Since at this altitude the ionospheric and atmospheric effects are important, the frequency residuals are not null and cannot be used to correct the profile automatically. However, the electron density has to be zero at this altitude. One can therefore use the electron density profile from the first baseline correction to perform the extra manual fit by fine-tuning the parameters of

the polynomial function of time. To summarize this method, one can use the data points above the ionospheric layer to perform an initial baseline fit on the frequency residuals. The electron density profile is then inspected and if needed, the parameters of the baseline fit are modified to set both the high altitudes and the transition region electron densities to zero[18][20][26].

The Figure 13 shows a comparison between two versions of an electron density profile from the same radio occultation. The red line is a version of the profile on which only a fitted baseline correction based on the data points acquired over the ionospheric layer is applied. For this profile, as in the Figure 12, the baseline correction sets the electron density to zero at high altitudes but not at the transition region. The black line is a version of the profile on which a first fitted baseline correction was performed followed by a manual adjustment of the baseline parameters based on the electron density profile. This profile exhibits a zero electron density at both high altitudes and at the transition region, making it a reliable profile[20][36].

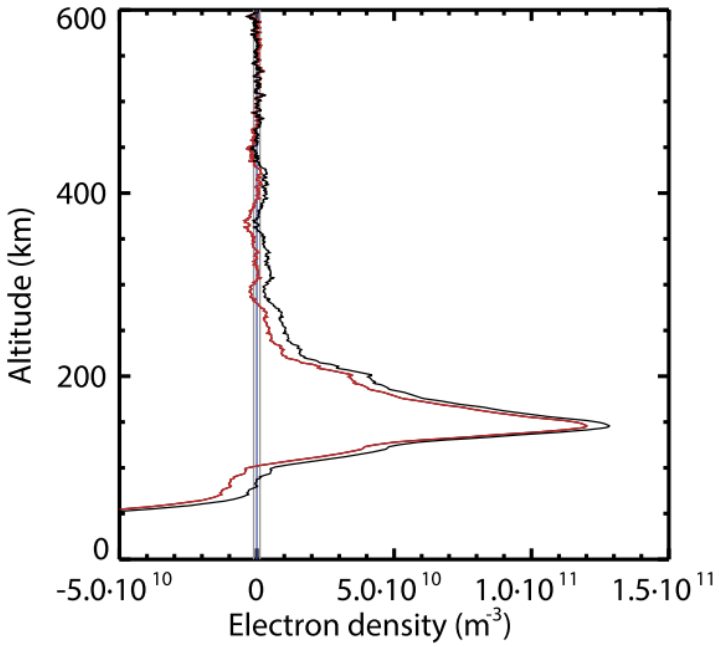

Figure 13: Comparison between two versions of an electron density profile derived from the same radio occultation. The red line is a version of the profile with only a fitted baseline correction based on the data points showing no ionospheric effect. The black line is a version of the profile on which a first fitted baseline correction was performed followed by a manual adjustment of the baseline parameters based on the electron density profile. The straight blue line represents the zero value of the electron density and the two grey ones are the usual noise coming from the thermal and phase noises explained above[20].

The frequency residuals corrected Δf_{corr} are thus equal to the difference between the frequency residuals observed Δf_{obs} and the baseline fit Δf_{fit} (2.85). In this study, all the profiles are fitted with linear functions of time Δf_{fit} (2.86)[20].

$$\Delta f_{corr} = \Delta f_{obs} - \Delta f_{fit} \tag{2.85}$$

$$\Delta f_{fit} = a_0 + a_1(t - t_0) \tag{2.86}$$

where a_0 $[Hz]$ and a_1 $[Hz^2]$ are the baseline parameters, t is the time and t_0 is the time of the highest altitude data point[20][36].

2.3.3 Stability of the Baseline Parameters

As a manual fit is made on the baseline parameters, the final profiles retrieved from the data depend on the user ability to correctly fit the parameters. Since this choice is depending on a human judgement, this can induce some differences on the baseline parameters for the same set of data, and thus can influence the outputs. This creates some additional errors on the profiles that need to be taken into account.

In order to evaluate the parameters stability and their effects on the vertical profiles, this study uses 9 radio occultations measurements from MEX MaRS, which are listed in Table 2. For each radio occultation, the profile is fitted manually using the method described in the previous subsection with a set of baseline parameters $(a_0; a_1)$ in order to retrieve reliable vertical profiles. For the same occultation, the baseline fit is done again but this time using either the set of baseline parameters $(a_0 + \Delta a_0; a_1)$ or $(a_0; a_1 + \Delta a_1)$. This last baseline fit gives other vertical profiles that are compared to the ones retrieved with $(a_0; a_1)$ which allows to evaluate the stability of each parameter. The deviation of the parameters Δa_0 and Δa_1 are chosen in order to have vertical profiles that are clearly different from the ones retrieved with the original parameters set but that could also be seen as reliable from the user perspective (Figure 14 and 15). For this study, the values used for Δa_0 and Δa_1 in this stability analysis are respectively $1.0{\cdot}10^{-6} Hz$ and $2.0{\cdot}10^{-4} Hz^2$.

Data File ID of the MEX MaRS Radio Occultation	Start Date of the Measurement (yyyy-mm-dd)	End Date of the Measurement (yyyy-mm-dd)
MEXMRS_0046_2004_139 V1.0	2004-05-18	2004-05-18
MEXMRS_0097_2004_181 V1.0	2004-06-29	2004-06-29
MEXMRS_0235_2004_355 V1.0	2004-12-20	2004-12-20
MEXMRS_0245_2004_362 V1.0	2004-12-27	2004-12-28
MEXMRS_0570_2005_268 V1.0	2005-09-25	2005-09-25
MEXMRS_0895_2006_084 V1.0	2006-03-25	2006-03-25
MEXMRS_1164_2007_118 V1.0	2007-04-28	2007-04-28
MEXMRS_1119_2007_134 V1.0	2007-05-14	2007-05-14

Table 2: Table listing the data files ID of MEX MaRS radio occultations used in the stability analysis of the baseline fit parameters. The starting and ending dates of each radio occultation are also provided.

Figures 14.a and 14.b show an example of the different vertical profiles retrieved through the MEXMRS-0046-2004-139 data measurement of 2004, DOY 139. The green lines represent the vertical profiles while using the original manually fitted parameters (a_0, a_1) and the red lines represent the profiles with the parameter set $(a_0 + \Delta a_0, a_1)$. The Figures 15.a and 15.b show the same comparison for the same radio occultation but where the red profiles include a deviation on the other parameter such as $(a_0, a_1 + \Delta a_1)$. The comparison of the profiles in both the Figures 14 and 15 shows that both parameters are stable and that a small deviation of these parameters does not lead to completely different profiles. The same results are found when comparing the profiles from the 8 remaining radio occultations from the Table 2.

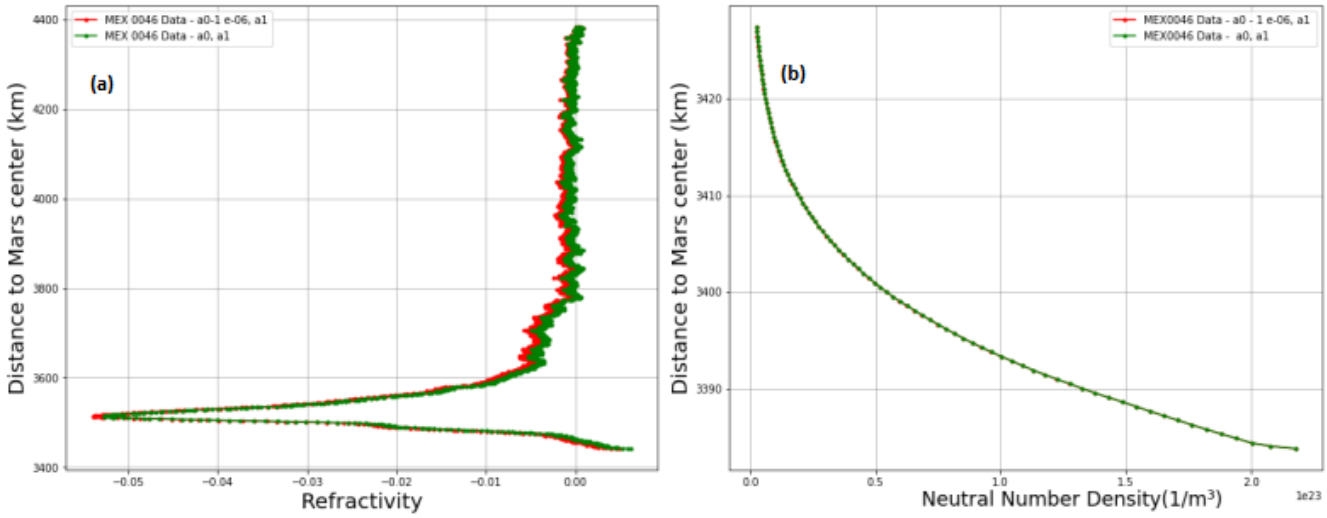

Figure 14: Comparison of the differences induced by a deviation of $1.0 \cdot 10^{-6} Hz$ on the parameter a_0 in a vertical refractivity profile (a) and in a vertical neutral number density profile (b). The radio occultation measurement used in the above profiles corresponds to the MEX MaRS measurement 2004/DOY139.

In order to quantify the errors generated by the small deviations on the baseline parameters, the refractivity and neutral number density's differences of the red and green profiles are computed for each radio occultation[36]. The mean and the standard deviation of the differences are then taken for each radio occultation. The error caused on the refractivity (neutral number density) by the small deviations introduced on the baseline parameter a_0 is then set to be equal to the mean of the means of the differences of refractivity (neutral number density) over all the profiles in which a_0 was perturbed. The same error estimation is applied for the a_1 parameter. For the refractivity, the errors caused by a perturbation on respectively a_0 and a_1 are σ_{μ,a_0} and σ_{μ,a_1}. From this analysis, the total error on the refractivity caused by this manual baseline fit is set to be $\sigma_{\mu,baseline} = \sqrt{\sigma^2_{\mu,a_0} + \sigma^2_{\mu,a_1}} = 0.03\sigma_\mu$. This means that the error on the refractivity caused by the manual baseline fit is very small. The error caused by the manual baseline fit on the density can be computed in a similar way, giving $\sigma_{Nn,baseline} = \sqrt{\sigma^2_{Nn,a_0} + \sigma^2_{Nn,a_1}} = 0.02\sigma_{Nn}$. The error on the neutral number density caused by the manual baseline fit is small as well. One can thus conclude that the baseline parameters are stable and that small variations of these parameters do

not really change the vertical profiles that are analysed here. However, even if small, these errors are included in the total error computations in all the following results.

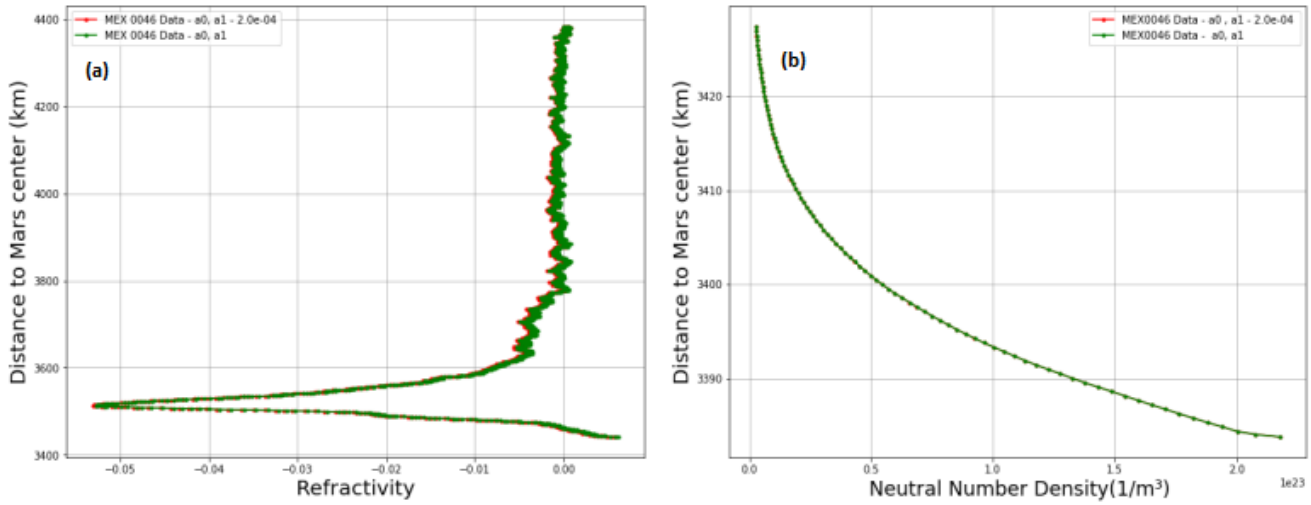

Figure 15: Comparison of the differences induced by a deviation of $2.0 \cdot 10^{-4} Hz$ on the parameter a_1 in a vertical refractivity profile (a) and in a vertical neutral number density profile (b). The radio occultation measurement used in the above profiles corresponds to the MEX MaRS measurement 2004/DOY139.

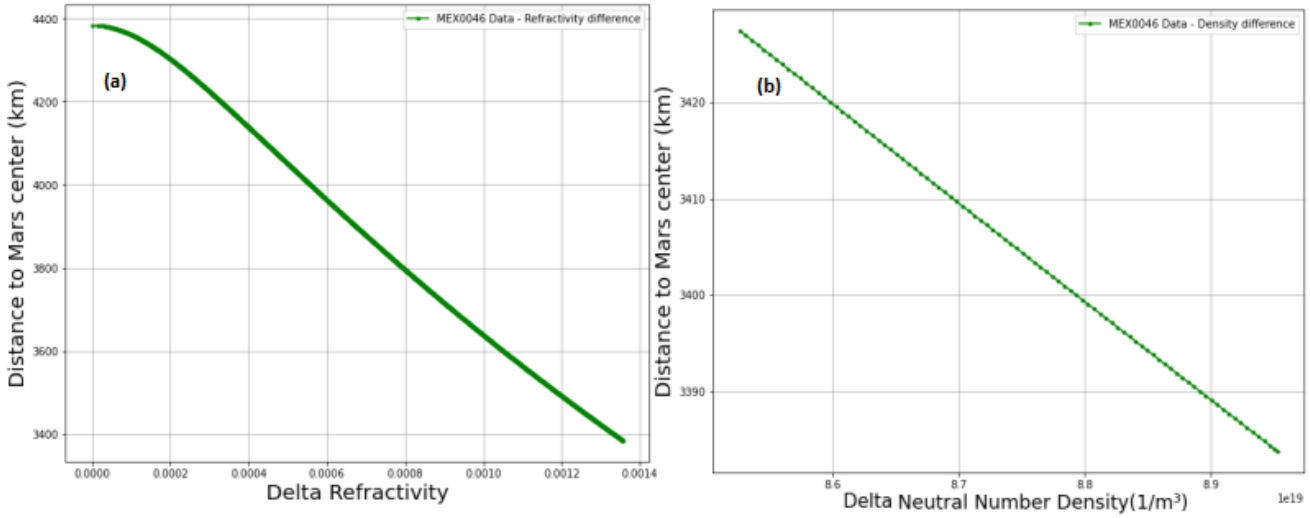

Figure 16: Differences of the vertical refractivity profiles plotted in Figure 14.a (a) and of the neutral number density profiles plotted in Figure 14.b (b).

The Figures 16.a-b and 17.a-b show the respective vertical profiles of the differences of refrac-

tivity and of neutral number density between the green and red profiles in the Figures 14.a-b and 15.a-b. By comparing the scales of the Figures 14 and 15 to the ones of the Figure 16 and 17, it is clear that the differences induced by the deviations of the baseline parameters remain small and that the manual baseline fit method does not cause large errors. These differences increase with decreasing altitude but as the values of both the refractivity and the neutral number density increase as well, those differences remain nearly negligible.

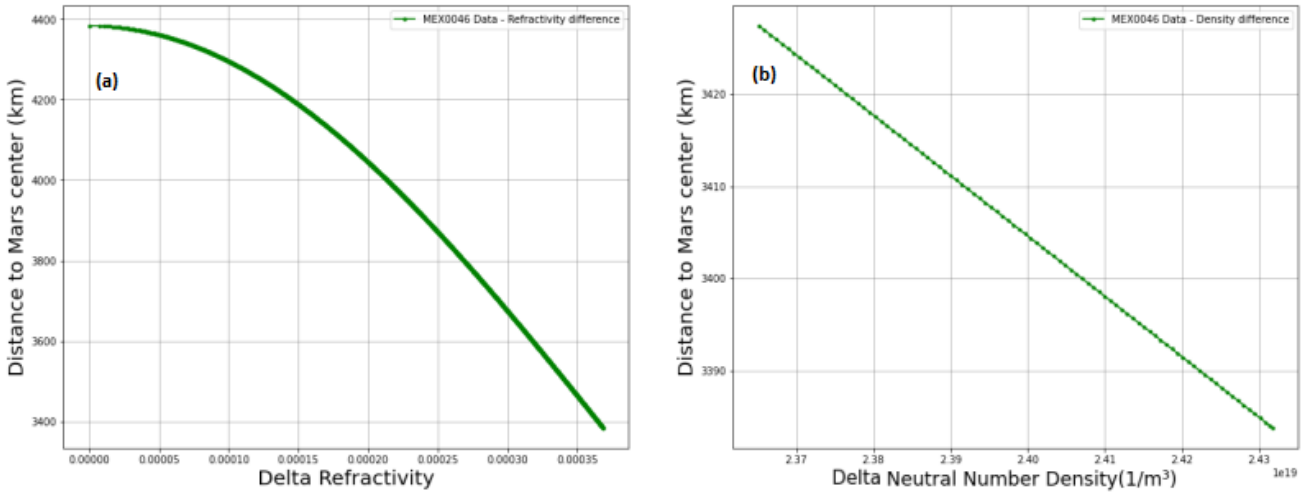

Figure 17: Difference of the refractivity vertical profiles plotted in Figure 15.a (a) and of the neutral number density profiles plotted in Figure 15.b (b).

2.3.4 Comparison of Vertical Profiles with an External Study

In order to validate the numerical method used for the data treatment in this study, the profiles retrieved from the nine radio occultations of the Table 2 are here compared to the profiles of an external study from the University of Cologne retrieved from the same radio occultations[18][19]. The external results were provided by the Royal Observatory of Belgium from a previous collaboration with the University of Cologne.

The Figure 18 shows a comparison between the refractivity profile obtained in this study from the data file MEXMRS-0097-2004-181 V1.0 (blue line) and the one from the University of Cologne for the same file (yellow line). As the external refractivity profile only includes data from the ionosphere, this comparison is only limited to this region. This is not a problem as it is the region of interest for the manual baseline fit described in section 2.3.3. One can clearly see that, after using a manual baseline correction as described above for a data file, the refractivity profile matches nearly perfectly to the one of the University of Cologne. The red line in the Figure 18 represents the difference of refractivity as a function of the distance to the center of Mars. Over the whole vertical profile, this refractivity difference is small compared to the actual value of the refractivity. The mean value of the refractivity over the vertical profile from this study is $\mu_{mean,iono} = -0.061$ whereas the mean value of the difference of refractivity is

$\Delta\mu_{mean,iono} = -0.0032$, or only about $\sim 0.05\mu_{mean,iono}$. Additionally, the maximum value of the difference of refractivity (at the peak) is $\Delta\mu_{max,iono} = -0.00094$ whereas the peak of the refractivity profile from this study is $\mu_{max,iono} = -0.0466$, which remains large compared to $\Delta\mu_{max,iono}$. This clearly shows that, in this case, the refractivity profile from this study is nearly identical to the one of the external study.

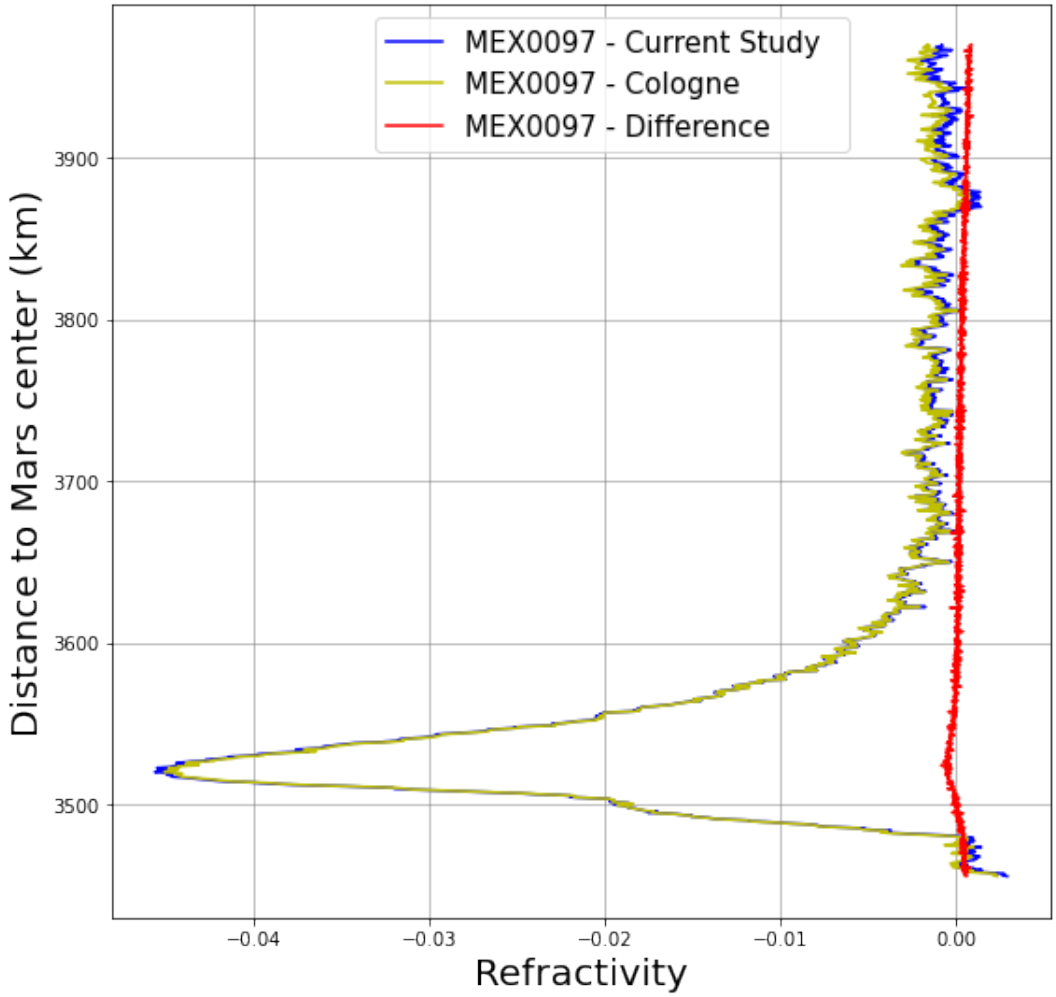

Figure 18: Comparison of the refractivity between the vertical profile of this study (blue) and the one from the University of Cologne (yellow). Both profiles were computed using the data file MEXMRS-0097-2004-181 V1.0 from MEX MaRS. The difference of refractivity as a function of the distance to the center of Mars is plotted in red.

As the refractivity profiles are very similar, it is obvious that both the electron and the neutral number densities profiles will also be very close, as these densities are directly proportional to the refractivity (cf. Section 2.2.4). The Figure 19 shows the comparison between the neutral number density profile of this study and the one of the external study, both still originating from the same

data file MEXMRS-0097-2004-181 V1.0. Here again, as showed in the Figure 19.a the profiles are very similar. The Figure 19.b shows the neutral number density difference between the profiles as a function of the distance to the center of Mars. The mean value of the neutral number density difference $\Delta N_{n,mean}$ is equal to $\sim 0.5\%$ of the mean value of the neutral number density profile from this study ($N_{n,mean} = 4.87 \cdot 10^{22} m^{-3}$). Even if the difference increases with decreasing altitude, it increases at a slower rate than the actual number density. The greatest ratio between the number density difference and the actual value of the neutral number density is actually located at the highest altitude of the neutral atmosphere, where $\Delta N_n \simeq 0.05 N_n$ which is still very small. The differences are negligible, therefore, the neutral number density profile from this study, acquired using the above method, clearly replicates the one of the external study with great accuracy.

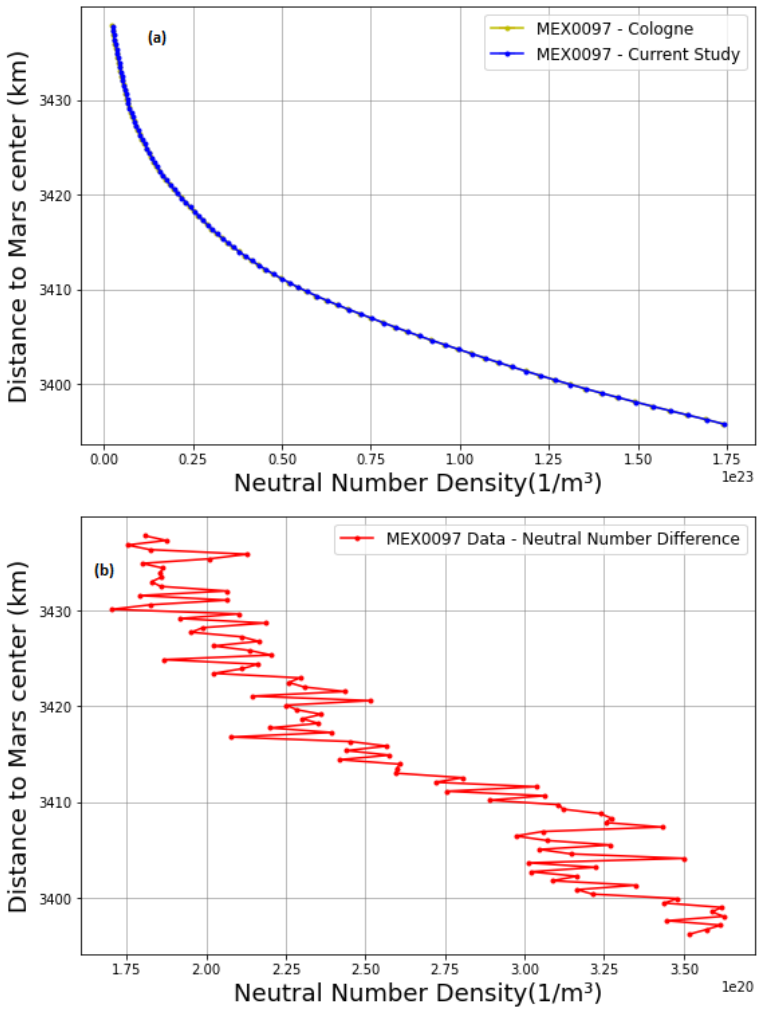

Figure 19: (a) Comparison of the neutral number density between the vertical profile of this study (blue) and the one from the University of Cologne (yellow). Both profiles were computed using the data file MEXMRS-0097-2004-181 V1.0 from MEX MaRS. (b) The difference of neutral number density as a function of the distance to the center of Mars is plotted in red.

The temperature profiles are the most sensitive to the initial conditions and to the integration method used, as they depend on more variables (gravitational field, density, pressure). Moreover, the temperature is a key parameter in this thesis as one of the main hypothesis of this work is that the electrons from SEP events or CME can trigger an extra-ionization of the upper neutral atmosphere which should generate an increase of the temperature at these altitudes [7][8][25]. It is thus very important that the method used here to compute the temperature profiles must be accurate and capable of replicating some previously validated results.

In this optic, the same comparison is made between our temperature profiles and the ones from the external study. In this case and as showed in the Figure 20 (top), three vertical temperature profiles are plotted for each study, coming from the same data file. For each study, the three temperature profiles correspond to three different initial conditions for the temperature at a certain altitude of the neutral atmosphere, which is needed to initiate the integration. This temperature T_0 is set at 3436 km (50 km above the mean radius of Mars) and is equalled to 130 K (blue), 165 K (green) and 200 K (red) in both studies[18][19]. This allows to cover the whole plausible range of values of the temperature at this altitude, based on in-situ measurements and models. It is worth noting that the choice of this initial value has here a great influence on the rest of the profile, especially as the altitude increases. However, the choice of setting the initial condition on the temperature at 50 km altitude is not usual and was made by the University of Cologne. This study only does it with the intention of replicating the same conditions in order to compare and validate the outputs of the numerical method. In the Section 3, the initial condition on the temperature is set at 80 km altitude which is just at the top of the neutral atmosphere and which is the most relevant choice for an integration over the whole atmosphere.

In the Figure 20 (top), the temperature profiles from this study are plotted in solid lines and the ones from the external study are plotted in dashed lines. It is clear that there exists only a small difference between the temperature profiles using the same initial conditions. The Figure 20 (bottom) also shows the vertical profile of the difference between the temperature profiles of this study and the ones of the external study. The color code remains the same as in the top panel of the same figure. The difference of temperature between each corresponding profiles clearly increases with the altitude, reaching values that can exceed 5 K. However, this is not a problem as this difference is clearly included in the uncertainties of the two profiles which are also increasing with the altitude, as seen on the top panel of the Figure 20. As the gap between the two temperature profiles is filled with the uncertainty margin, one can clearly state that these profiles are similar and that our numerical method is reliable. Moreover, the uncertainty on the temperature profiles of the external study might not include the additional human error caused by the manual baseline fit, that was computed previously. This could enlarge their uncertainties.

The same analysis on these three quantities was made for all the other eight data files listed in the Table 2. The comparison gives similar results and conclusions as all the profiles are nearly identical to the ones of the University of Cologne's study. This shows that by applying our numerical method and the manual baseline fit, one can retrieve nearly similar refractivity profiles as the ones coming from validated external studies. This method can thus be applied independently as well as for other purposes while acknowledging the reliability of the results, as it is done in the Section 3.

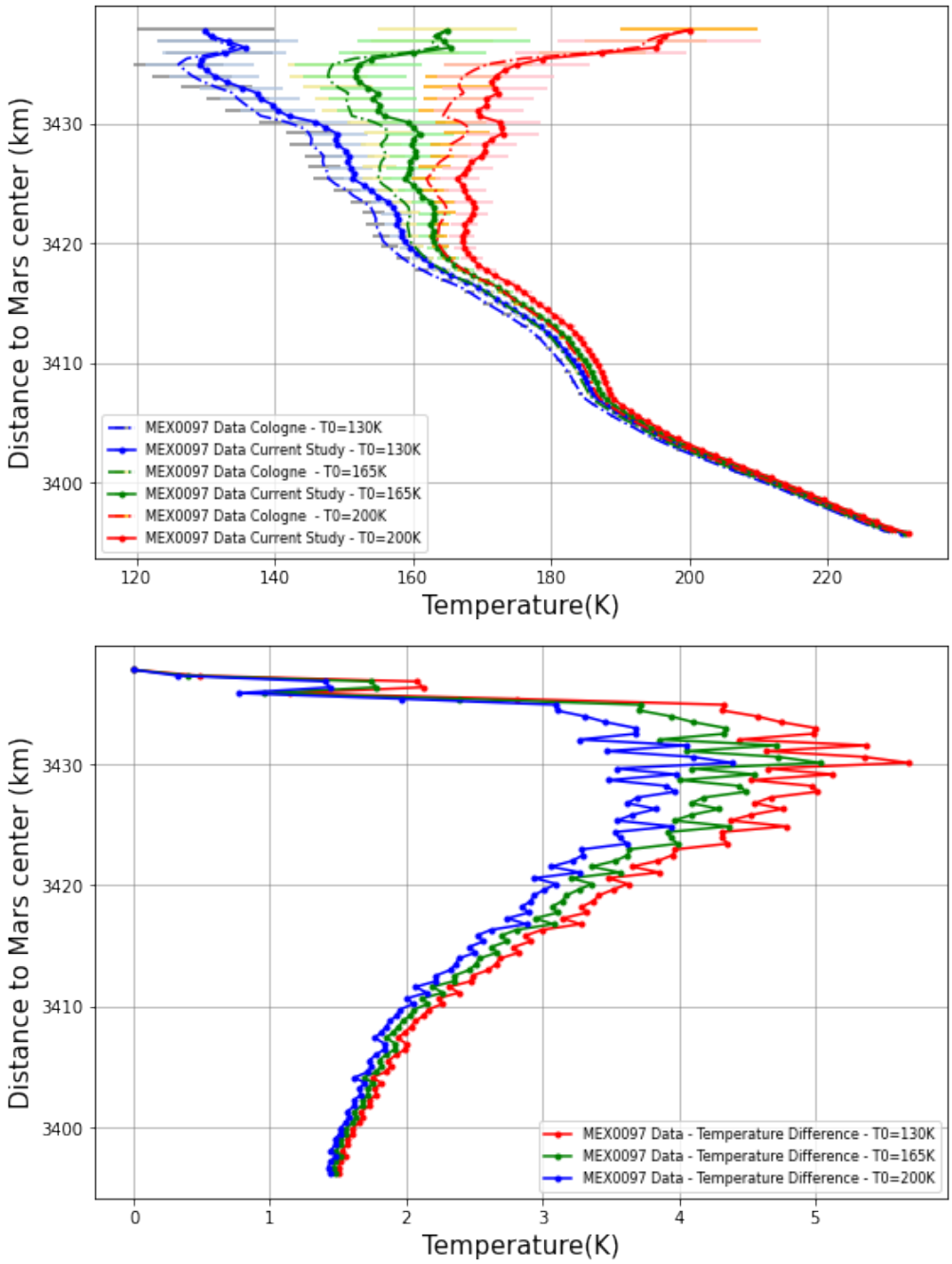

Figure 20: (Top) Comparison between the vertical temperature profiles of this study (solid line) and the ones of the external study (dashed line) from the University of Cologne. The blue, green and red lines correspond respectively to an initial temperature of 130K, 165K and 200K set at a distance of the center of Mars of 3436 km. All profiles were computed using the data file MEXMRS-0097-2004-181 V1.0 from MEX MaRS. (Bottom) The differences of temperature as a function of the distance to the center of Mars are plotted with the same color code than above.

3 Data Selections and Results

This thesis' main objective is to correlate the SEP events or CME that impacted Mars with some changes of the physical properties of the Martian neutral atmosphere using radio occultation measurements. The previous studies on radar blackouts of MARSIS and SHARAD constitute a real trigger for this research as these blackouts are caused by some SEP events or CME electrons interacting with the Martian atmosphere and causing an extra-ionization of the medium[7][8]. This extra-ionization increases the electron content along the radar signal path which attenuates greatly the signal creating a blackout (cf. Section 2.1). The radar blackouts can be used as indicators of such SEP or CME events on Mars but do not give any information on the physical properties of the Martian ionosphere and atmosphere as the signal is lost. The use of radio occultation is thus necessary as it is not influenced by such events and allows to probe the whole Martian ionosphere and atmosphere during these periods. Based on the these information, this section presents the radio occultation data selection criteria used in this study in order to analyse the impact of SEP and CME electrons on the physical properties of the Martian ionosphere/atmosphere. The data selected are divided between different periods of time and are analysed as case studies. The data are processed with the method explained extensively in the Section 2.2 and 2.3 and different vertical profiles of various quantities are then presented. This is followed by observations of the influence that the SEP and CME events have on Mars atmosphere which are correlated to both the radar blackouts and SEP electrons flux measurements.

3.1 Data Selection Using Radar Blackouts of MARSIS and SHARAD

The correlation between radar blackouts and SEP and CME events was only highlighted very recently by the study of Sanchez-Cano et al. 2019 on a single event in September 2017, and later on by the study of Lester et al. 2022 on the impact of energetic solar particles on the Martian ionosphere during a full solar cycle [7][8]. By correlating the increases in the flux of energetic electrons of solar origin detected by MAVEN with the blackouts of the radar instruments MARSIS and SHARAD over these periods, these studies proved that SEP and CME events are at the origin of the radar blackouts. The Figure 21 shows a chronology of all the orbits performed by MEX and MRO which are carrying respectively the radar instruments MARSIS and SHARAD. Each orbit is represented by a grey line except the orbits for which blackouts or partial blackouts were observed, which are respectively represented by red and blue lines. There are two columns representing each one, one of the radar instruments and each row is representing a year [8].

As this study aims to analyse the effects of SEP and CME events on the atmospheric physical properties by using radio occultation measurements, the radar blackouts represent great indicators of such periods in order to select the radio occultation data used in this work. A first feature to notice in the Figure 21 is that the MARSIS instrument is more sensitive and that it experienced more blackouts than the SHARAD instrument. The reason behind this is that MARSIS uses a lower carrier frequency (1.8-5 MHz) than SHARAD (20 MHz) [8]. Since the attenuation of the signal is inversely proportional to the square of the carrier frequency (see equation (2.1)), a higher frequency signal experiences less attenuation. This also explains why radio occultation is not affected at all by these events since it operates at much higher frequencies of the order of the GHz [2][7][8].

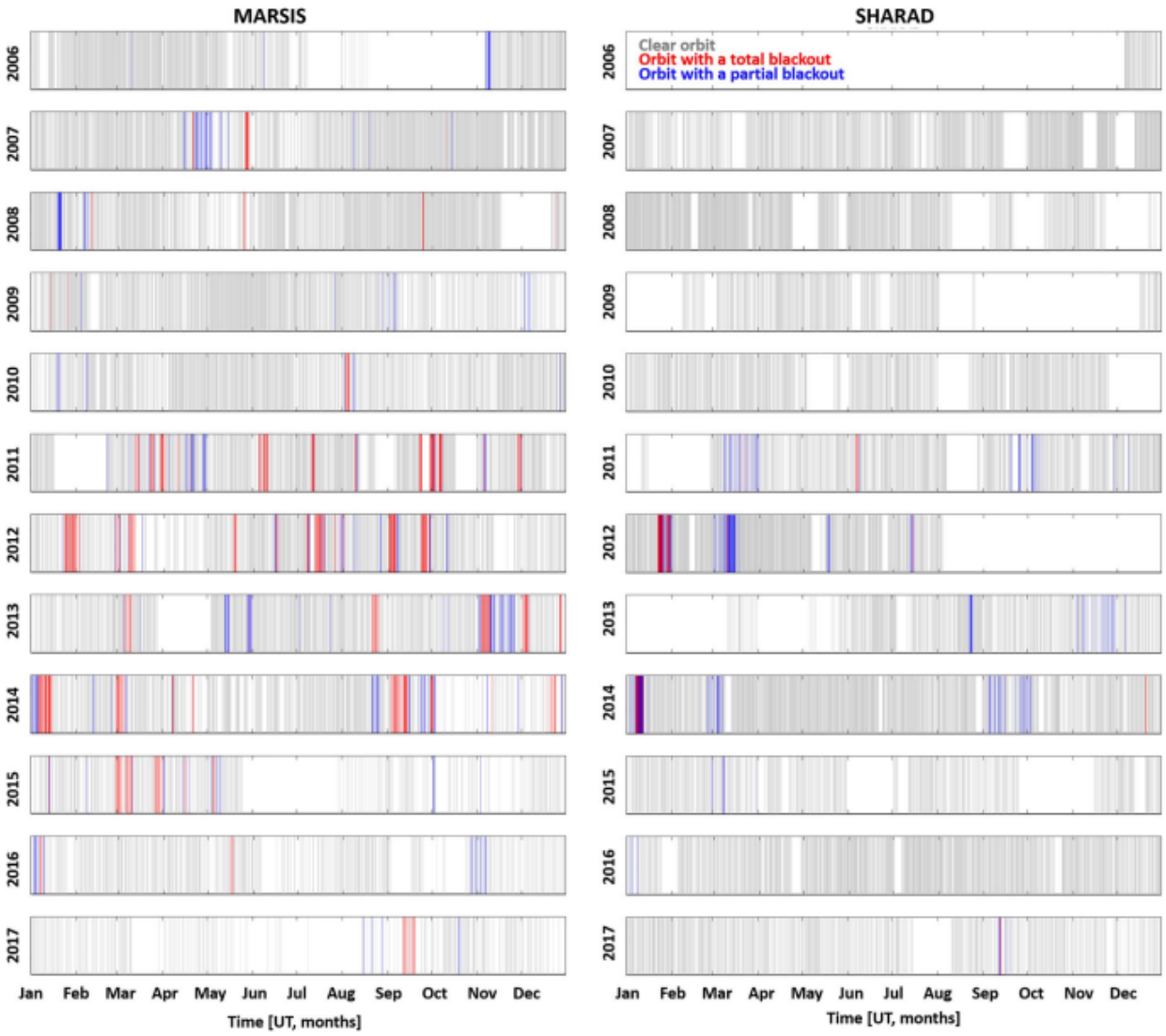

Figure 21: The orbits where the radar is operating are represented by grey vertical lines, where a total blackout occurs by red vertical lines and where a partial blackout occurs by blue vertical lines. The left hand panels are for MARSIS and the right hand ones for SHARAD. Each row represents one calendar year starting from 2006 at the top [8].

In order to select the periods of interest for this study, the first criteria was that the events would be strong enough to induce noticeable changes in the physical properties of the ionosphere and of the upper atmosphere of Mars. In this optic, only periods where both radars experienced blackouts simultaneously are considered, since these would be associated with the strongest SEP and CME events impacting Mars. The second criteria was the availability of MEX radio occultation data during these periods. MEX MaRS is only one of the many instruments of MEX and it is not operating continuously. Moreover, in order to perform radio occultations of Mars, the Earth and the spacecraft need a particular geometrical configuration, as mentioned in the Section 2.2, which

is not always the case. Finally, the existence of previous studies of these particular SEP or CME events on Mars were also accounted in order to have detailed knowledge of the chronology and of the properties of these events, especially using particles counters measurements and spectrometers. Even if nearly all the strong SEP and CME events have been studied, some received more scientific attention than others.

Knowing these criteria and constraints, the periods that are analysed in this study are the CME of June 2011 and the SEP events of February and March 2015. The two periods are hereunder studied as two case studies.

3.2 Case Study 1 - CME Impact on Mars during June 2011

3.2.1 Chronology and Properties of the Event through Various Measurements

On the 5^{th} of June 2011, a powerful CME impacted Mars' environment, disturbing the ionospheric and atmospheric structures for multiple days, until the 11^{th} of June. The peak of this disturbance happened on the 6^{th} of June [37]. This long-lasting disturbance was clearly observed by MARSIS as multiple blackouts were experienced by the radar between the 5^{th} and the 11^{th} of June.

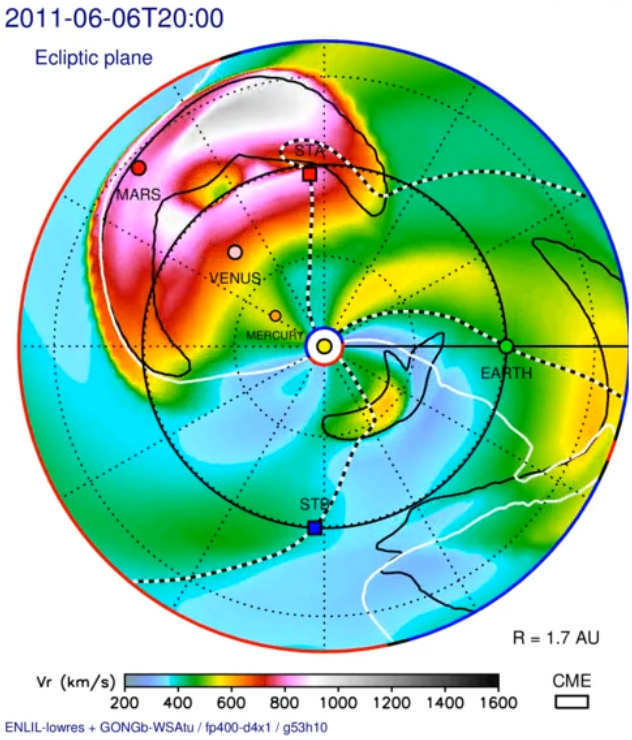

Figure 22: Helioweather results for the space weather on the 6^{th} of June 2011, showing a large CME impacting Mars [38].

The Figure 22 shows the Helioweather website's results for the space weather on the 6^{th} of June

2011 at 20:00 UT. These are retrieved from an experimental, real-time simulation of corotating and transient solar wind disturbances driven by various coronal models. It is obvious that at this period, a large CME impacted Mars with fast solar winds having a radial velocity of ∼1000 km/s [38].

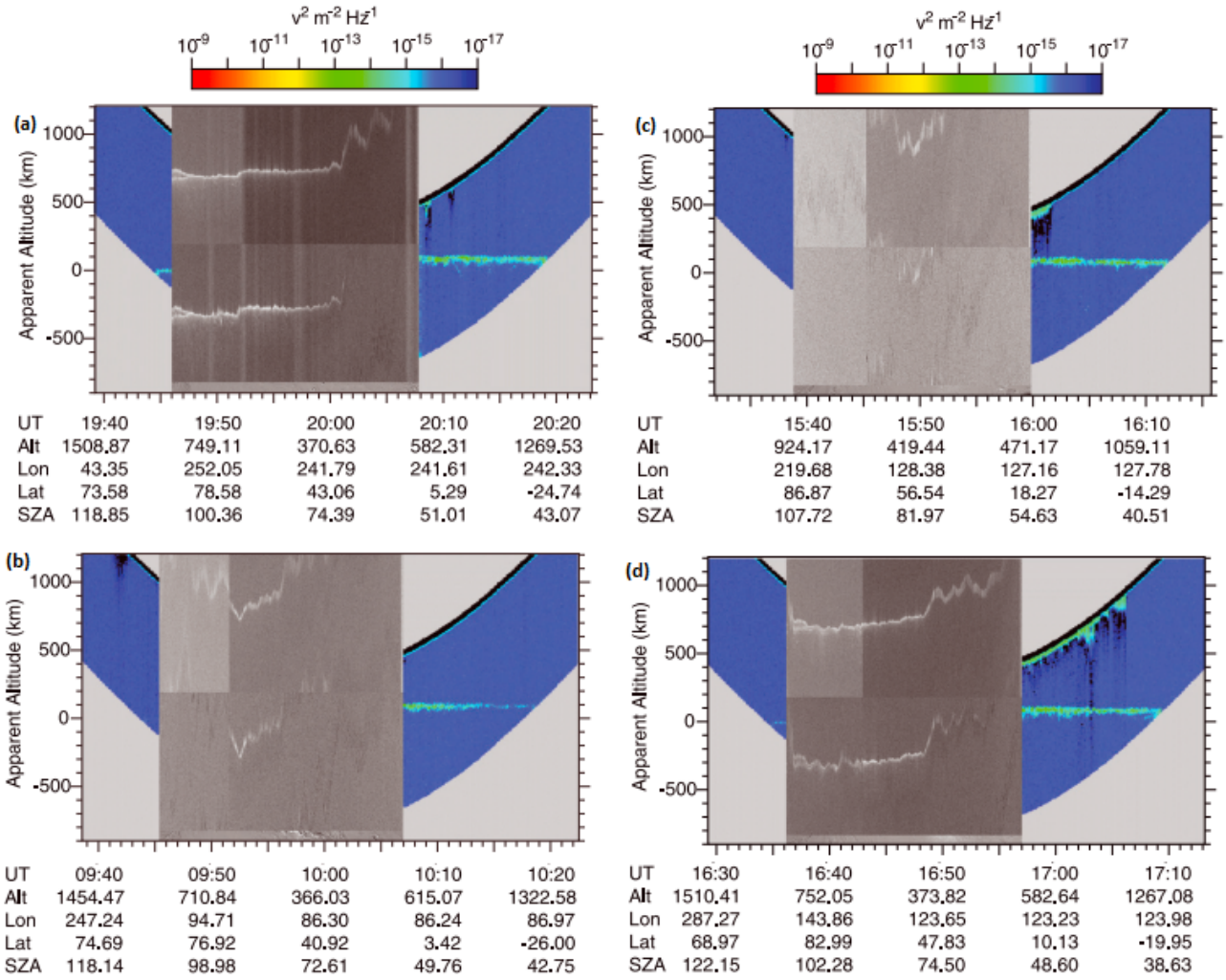

Figure 23: MARSIS subsurface radar signals in two frequency bands surrounded (grey blocks) by ionospheric mode echograms before and during the impact of the CME on Mars. The radargrams a, b, c and d were respectively taken on the 4^{th}, 5^{th}, 11^{th} and 12^{th} of June 2011 [37]. See the text for further explanations.

Four of the radargrams provided by MARSIS during this period are presented in the Figure 23. The color bar and colored region are data from MARSIS AIS mode (sounding the ionosphere); the grey scale blocks of data are two frequency bands of MARSIS subsurface data. The universal time, the spacecraft's altitude, the latitude and longitude as well as the SZA are provided below each radargram. The Figure 23.a shows the radargram taken on the 4^{th} of June 2011, just before

the impact of the CME. One can see the surface reflection (small green signal on the left of the bottom grey block) just a couple of minutes before the onset of the subsurface reflection. After the acquisition of the subsurface data, around 20:08 UT, the ionospheric reflection becomes visible. The Figure 23.b shows the radargram taken on the 5^{th} of June, still before the shock, but in the region where SEPs are starting to increase. The ionosphere and atmosphere are starting to be disturbed and the first effects of this disturbance become visible [37]. The surface reflection of the AIS mode is not visible anymore as the subsurface reflection becomes weaker and difficult to distinguish, which is a sign of an extra attenuation of the signal due to an increase of the electron density [7][8][37]. This evolves into a total blackout of the radar with the disappearance of the subsurface signal from the 7^{th} until the 10^{th} of June. On the 11^{th} of June, the subsurface signal begins to reappear as the ionospheric and atmospheric disturbances start to fade. This can be seen in the Figure 22.c. Finally, on the 12^{th} of June, as the CME has completely past Mars and as the SEPs have returned to a usual level, the subsurface signal is restored as shown in the Figure 22.d. However, even more than 6 days after the peak of the disturbance, the surface reflection of the AIS mode has still not returned to its value of before the impact. This means that the disturbance, even if weaker, is still ongoing [37][39].

The blackouts events described above can be directly correlated with the measurement of the SEPs by the ASPERA-3 on board of MEX (Analyzer of Space Plasma and Energetic Atoms). This instrument is composed of an electron spectrometer and of an ion mass analyser, allowing to monitor the flux of SEPs during the CME. The High Energy Neutron Detector (HEND) on board the Mars Odyssey spacecraft can also be used for similar purposes [37]. The Figure 24.a shows the electron energy-time spectrogram during the first half of June for the electrons having a solar or ionospheric origin. A large peak of SEPs electrons is monitored on the 6^{th} of June. This disturbance fades away with time over a few days. Some smaller disturbances are observed starting from the 3^{rd} of June but seem unrelated to the CME [37]. The spike in electrons energy and flux on the 6^{th} of June is perfectly consistent with the beginning of the blackouts of MARSIS, showing a clear correlation between an increased amount of SEPs and an extra attenuation of the signal of the radar. The Figure 24.b shows the solar wind dynamic pressure derived from the measurements of the solar wind proton during the same period as in Figure 24.a. The solar wind dynamic pressure increases simultaneously with the electrons flux increase on the 6^{th} of June. The energetic particles flux becomes so high that the instrument experienced a blackout during this period, as represented by the dashed area. The instrument stayed incapacitated for about 12 hours after the main peak [37]. Here again, the increase of solar wind dynamical pressure is coherent with both the blackouts of MARSIS and the SEPs electrons increase. Finally, the Figure 24.c displays the background counts of ions detections from both ASPERA-3 and HEND. These background counts represent the detections of the energetic ions penetrating the housing of the instruments. Both instruments detected an increase in their respective background counts coinciding with the two latter peaks presented above. Additionally, the two instruments monitor different ranges of ions energies, with the HEND detected ions having energies greater of two orders magnitude than the ones detected by ASPERA-3. Since these peaks are simultaneous, this implies that the source of the increase is global which is consistent with an encompassing space weather event such as an CME [37].

All these measurements clearly correlate the detected CME that impacted Mars ionosphere with the blackouts experienced by the radar instruments. This chronology and precise information on

this CME event also allow to select efficiently the radio occultation data for the in-depth analysis of the effects of this event on the physical properties of the Martian ionosphere and atmosphere.

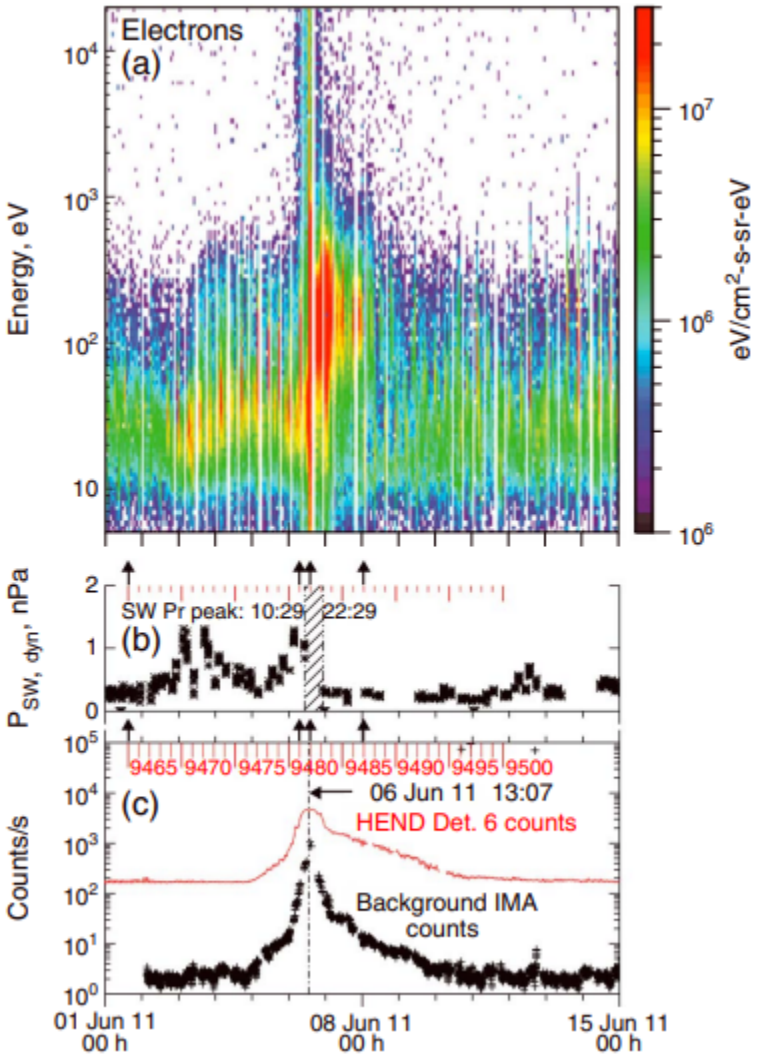

Figure 24: (a)Electron energy-time spectrogram from ASPERA-3/MEX during the CME interaction with the Martian ionosphere. The color scale indicates differential energy flux while the white vertical bands indicate no data. (b) Solar wind dynamic pressure retrieved from ASPERA-3 IMA proton measurements in the solar wind. The dashed region shows where IMA is incapacitated by the high fluxes. (c) ASPERA-3 IMA background counts (black) and Odyssey HEND charged particle counts (red). Both particle counts peak simultaneously around 13:00 UT on 6 th of June 2011 [37].

3.2.2 Radio Occultation Ionospheric Profiles during June 2011 CME Impact

In the optic of analysing the impact of these CME and SEPs events on the physical properties of Mars' ionosphere and atmosphere, the radio occultations measurements listed in Table 3 are used. These measurements took place on the 11^{th}, the 12^{th} and the 14^{th} of June 2011, when the radar disturbance started to dissipate. However, as mentioned in the above subsection, the radar signal was still disturbed by the CME impact more than 6 days after the maximum peak of SEPs. These radio occultation measurements are thus great material for this analysis.

Date	Vol ID	Longitude (Geocentric) (deg)	Latitude (Geocentric) (deg)	Local Solar Time	Ls (deg)	SZA (deg)
11/06/2011	MEXMRS_2936	290.488038	-0.731795	06:54:11 A.M.	308.916224	76.986043
11/06/2011	MEXMRS_2938	188.306296	-1.978244	06:53:09 A.M.	309.086446	76.802790
12/06/2011	MEXMRS_2939	343.974724	-4.720726	06:50:56 A.M.	309.426530	76.423617
12/06/2011	MEXMRS_2941	241.836582	-5.977834	06:49:56 A.M.	309.596459	76.257774
14/06/2011	MEXMRS_2946	348.935968	-12.681922	06:44:54 A.M.	310.614937	75.444225

Table 3: Table listing the data files ID of MEX MaRS radio occultations used in the analysis of the impact of the June 2011 CME, along with the dates of the radio occultations, the geocentric latitudes and longitudes of the measurements, the local solar times, the solar longitudes and the solar zenith angles.

As it is supposed that the CME and the associated SEPs generate an extra-ionization when interacting with Mars ionosphere which would be responsible for the radar blackouts, the first quantity that is expected to change is the electron density [7][8][25][37]. The Figure 25 presents the ionospheric vertical electron density profiles retrieved through the radio occultation measurements listed in Table 3. As this CME induces a single disturbance that dissipates through time, the radio occultation's profiles that are expected to show the most disturbances are the ones that are chronologically closer to the peak of the disturbance. One would thus expect the measurements of the 11^{th} and of the 12^{th} of June to be the most disturbed. However, the radio occultation of the 14^{th} of June is not supposed to show any disturbance as the Martian ionosphere retrieved its original structure after the 12^{th} of June, as suggested by the Figure 23 [37]. However, all ionospheric electron density profiles presented in the Figure 25 are similar, except for the orange profile which shows a slightly larger peak density but which cannot be correlated to the CME impact. There are no apparent evidence of an electron density increase caused by the CME impact. This is not very surprising since previous ionospheric sounding from MARSIS did not revealed any change in the ionospheric structure above the maximum electron density [37]. Moreover, a previous radio occultation study

of the ionosphere of Mars during this period did not show any clear evidence of an increase in the electron density due to this CME event [37][40]. This implies that the extra-ionization caused by the SEPs is occurring below the ionosphere [7][8][37][40].

The data treatment method used here allows to retrieve global vertical profiles that are encompassing the ionosphere and the neutral atmosphere from top to bottom. This allows to analyse simultaneously the boundary region between the ionosphere/neutral atmosphere and the whole neutral atmosphere. This type of radio occultation data treatment was rarely used in previous studies of Mars atmosphere, limiting their analysis to independent studies of the ionosphere or of the neutral atmosphere. This is a novelty compared to previous studies as this method was never used to analyse the influence of CME on the Martian atmosphere. The advantageous aspect of this data treatment is directly used in the atmospheric profiles analysis hereafter.

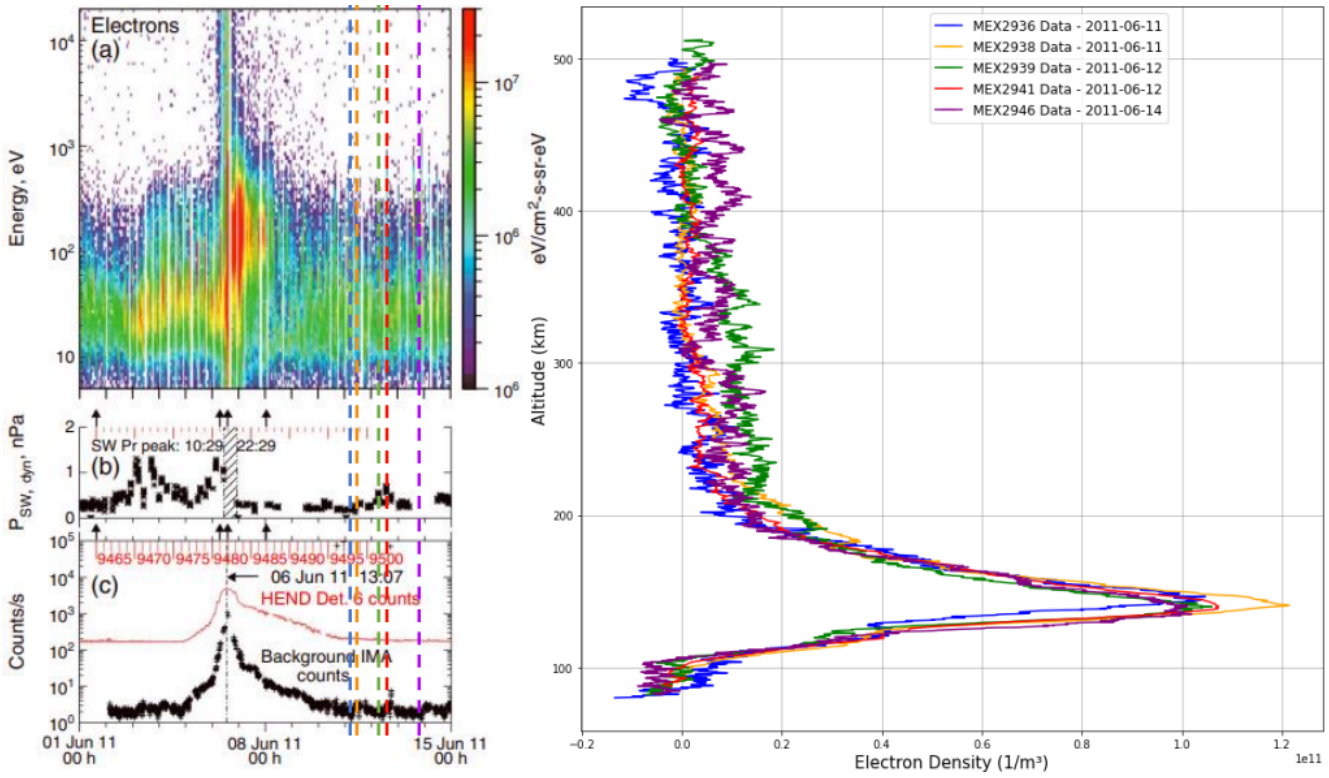

Figure 25: Left: Same ASPERA-3/MEX measurements than presented in the Figure 24 [37]. Vertical dashed lines are included to indicate the timing of the radio occultations listed in Table 3. Right: Vertical electron density profiles (with error bars) retrieved from the radio occultations listed in Table 3. The color of each profile is corresponding to the same color dashed line on the left.

3.2.3 Radio Occultation Atmospheric Profiles during June 2011 CME Impact

As explained in the Section 2, electrons and neutrals have opposite refractivities and the sum of the latter gives the total refractivity of the medium, as shown by the equation (2.56). Usually, the density of one of this type of particles is much greater than the other and small disturbances remain unnoticed. However, at the turbopause and in the upper atmosphere, the refractivity is close to zero, meaning that an extra-ionization could greatly disturb the value of the refractivity. The Figure 26 shows the vertical refractivity profiles retrieved from the radio occultation data listed in Table 3 on different altitude ranges.

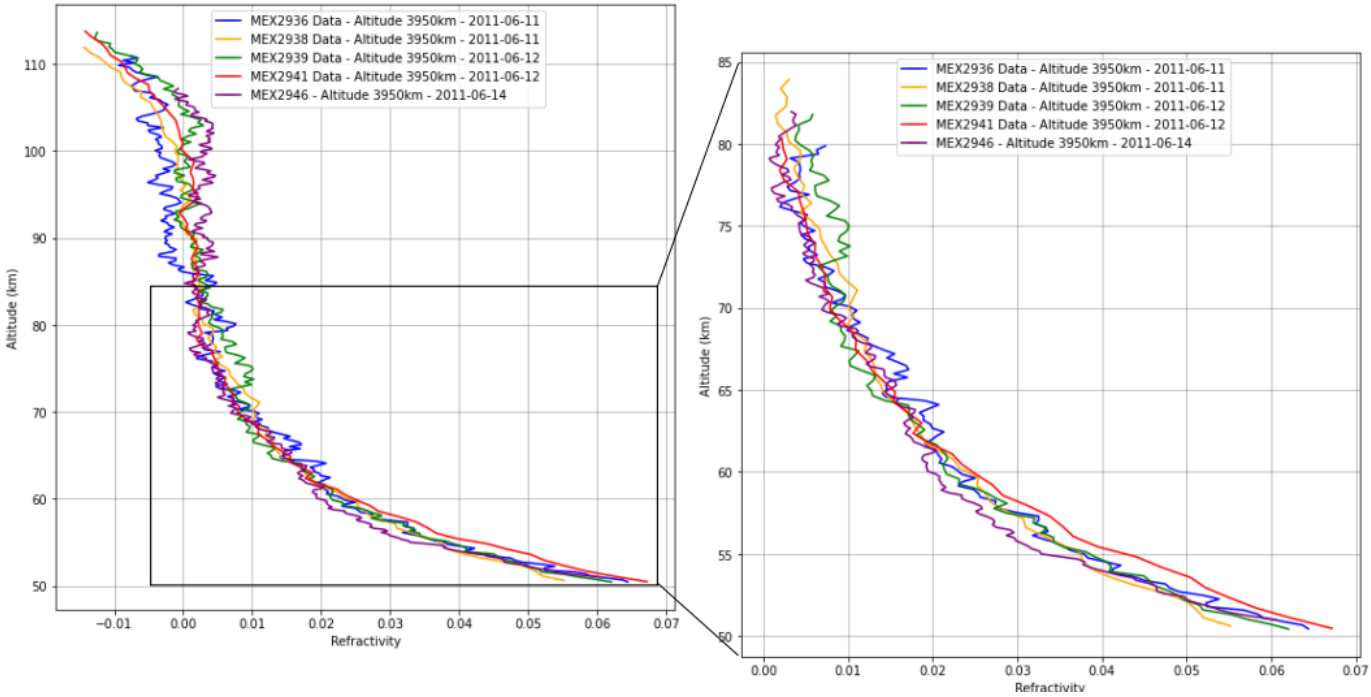

Figure 26: Atmospheric refractivity profiles (with error bars) retrieved from the radio occultation data listed in Table 3. The right plot represents a zoom of the black frame in drawn in the left plot. The colors of the profiles are still referring to the Figure 25.

Two characteristics can be identified from the Figure 26. The first characteristic to underline is that the refractivity profiles derived from radio occultations performed closer in time to the peak of the disturbance caused by the CME (blue, orange, green), exhibit smaller values at the turbopause (here between ∼100 km and ∼85 km) than the ones derived from radio occultations performed later in time (red, purple). This can be observed on the left plot of Figure 26. This is coherent with an extra-ionization of this region as the presence of a small number of additional electrons can overcome the smaller presence of neutrals, which would result in smaller values of the refractivity. This is also coherent with the theory emitted in previous studies for the explanation of radar blackouts [7][8][25][37][40]. However, the structure of the turbopause do not seem to vary. The second characteristic can be observed in the enlarged plot on the right. The refractivity profiles are all exhibiting an increase of the refractivity as the altitude decreases. However, by looking closely at the refractivity

profiles in the upper atmosphere, especially between 50 km and 65 km of altitude, some differences can be observed. One can notice that the profiles derived from measurements closer in time to the disturbance exhibit a refractivity that increases at a smaller rate with decreasing altitude than the other profiles. Once again, this would be coherent with an extra-ionization of the upper atmosphere as the refractivity is equal to the sum of the refractivity induced by the electrons and the one induced by the neutrals. A smaller increase of the refractivity with decreasing altitude can be caused by the additional electrons from the ionization that would inhibit the positive refractivity from the neutrals as electrons are characterized by a negative refractivity. By entering the atmosphere, the SEPs electrons contribute to the refractivity, while ionizing neutral atoms to form more ions and electrons which would further amplify this decrease of the refractivity. This phenomenon is not observed when the disturbance has dissipated. Moreover, the two above characteristics are completely consistent with the chronology of the radar blackouts exposed in the previous subsection.

One could rightfully be doubtful about the second characteristic mentioned above as the slopes of the refractivity profiles are hard to evaluate with naked eyes and this differences could seem small. However, this doubt can be easily lifted by looking at the vertical scale height profiles of these same data. Indeed, since the scale height is inversely proportional to the density of the atmosphere and since the SEPs electrons are supposed to reduce the number of neutral atoms through ionization, such an influence should be directly reflected by larger values of the scale height at these altitudes for the profiles affected by the CME event.

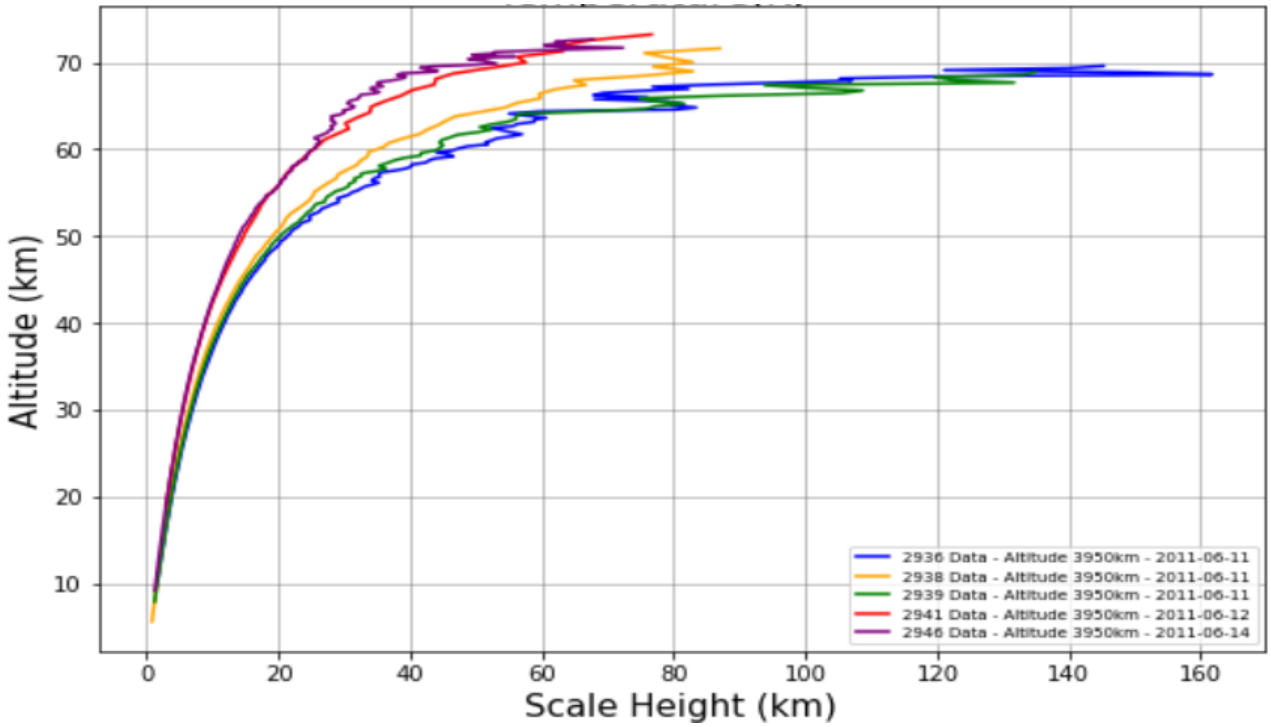

Figure 27: Atmospheric scale height profiles retrieved from the radio occultation data listed in Table 3. The colors of the profiles are still referring to the Figure 25.

One can use the relation beneath to retrieve the expression of the scale height [41]:

$$N_n(z) = N_{n,0} exp\,(-z/H(z)) \tag{3.1}$$

where $N_n(z)$ is the neutral number density at altitude z ,$N_{n,0}$ is an initial condition on the neutral number density (here fixed at 80 km altitude) and $H(z)$ is the scale height at z. The Figure 27 shows the different vertical scale height profiles retrieved from the same data. As expected, the scale height profiles derived from measurements closer to disturbance exhibit a larger scale height in the upper atmosphere, mostly above 40 km. The orange profile would have been expected to be closer to the blue and green profiles as it is chronologically located in between those. However, one should keep in mind that these disturbances are highly dynamic and that their behaviour can change rapidly. This being said, the general tendency described here above remains observable. On the contrary, the profiles that are not or less affected exhibit lower values for their scale heights in the upper atmosphere. At 60 km altitude, the scale heights of the unaffected profiles are nearly two times smaller than the scale heights of the affected ones. This supports the fact that this extra-ionization is indeed impacting the upper neutral atmosphere and, in a lesser way, the turbopause.

As an extra-ionization is taking place in the upper atmosphere during this CME impact, an increase of the temperature should be measured at these altitudes. This would also justify the vertical scale height profiles presented in the Figure 27 as the scale height also depends on the temperature through the relation [41][42]:

$$H = \frac{kT}{mg} \tag{3.2}$$

where T is the temperature, k is the Boltzmann's constant, m is the mean molecular mass of the atmosphere and g is the gravitational acceleration of the body.

Our first approach is to compare the vertical temperature profiles retrieved from the radio occultation measurements with the outputs of two global climate models of the Martian atmosphere. These models take into account the geocentric location, the local time, the dust storms, the solar longitude as well as the usual global climate dynamics. However, these do not consider the effects of the SEPs and CME events. This comparison allows to correlate the origin of an increase of the temperature measured in the upper atmosphere with the CME impact. Indeed, if an increase of the temperature is measured with respect to the models, this would support that the cause of this increase is not considered by the models, such as a CME impact. As a second approach to further prove that the origin of the temperature spike is indeed caused by the CME, the different profiles are then compared between each other in order to verify the coherence with the chronology of the SEPs and CME impact.

The Figure 28 presents the vertical temperature profiles derived from two of the radio occultations performed during the CME impact compared with the outputs of the Mars Global Climate Model (GCM) LMD developed by the Laboratoire de Météorologie Dynamique/Institut Pierre Simon Laplace (LMD/IPSL) in red [43] and the outputs of the Mars Global Climate Model WRF

developed by the ROB (ROB WRF) in black [44], the latter being a version of the original PlanetWRF model developed by Richardson et al. (2007) [45]. The MEX data files used here are the MEXMRS-2936 (Figure 28, top) and the MEXMRS-2946 (Figure 28, bottom). The former contains measurement when the disturbance was active, where the latter contains data when it was dissipated. In each plot, the three vertical temperature profiles from this study in green, orange and blue are using different initial conditions on the temperature at 80 km altitude which are respectively set at 200 K, 165 K and 130 K. This is done in order to ensure to sample the whole range of values that the temperature of the neutral atmosphere can take at this altitude (cf. Section 2.3.4). However, one can see that even with different initial conditions on the temperature at the boundary layer, the temperature profiles are nearly identical. These profiles are plotted from the surface to roughly 70 km as the uncertainties become too large for higher altitudes.

For both dates and below 30 km of altitude, the measurements are very similar to the outputs of the two GCMs used in this study. However, one can clearly see that on the 11^{th} of June (Figure 28, top), the vertical temperature profiles measured exhibit a large increase between 40 km and 70 km compared to the models' outputs. The differences in temperature between the models and the measurements can be as great as a 100 K. Additionally, the temperature profiles of the 14^{th} of June (Figure 28, bottom) do not show such discrepancies with the models' outputs. For this latter measurement, the error bars fully cover the outputs of the models and only a slight temperature spike is exhibited by the measurement at 50 km altitude. This suggest firstly that at times of high disturbance of the atmosphere and ionosphere by the CME and the SEPs, the upper atmosphere exhibits structural modification equivalent to a large temperature increase of a few tenths of Kelvin between 40 km and 70 km altitude. This is totally coherent with an extra-ionization of the neutral atmosphere at these altitudes [7][8][25][37]. However, the temperature is an equivalent temperature representing a structural change of the medium and not the results of a real heating. The temperature might increase due to collisions of SEP with neutrals but not up to the values plotted in the Figures. The notion of equivalent temperature, represented here, is a value that would rather quantify the structural change of the atmosphere due to the ionization which would be equivalent to a change of the true temperature. This notion is used for the rest of this study and is simply referred hereafter as the temperature. This also corroborates the larger atmospheric scale heights measured during this CME induced disturbance. On the contrary, the temperature profiles measured on the 14^{th} of June, when the disturbance has dissipated, do not show large temperature spikes and are very similar to the outputs of the GCMs. This further suggests that the SEPs electrons are causing the atmospheric disturbance and the radar blackouts, as the models do not take into account the effects of SEP. One could also argue that the small temperature increase located at 50 km is a remnant signature of the original upper atmospheric disturbance measured earlier.

The same comparison was made for all the other data files and showed similar results. The three first MEX radio occultations measurements listed in Table 3 show large temperatures increases at similar altitudes as the one observed in Figure 28 (top). However, the two last measurements are not exhibiting such atmospheric disturbances. This is completely coherent with the radar blackouts, the CME chronology and the previous results presented in the Figure 26 and 27, which tend to correlate these equivalent temperature spikes with the SEPs electrons disturbances [8][25][37][40].

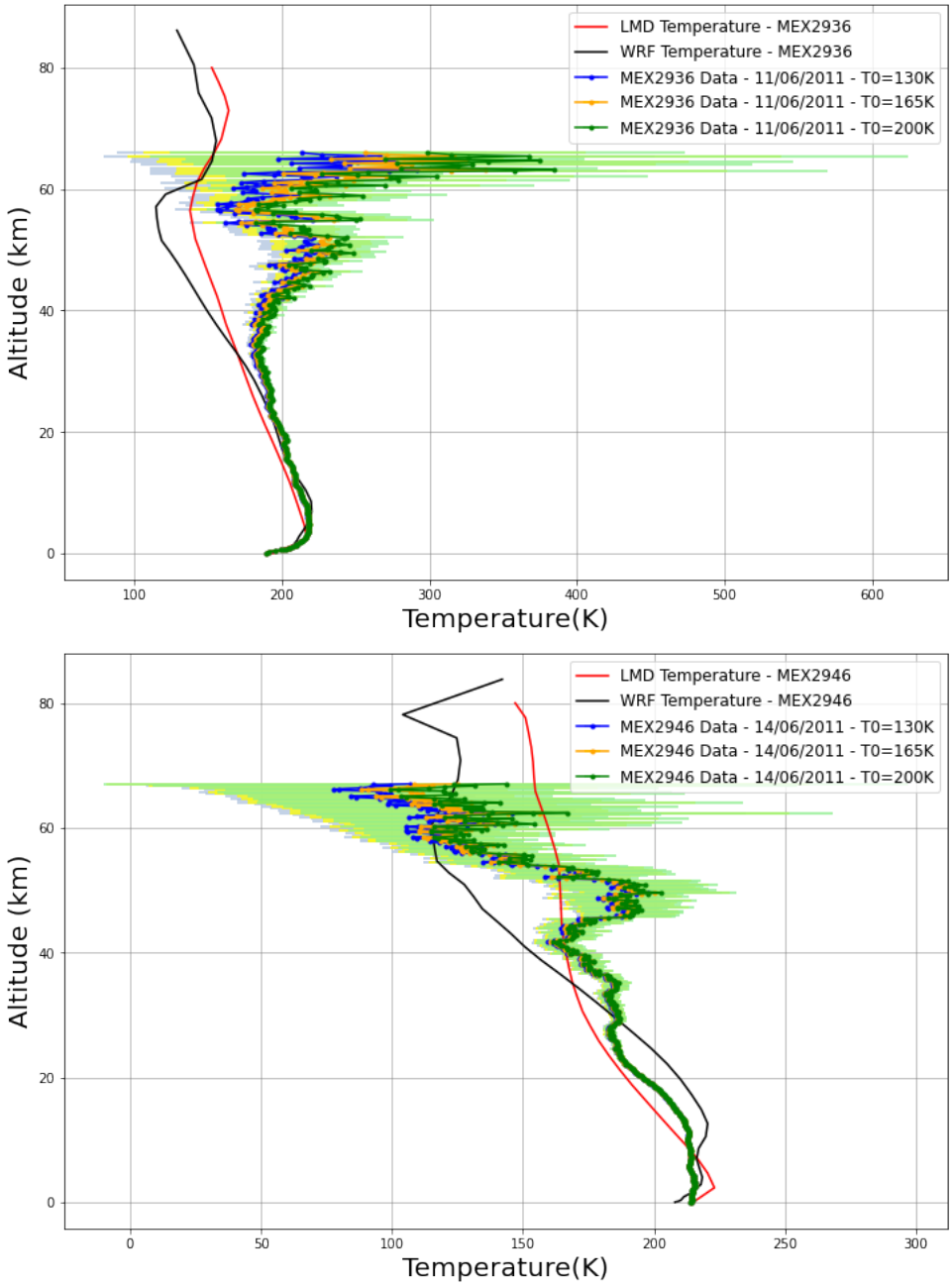

Figure 28: Top: Vertical atmospheric temperature profiles retrieved from the data file MEXMRS-2936 compared with the corresponding outputs of LMD and WRF models, respectively in red and black. This radio occultation was performed during the atmospheric disturbance caused by the CME. Bottom: Vertical atmospheric temperature profiles retrieved from the data file MEXMRS-2946 compared with the corresponding outputs of LMD and WRF models. This radio occultation was performed after the atmospheric disturbance caused by the CME. The three different profiles in green, orange and blue use different initial conditions on the temperature at the boundary layer set at 80 km (respectively 200 K, 165 K and 130 K)[6][19]

By plotting all the vertical temperature profiles retrieved from the data files in Table 3, one can compare the different atmospheric disturbances of each profile (if there is one) and observe the chronological evolution of the effects of SEPs on the neutral atmosphere temperature. This comparison is presented in the Figure 29. This can also be compared with the SEPs flux measurements in the Figure 25 as the colors used in the latter are corresponding to the ones of the vertical temperature profiles.

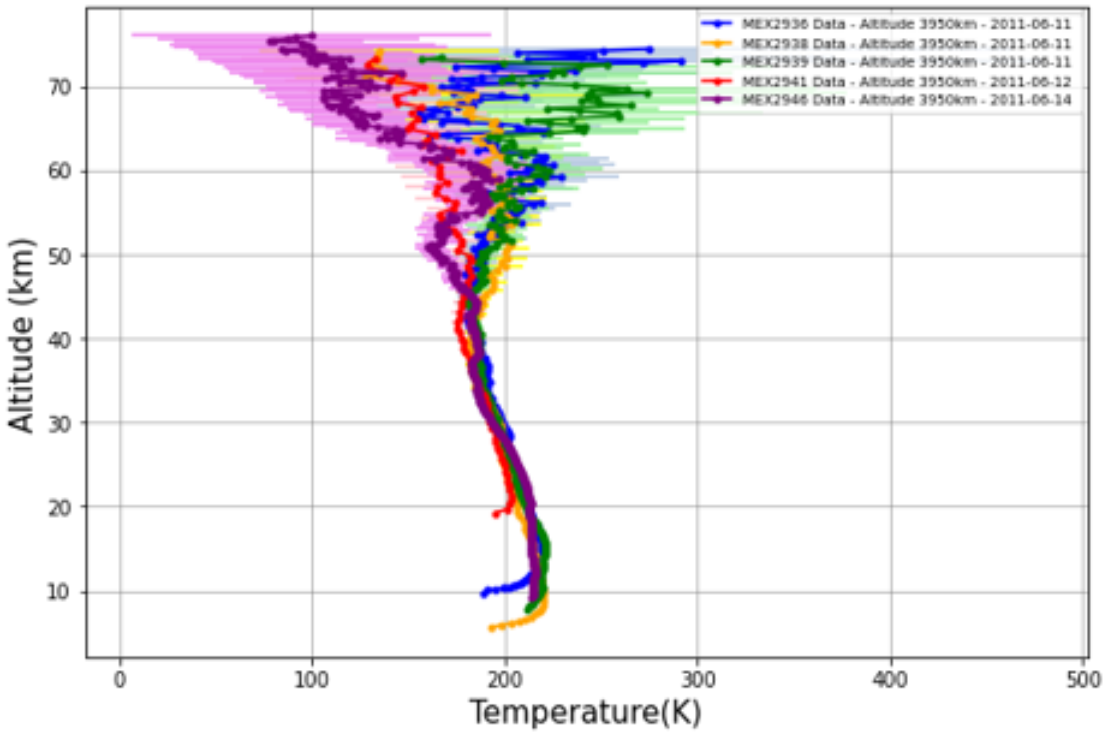

Figure 29: Vertical atmospheric temperature profiles retrieved from the data file listed in Table 3. The initial condition on the temperature set at 80 km altitude is the same for all the profiles ($T_0 = 130K$) and is based on the GCMs outputs. The profiles' colors correspond to the ones displayed in the Figure 25. All the profiles start at different lower altitudes as this depends on the local conditions of the measurements (topography, geocentric coordinates,...). The altitude is here computed as being the difference between the distance from the radio signal to Mars center and an average radius of Mars (cf. Section 1.1).

The Figure 29 shows that all the temperature profiles measured are similar below 30 km. However, during the disturbance by the CME, the temperature profiles (blue, orange and green) exhibit larger values of a few tenths of Kelvin between 40 km and 70 km than the profiles measured when the disturbance has dissipated (red and purple). This suggests that the atmospheric disturbance is caused by the interactions of the SEPs and the CME with the Martian atmosphere. The purple profile still exhibits a small temperature peak at an altitude of 50 km. This can be caused by the dissipation of the disturbance observed in the blue, orange and green. The red temperature profile

is very different compared to the others as this measurement was performed just over one of the volcanoes of Tharsis Montes, which increases greatly the altitude of the surface of about 10.5 km [13]. As this modifies the local structure of the neutral atmosphere, this profile is not further studied here.

In summary, this case study's results suggest that the increase of the SEPs electrons flux caused by the June 2011 CME, which is correlated to the radar blackouts, would be responsible for the large disruption of the refractivity, and thus of the density of the upper neutral atmosphere, between 40 km and 90 km. This can be explained by an extra-ionization of this region induced by the SEPs electrons. The electrons originating from neutrals' ionization and the SEPs electrons themselves have an opposite effect on the refractivity compared with the neutral atoms, which can explain the differences of slopes of the refractivity profiles. This effect is only observed for radio occultation measurements performed when radar (partial) blackouts were observed, suggesting that both are correlated. The atmospheric scale heights analysis of these different measurements are coherent with this explanation as they present larger scale heights during the SEPs disturbance, which would corroborate the decrease of neutral density in the upper atmosphere due to an extra-ionization. Additionally, on the 11^{th} of June and morning of the 12^{th} of June, the temperature profiles exhibit larger values above 40 km when compared to both the outputs of models not considering the effects of SEPs and the temperature profiles not subject to the SEPs disturbance. This would suggest that an increase in the SEPs electron flux is causing an extra-ionization which would be responsible for these atmospheric disturbances. This was already suggested by many previous studies on radar blackouts and CMEs interactions with the Martian ionosphere and atmosphere [7][8][25][37][39][40], but no evidence of this effect was yet presented.

3.3 Case Study 2 - CME Impact on Mars during February/March 2015

3.3.1 Chronology and Properties of the Event through Various Measurements

This second case study is analysing the CME event that impact the Martian atmosphere between the 22^{nd} of February and the 15^{th} of March 2015. This event is interesting as it presents three distinct SEP events measured by MAVEN. The Figures 30.a, b and c show respectively the MAVEN's measurement of the EUV irradiance, of the SEP ions spectra and of the SEP electrons spectra as functions of time (in days). The Figure 30.d presents times of MARSIS (squares) and SHARAD (diamonds) operations. The red filled squares/diamonds represent the total blackouts whereas the blue filled squares/diamonds represent the partial blackouts [8]. This period is divided in three enhancements of SEPs ions and electrons. The first enhancement is weak and occurred only on the 22^{nd} of February, the second increase started on the 27^{th} of February and lasted until the 4^{th} of March and the third one occurred between the 6^{th} and the 10^{th} of March [8][39]. The two last SEP events were stronger and longer, so radio occultations are thus expected to present large disturbances in their measurements at these times. However, the CME that impacted Mars during this period was weaker than in the first case study. The disturbance are thus expected to be smaller.

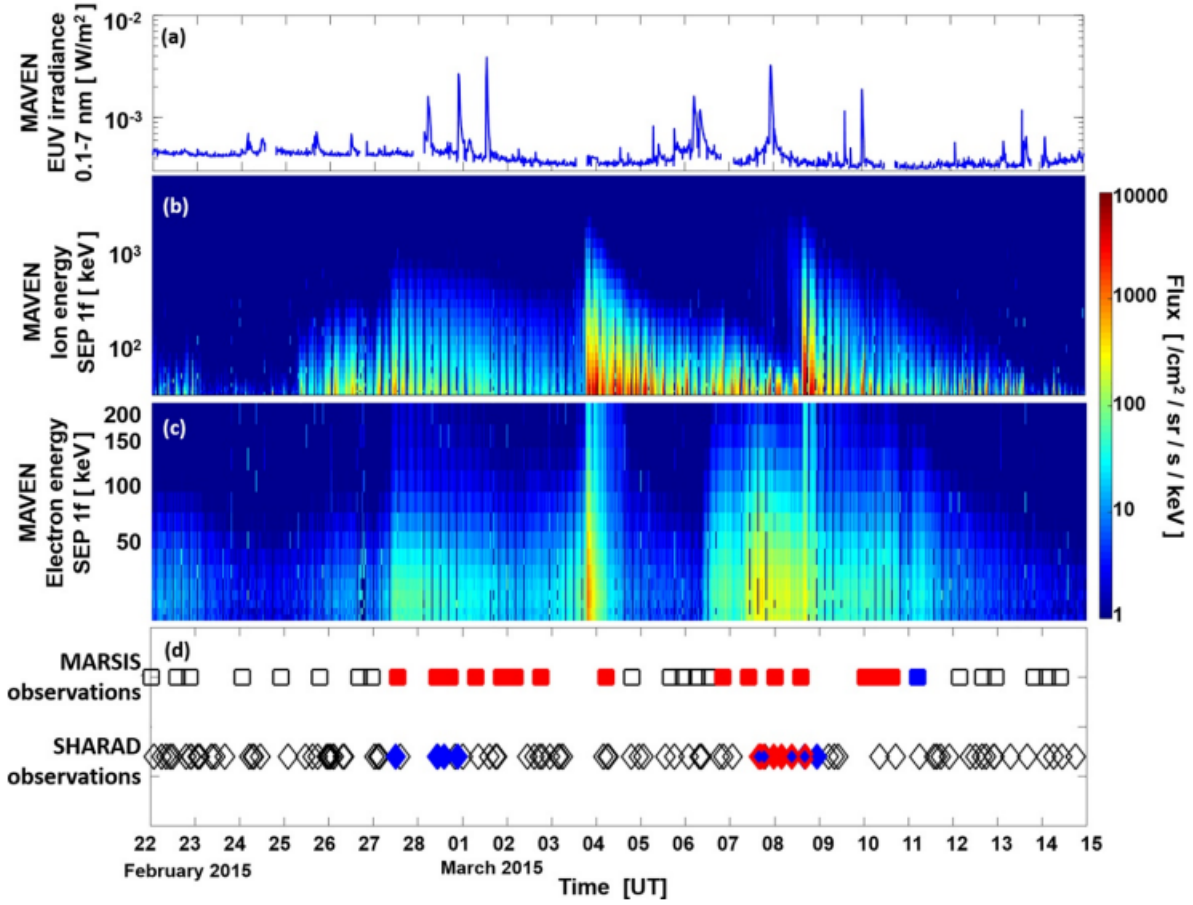

Figure 30: (a) MAVEN EUVM irradiance observations. (b) MAVEN SEP ion spectra. (c) MAVEN SEP electron spectra. (d) Times of MARSIS (squares) and SHARAD (diamonds) operations. Operations with blackouts are filled in red and the ones with partial blackouts are filled in blue[8].

3.3.2 Radio Occultation Ionospheric Profiles during 2015 CME Impact

In the same way that in the first case study, the radio occultation measurements listed in the Table 4 are used to study this 2015 CME event. The Table 4 is organised in the same way as the Table 3. The measurements were performed on the 23^{rd} and 26^{th} of February as well as on the 2^{nd} and 5^{th} March 2015. By comparing the date of the measurements with the chronology of MAVEN's measurements, one would expect to see large disturbances in the first and in the last radio occultations.

Similarly as in the case study 1, the first quantity that is here analysed is the electron density as one would be expecting an increase of this value since an extra-ionization is taking place, leading to a radio signal attenuation [7][8]. The Figure 31 represents the vertical electron density profiles in the Martian ionosphere retrieved from the four data files listed in Table 4 (right) and the MAVEN measurements with vertical dashed lines with colors corresponding to their respective profile (left). As in the first case study, no particular influence of the CME interactions with the Martian iono-

sphere is observable as all profiles are fairly similar. Once again, the disturbance is expected lower, in the upper atmosphere.

Date	Vol ID	Longitude (Geocentric) (deg)	Latitude (Geocentric) (deg)	Local Solar Time	Ls (deg)	SZA (deg)
2015-02-23	MEXMRS_3700	211.130728	-60.823499	08:23:14 P.M.	296.476200	85.853805
2015-02-26	MEXMRS_3701	161.863050	-59.000139	07:56:35 P.M.	298.404636	84.755341
2015-03-02	MEXMRS_3703	268.429832	-56.496189	07:29:46 P.M.	300.672880	83.571990
2015-03-05	MEXMRS_3706	220.962702	-54.153071	07:10:29 P.M.	302.582816	82.659122

Table 4: Table listing the data files ID of MEX MaRS radio occultations used in the analysis of the impact of the February/March 2015 CME, along with the dates of the radio occultations, the geocentric latitudes and longitudes of the measurements, the local solar times, the solar longitudes and the solar zenith angles.

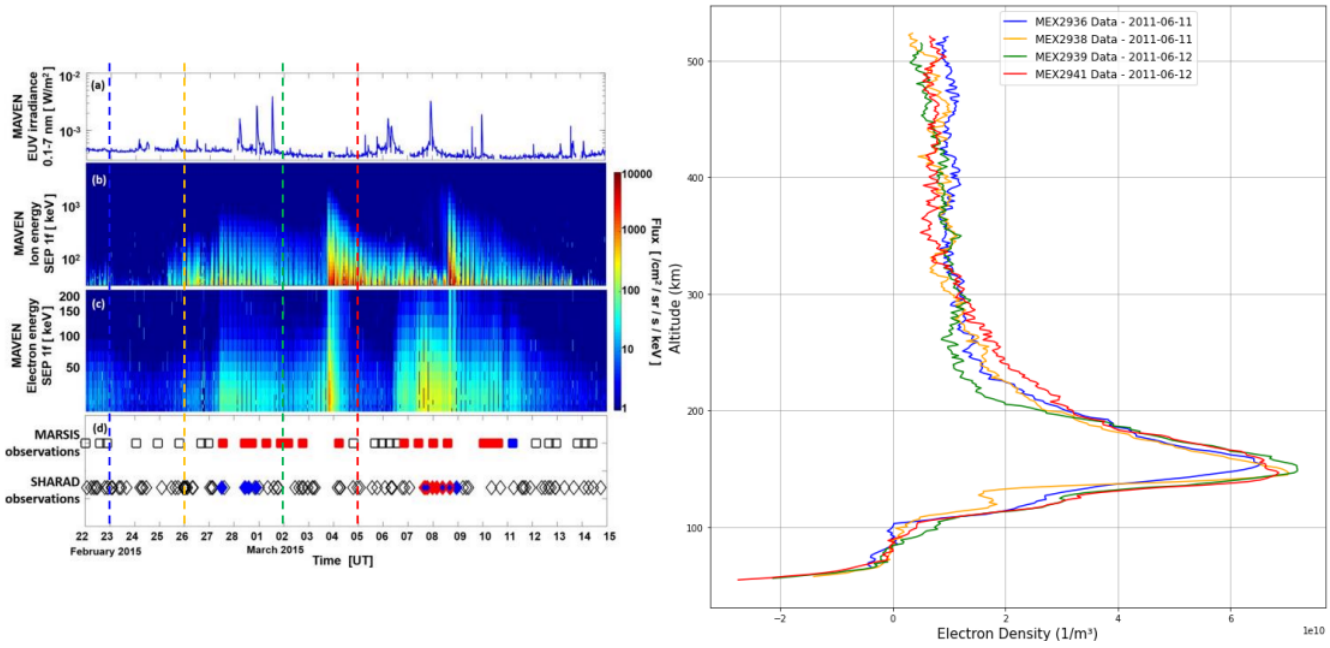

Figure 31: Left: Same MAVEN measurements than the ones presented in the Figure 30 [8]. Vertical dashed lines are included to indicate the timing of the radio occultations listed in Table 4. Right: Vertical electron density profiles (with error bars) retrieved from the radio occultations listed in Table 4. The color of each profile is corresponding to the same color dashed line on the left.

3.3.3 Radio Occultation Atmospheric Profiles during 2015 CME Impact

In order to study a potential impact of the SEPs electrons on the turbopause and on the upper neutral atmosphere, the vertical refractivity profiles are here again plotted for this region. The Figure 32 presents the vertical refractivity corresponding to the radio occultations listed in Table 4.

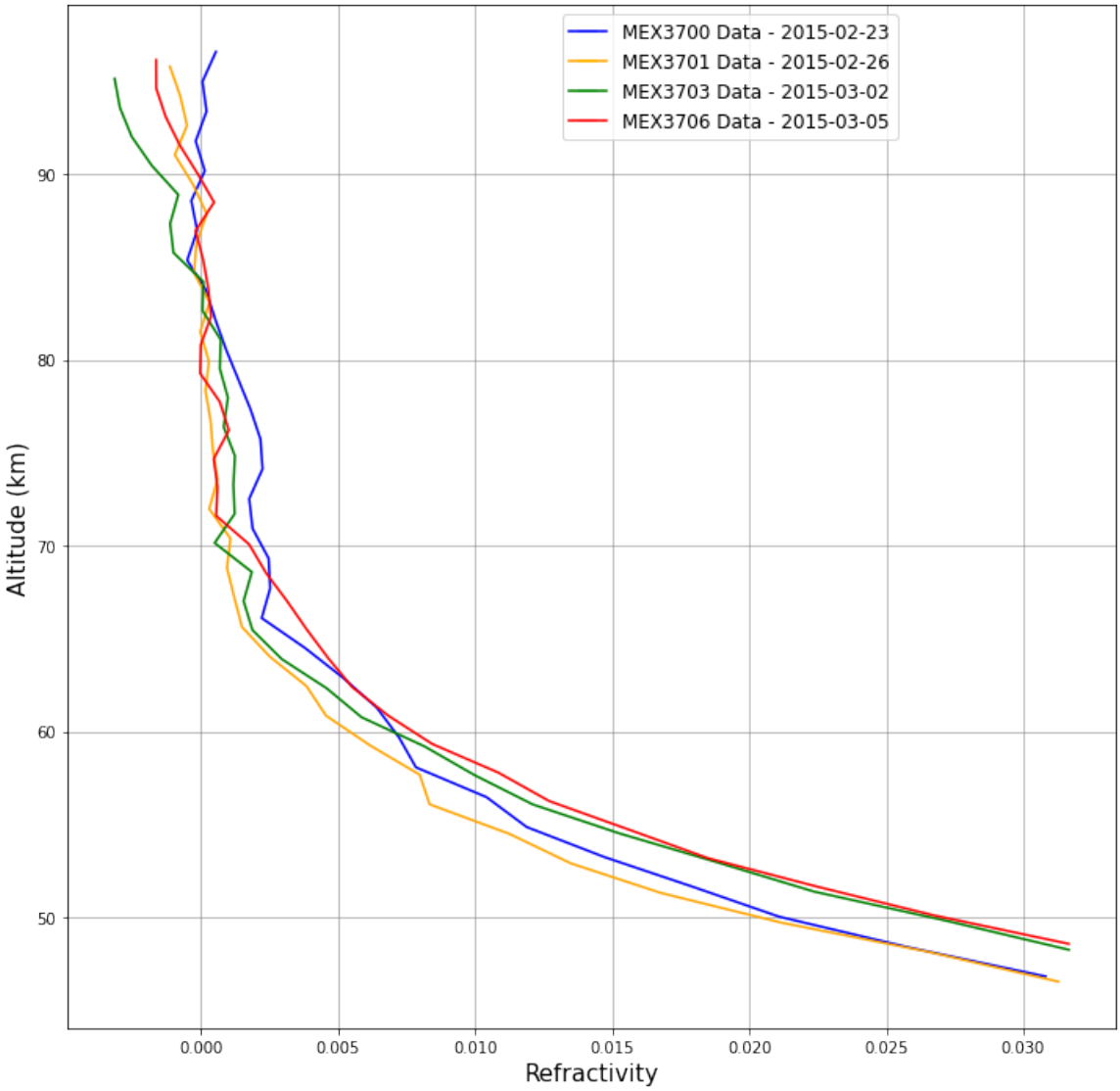

Figure 32: Atmospheric refractivity profiles (with error bars) retrieved from the radio occultation data listed in Table 4. The colors of the profiles are still referring to the Figure 30.

One can clearly see that the first radio occultation performed the day after the first SEP event clearly exhibits a refractivity profile (blue) with a steeper slope than the other profiles, indicating potential disturbance due to an ionization, similarly to the previous case study. However, the last

radio occultation measurement presents a refractivity profile (red) that is more similar to the ones that are not or less affected by the SEP events, even if this radio occultation was made a day after a large SEP event detection by MAVEN (see Figure 30). This might be explained by the low SEP electrons flux at this moment, combined with the fact that this 2015 CME event was weaker than the one in 2011, so the disturbances were weaker as well and should have lasted for shorter periods. This explanation would be coherent with the radar blackouts that are this time only happening during or very close to the SEPs events described above, meaning that the electron density enhancements in the atmosphere did not last more than a day after each event.

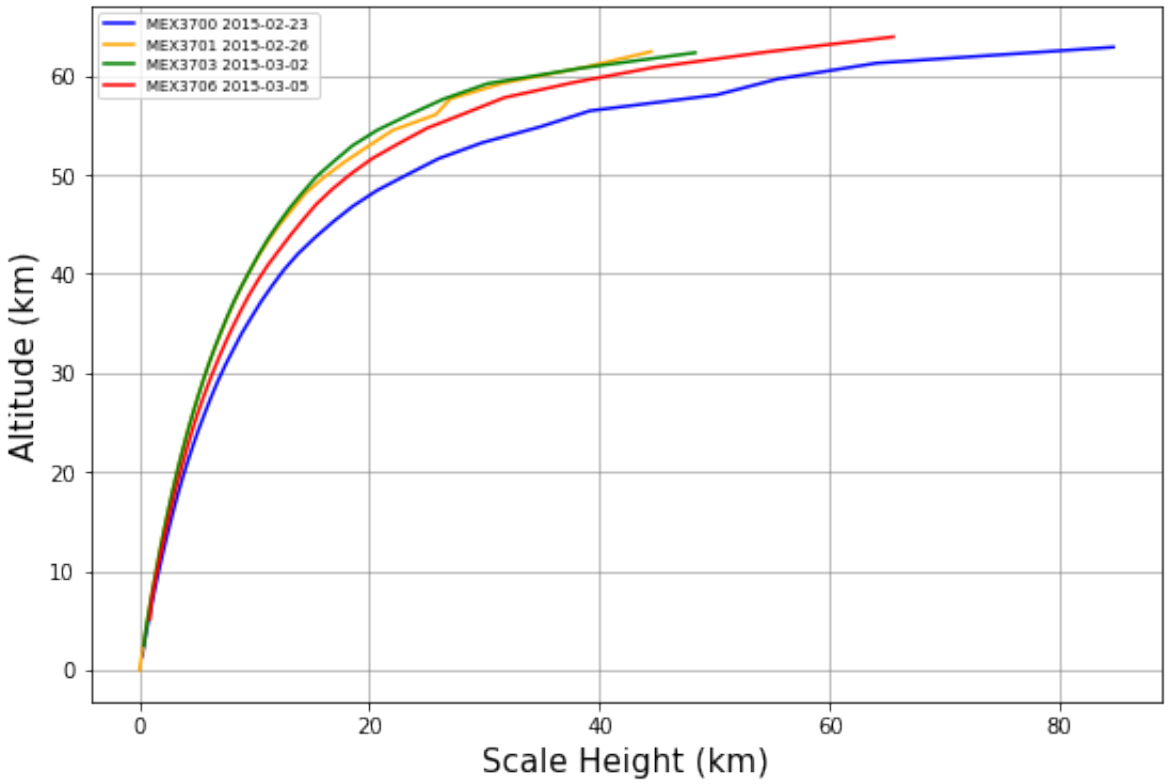

Figure 33: Atmospheric scale height profiles retrieved from the radio occultation data listed in Table 4. The colors of the profiles are still referring to the Figure 30.

The above observations are confirmed by the Figure 33 which is showing the corresponding vertical scale heights profiles. One can clearly see that the first radio occultation performed a day after the 22^{nd} of February SEP event (blue) exhibits larger scale heights above 40 km compared to the other profiles, which suggests that the SEPs electrons have ionized this region and have removed some neutrals, influencing the scale heights. The red profile, which corresponds to the last radio occultation, exhibits an in-between case with a scale height that is larger than the ones without disturbance, but smaller than the ones from the blue profile. This radio occultation was performed when the flux of SEP electrons was particularly low but it was also made just a day after a large enhancement of SEPs electrons. This profile suggests that the electron density enhancement

from the previous SEP event was still present but that the system was evolving towards its original structure without any disturbance [8][37]. The last two profiles seem unaffected by the SEP events. These signatures are completely coherent with the ones from the case study 1 and corroborate that the SEPs electrons are responsible for an extra-ionization of the neutral atmosphere inducing a disturbance in the density of the upper atmosphere [7][8][25][37][39].

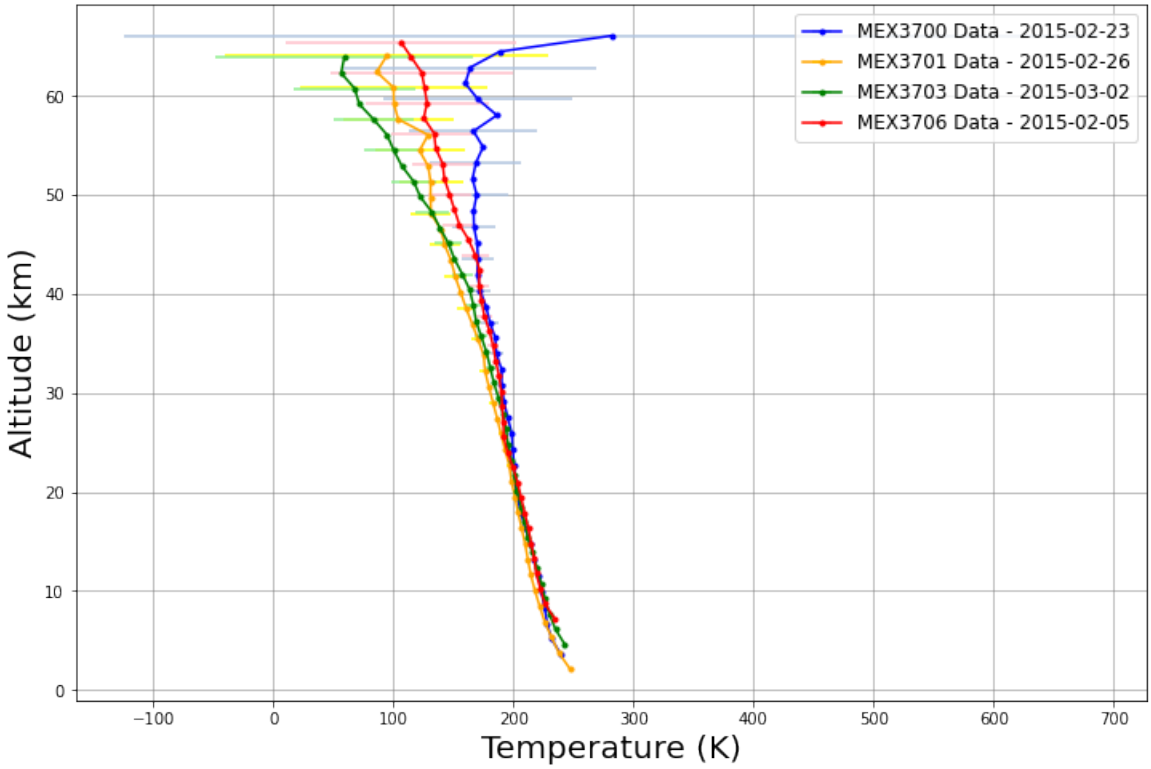

Figure 34: Vertical atmospheric temperature profiles retrieved from the data file listed in Table 4. The initial condition on the temperature set at 80 km altitude is the same for all the profiles ($T_0 = 130K$) and is based on the GCMs outputs. The profiles' colors correspond to the ones displayed in the Figure 30.

The Figure 34 presents the temperature profiles for the same radio occultations already studied in this case study. Above 40 km of altitude, the temperature profile retrieved from the first radio occultation (blue) exhibits a larger temperature than the profiles unaffected by the SEP disturbance (orange and green), with differences growing as large as 80 K. The temperature profiles are similar below 40 km altitude. Once again, this suggests that the extra-ionization caused by the SEP electrons induces an increase of the temperature above 40 km when compared to the profiles that are undisturbed. This is coherent with the larger scale heights presented by the same measurements and is completely consistent with the characteristics observed in the first case study. The smaller maximum temperature difference could be attributed to the weaker CME event in 2015 when compared to the CME impact of 2011. The red temperature profile shows slightly larger

temperature than the undisturbed profiles. This further suggests that this is an in-between case presenting the atmosphere that is recovering from a SEP disturbance. The temperature differences are in this case of only $\sim$ 30 K.

All the above results are coherent with the results of the case study 1, the radar blackouts and the chronology of the SEPs events measured by MAVEN. This tends to corroborate that the SEPs electrons are indeed inducing an extra-ionization of the upper atmosphere of Mars, above 40 km, which is modifying the density of the medium as well as disturbing its structure [7][8][25][37][39].

4 Conclusion and Perspectives

In the last few years, radar blackouts have been intensively studied and correlated to the SEP and CME events by Sánchez–Cano et al. (2017) and later on by Lester et al. (2022)[7][8]. It has been theorised that the SEP electrons precipitating in Mars' ionosphere and atmosphere are responsible of an extra-ionisation of the Martian atmosphere inducing an increase of the electron density in this region [7][8][25]. As the signal attenuation is directly proportional to the electron density, this phenomenon would explain that the radars MARSIS and SHARAD are incapacitated during the detections of such events by MEX and MAVEN [2][8][37]. The disturbance of the Martian atmosphere by a CME can last a few days, incapacitating radars for sometimes 6 days [37]. However, since the radars cannot take measurements during these SEP events as they experience blackouts, no evidence of the effects of this extra-ionization on the physical properties of the atmosphere of Mars was observable [37].

In this study, radio occultation measurements performed at time of SEP events on Mars were used to determine experimentally the effects of the SEP electrons on the physical properties of the Martian ionosphere and atmosphere. Indeed, radio occultations are operating at frequencies that are much greater than the ones used by MARSIS and SHARAD, avoiding them to be affected by a large attenuation of the signals [2]. By using the geometry of the radio signals, modified by their crossing of the ionosphere or the atmosphere, one can retrieve the vertical refractivity, density, temperature and pressure profiles[5][6][18][19][30][31]. However, a global study of both the ionosphere and the atmosphere was never performed during the SEP events as the two media were always studied independently. This represents a real novelty in this study as it allows to locate the extra-ionization region and the boundary layer between the ionosphere and the atmosphere.

In both case studies presented in this work, the MEX data selections were based on other measurements from MAVEN and MEX, on the blackout periods of MARSIS and SHARAD, but also on the availability of the radio occultation measurements. Indeed, the MaRS on board of MEX is not performing radio occultations continuously leaving some periods with no measurement [18][19]. However, some radio occultations were performed during and around the CME impacts of 2011 and 2015, allowing to conduct our case studies. In both cases, the ionosphere of Mars does not exhibit any increase of its electron density during the SEP events meaning that the extra-ionization is happening in the neutral atmosphere. Ulusen et al. (2012) performed similar analysis on the ionosphere of Mars during the CME impact of 2011 and did not observe any modification of the electron density in this region, also concluding that the extra-ionization should be observed in the atmosphere [40]. Indeed, the analysis of the neutral atmosphere shows multiple changes of its physical properties during the SEP events. Firstly, radio occultations performed during SEP events reveal a lower refractivity in the turbopause than for the measurements performed when the disturbance has dissipated. This gives information on the electron and on the neutral densities as they are both influencing the refractivity in opposite ways: electrons induce a negative refractivity and neutrals induce a positive refractivity. This phenomenon is thus coherent with an extra-ionization caused by the SEPs electrons in this region as the turbopause is near an equilibrium between the electron and the neutral densities (with a zero total refractivity)[34] so a small ionization of the medium would increase the electron density and decrease the neutral density, resulting in a global decrease of the refractivity. The vertical refractivity profiles of the upper atmosphere of Mars, between 40 km and 80 km altitude, also exhibit steeper slopes during SEP events. Once again, this suggests that an

extra-ionization of the medium by SEP electrons is reducing the neutral density at these altitudes while increasing the electron density. This would lead to a smaller increase of the refractivity with decreasing altitude than what would be observed without a SEP disturbance of the atmosphere. This phenomenon is further suggested by an analysis of the vertical scale height profiles. Since the atmospheric scale height is inversely proportional to the neutral density, a decrease in the neutrals induced by ionization has to be associated with an increase of the scale heights at these altitudes. This is indeed observed in both case studies presented with scale heights that sometimes are twice greater during a SEP disturbance than the scale heights observed when the disturbance has dissipated.

An extra-ionization of the upper atmosphere is expected to induce a perturbation of the upper atmosphere through an increase of the temperature [8][25][37]. The vertical temperature profiles derived from radio occultation measurements during or close to an SEP electrons enhancement show large increases of the temperature between 40 km and 80 km altitude when compared to the temperature profiles from measurements with no SEP enhancement. The difference between profiles can peak to 100 K during the stronger CME event of 2011. When compared to the outputs of global climate models of Mars that are not including the effects of SEP enhancement, large temperature excesses of 100 K are also observed in the profiles from the radio occultations performed close to a SEP event [43][44][45]. This is not the case for the profiles derived from the measurements performed later in time after the CME impact. Only some small excesses of temperature can be observed at similar altitudes, suggesting that they are only due to the resorption of the original atmospheric disturbance created by the SEP events. These temperature increases are totally coherent with an extra-ionization of the upper atmosphere of Mars by the SEP electrons as they are consistent with MAVEN measurements of the enhancement of the SEP electrons flux and with the radar blackouts of MARSIS and SHARAD [7][8][37]. Additionally, these atmospheric disturbances also corroborate the increases of the scale heights during SEP events as the atmospheric scale heights are also proportional to their temperatures. The results of this study strongly suggest that the SEP electrons are responsible for an extra-ionization of the upper atmosphere of Mars, between 40 km and 80 km of altitude, inducing an enhancement of the electron density as well as a decrease of the neutral density. These latter changes are influencing the refractivity of the medium. Moreover, the thermal analysis of the atmosphere further suggests that the ionization from the SEP electrons increases largely the equivalent temperature at similar altitudes, perturbing the atmosphere and its structure [25].

This study could be extended by analysing other periods of SEP or CME events on Mars as these are quite frequents and more radio occultation data are available. Some large CME events have caused longer radar blackouts in February 2012 and in January 2014 and those would be interesting to study. The use of other source of radio occultation measurements such as MGS or MAVEN spacecrafts could also help to study these CME impacts on the Martian atmosphere. Ideally, a complete study over a full solar cycle, as the one performed on the radar blackouts by Lester et al. (2022), should be conducted over the same periods to correlate statistically the changes in the atmospheric physical properties observed during the SEP and the CME events to the radar blackouts and to the SEP electrons enhancements measured by MAVEN. Finally, the temperature profiles measured could also be compared to the outputs of Mars global climate models that include the SEP and the CME events to verify if the extra-ionization caused by the SEP electrons is the

only phenomenon inducing these changes of the physical properties of the upper atmosphere. Until continuous in-situ measurements are available for the upper atmosphere of Mars (between 40 km and 150 km of altitude), radio occultations remain the only measurements allowing to infer these physical properties during SEP and CME events. In the future, an alternative would be spacecrafts' constellations performing radio occultations which would allow a more global and continuous monitoring of the Martian environment. Ground stations on Mars would also allow to perform radio occultations of the Martian atmosphere and ionosphere in an easier way.

References

[1] Sheehan, W. (1996). The planet Mars: A history of observation & discovery. University of Arizona Press.

[2] Ho, C., Golshan, N., & Kliore, A. (2002). Radio wave propagation handbook for communication on and around Mars (No. JPL-Publ-02-5).

[3] Haberle, R. M., Clancy, R. T., Forget, F., Smith, M. D., & Zurek, R. W. (Eds.). (2017). The atmosphere and climate of Mars: Introduction. Cambridge University Press.

[4] Haberle, R. M., Clancy, R. T., Forget, F., Smith, M. D., & Zurek, R. W. (Eds.). (2017). The atmosphere and climate of Mars: Understanding Mars and Its Atmosphere. Cambridge University Press.

[5] Kliore, A., Cain, D. L., Levy, G. S., Eshleman, V. R., Fjeldbo, G., & Drake, F. D. (1965). Occultation experiment: Results of the first direct measurement of Mars's atmosphere and ionosphere. Science, 149(3689), 1243-1248.

[6] Tellmann, S., Pätzold, M., Häusler, B., Hinson, D. P., & Tyler, G. L. (2013). The structure of Mars lower atmosphere from Mars Express Radio Science (MaRS) occultation measurements. Journal of Geophysical Research: Planets, 118(2), 306-320.

[7] Sánchez–Cano, B., Blelly, P. L., Lester, M., Witasse, O., Cartacci, M., Orosei, R., ... & Kopf, A. J. (2019). Origin of the extended Mars radar blackout of September 2017. Journal of Geophysical Research: Space Physics, 124(6), 4556-4568.

[8] Lester, M., Sanchez-Cano, B., Potts, D., Lillis, R., Cartacci, M., Bernardini, F., ... & Russell, A. (2022). The impact of energetic particles on the Martian ionosphere during a full solar cycle of radar observations: Radar blackouts. Journal of Geophysical Research: Space Physics, 127(2), e2021JA029535.

[9] Dehant, V., Internal geophysics of the Earth and terrestrial bodies of the solar system (2021) Course at the University of Liège.

[10] Official Website of NASA, NASA website about InSight Mission, https://www.nasa.gov/feature/jpl/nasa-s-insight-reveals-the-deep-interior-of-mars

[11] Official Website of NASA, NASA website about Mars and the Solar System, https://solarsystem.nasa.gov/planets/mars/in-depth/

[12] Stevenson, D. J. (2003). Planetary magnetic fields. Earth and planetary science letters, 208(1-2), 1-11.

[13] Official NOAA website, NOAA website on the topography of Mars and MOLA instrument, https://sos.noaa.gov/catalog/datasets/mars-topography/

[14] Catling, D. C. (2014). Mars atmosphere: History and surface interactions. In Encyclopedia of the solar system (pp. 343-357). Elsevier.

[15] McCleese, D. J., Heavens, N. G., Schofield, J. T., Abdou, W. A., Bandfield, J. L., Calcutt, S. B., ... & Zurek, R. W. (2010). Structure and dynamics of the Martian lower and middle atmosphere as observed by the Mars Climate Sounder: Seasonal variations in zonal mean temperature, dust, and water ice aerosols. Journal of Geophysical Research: Planets, 115(E12).

[16] Medvedev, A. S., Kuroda, T., & Hartogh, P. (2011). Influence of dust on the dynamics of the Martian atmosphere above the first scale height. Aeolian Research, 3(2), 145-156

[17] Bertucci, C., Duru, F., Edberg, N., Fraenz, M., Martinecz, C., Szego, K., & Vaisberg, O. (2011). The induced magnetospheres of Mars, Venus, and Titan. Space science reviews, 162(1), 113-171.

[18] Pätzold, M., Neubauer, F. M., Carone, L., Hagermann, A., Stanzel, C., Häusler, B., ... & Dehant, V. (2004, August). MaRS: Mars express orbiter radio science. In Mars Express: The Scientific Payload (Vol. 1240, pp. 141-163).

[19] Pätzold, M., Häusler, B., Tyler, G. L., Andert, T., Asmar, S. W., Bird, M. K., ... & Remus, S. (2016). Mars express 10 years at Mars: Observations by the Mars express Radio Science experiment (MaRS). Planetary and Space Science, 127, 44-90.

[20] Withers, P., Felici, M., Mendillo, M., Moore, L., Narvaez, C., Vogt, M. F., ... & Jakosky, B. M. (2020). The MAVEN radio occultation science experiment (ROSE). Space Science Reviews, 216(4), 1-49.

[21] Sánchez-Cano, B., Witasse, O., Herraiz, M., Radicella, S. M., Bauer, J., Blelly, P. L., & Rodríguez-Caderot, G. (2012). Retrieval of ionospheric profiles from the Mars Express MARSIS experiment data and comparison with radio occultation data. Geoscientific Instrumentation, Methods and Data Systems, 1(1), 77-84.

[22] Mahaffy, P. R., Benna, M., Elrod, M., Yelle, R. V., Bougher, S. W., Stone, S. W., & Jakosky, B. M. (2015). Structure and composition of the neutral upper atmosphere of Mars from the MAVEN NGIMS investigation. Geophysical research letters, 42(21), 8951-8957.

[23] De Becker, M., Radio Astrophysics (2022), Course at the University of Liège.

[24] Campbell, B. A., Putzig, N. E., Foss, F. J., & Phillips, R. J. (2013). SHARAD signal attenuation and delay offsets due to the Martian ionosphere. IEEE Geoscience and Remote Sensing Letters, 11(3), 632-635.

[25] Witasse, O., Nouvel, J. F., Lebreton, J. P., & Kofman, W. (2001). HF radio wave attenuation due to a meteoric layer in the atmosphere of Mars. Geophysical research letters, 28(15), 3039-3042.

[26] Bocanegra-Bahamón, T. M., Calvés, G. M., Gurvits, L. I., Cimò, G., Dirkx, D., Duev, D. A., ... & McCallum, J. N. (2019). Venus Express radio occultation observed by PRIDE. Astronomy & Astrophysics, 624, A59.

[27] Hinson, D. P., Tyler, G. L., Hollingsworth, J. L., & Wilson, R. J. (2001). Radio occultation measurements of forced atmospheric waves on Mars. Journal of Geophysical Research: Planets, 106(E1), 1463-1480.
[28] Pätzold, M., Andert, T. P., Asmar, S. W., Anderson, J. D., Barriot, J. P., Bird, M. K., ... & Weiss, B. P. (2011). Asteroid 21 Lutetia: Low mass, high density. Science, 334(6055), 491-492.
[29] Hinson, D. P., Notes on the Doppler shifts experienced by the two-way radio signals in radio occultation experiment, Personal Exchange
[30] Fjeldbo, G., Kliore, A. J., & Eshleman, V. R. (1971). The neutral atmosphere of Venus as studied with the Mariner V radio occultation experiments. The Astronomical Journal, 76, 123.
[31] Fjeldbo, G., Eshleman, V. R., Garriott, O. K., & Smith III, F. L. (1965). The two-frequency bistatic radar-occultation method for the study of planetary ionospheres. Journal of Geophysical Research, 70(15), 3701-3710.
[32] Hinson, D. P., Notes on numerical integration of the Abel transform. SETI Institute, Personal Exchange.
[33] Fjeldbo, G., & Eshleman, V. R. (1968). The atmosphere of Mars analyzed by integral inversion of the Mariner IV occultation data. Planetary and Space Science, 16(8), 1035-1059.
[34] Hinson, D. P., Simpson, R. A., Twicken, J. D., Tyler, G. L., & Flasar, F. M. (1999). Initial results from radio occultation measurements with Mars Global Surveyor. Journal of Geophysical Research: Planets, 104(E11), 26997-27012.
[35] Withers, P. (2010). Prediction of uncertainties in atmospheric properties measured by radio occultation experiments. Advances in Space Research, 46(1), 58-73.
[36] Wang, J., Yue, X., Wei, Y., & Wan, W. (2018). Optimization of the Mars ionospheric radio occultation retrieval. Earth and Planetary Physics, 2(4), 292-302.
[37] Morgan, D. D., Dieval, C., Gurnett, D. A., Duru, F., Dubinin, E. M., Fraenz, M., ... & Plaut, J. J. (2014). Effects of a strong ICME on the Martian ionosphere as detected by Mars Express and Mars Odyssey. Journal of Geophysical Research: Space Physics, 119(7), 5891-5908.
[38] Helioweather website. Website archiving the space weather forecast. http://helioweather.net/
[39] Jakosky, B. M., Grebowsky, J. M., Luhmann, J. G., Connerney, J., Eparvier, F., Ergun, R., ... & Yelle, R. (2015). MAVEN observations of the response of Mars to an interplanetary coronal mass ejection. Science, 350(6261), aad0210.
[40] Ulusen, D., D. A. Brain, J. G. Luhmann, and D. L. L. Mitchell (2012), Investigation of Mars' ionospheric response to solar energetic particle events, J. Geophys. Res., 117, A12306, doi:10.1029/2012JA017671
[41] Australian Space Academy Website. Australian Space Academy website regrouping educational information. https://spaceacademy.net.au/
[42] Mendillo, M., Lollo, A., Withers, P., Matta, M., Pätzold, M., & Tellmann, S. (2011). Modeling Mars' ionosphere with constraints from same-day observations by Mars Global Surveyor and Mars Express. Journal of Geophysical Research: Space Physics, 116(A11).
[43] Mars Climate Database v5.3 : The Web Interface. Mars Global Climate Model LMD developed at the Laboratoire de Météorologie Dynamique/Institut Pierre Simon Laplace (LMD/IPSL). http://www-mars.lmd.jussieu.fr/
[44] Senel, C. B., Temel, O., Lee, C., Newman, C. E., Mischna, M. A., Muñoz-Esparza, D., ... & Karatekin, Ö. (2021). Interannual, Seasonal and Regional Variations in the Martian Convective Boundary Layer Derived From GCM Simulations With a Semi-Interactive Dust Transport Model. Journal of Geophysical Research: Planets, 126(10), e2021JE006965.
[45] Richardson, M. I., Toigo, A. D., & Newman, C. E. (2007). PlanetWRF: A general purpose, local to global numerical model for planetary atmospheric and climate dynamics. Journal of Geophysical Research: Planets, 112(E9).